Ultra-thin MFI zeolite films: Synthesis, Characterization and Progress Toward Industrial Applications

A DISSERTATION
SUBMITTED TO THE FACULTY OF
UNIVERSITY OF MINNESOTA
BY

Neel D. Rangnekar

IN PARTIAL FULFILLMENT OF THE REQUIREMENTS
FOR THE DEGREE OF
DOCTOR OF PHILOSOPHY

Prof. Michael Tsapatsis, Advisor

May 2017

Acknowledgements

I would like to thank my advisor, Professor Michael Tsapatsis, for guiding me through my doctoral studies. It was challenging at times but I would always get inspiration from the many stimulating discussions we had. I believe that working with Professor Tsapatsis has taught me how to be an independent researcher and to ask the right questions at the right time. My sincere gratitude also goes to him for providing me with many opportunities to advance my career.

I would first like to thank ExxonMobil for funding a part of my doctoral research. Many thanks to Dr. Benjamin McCool, Joseph Skowronski, Dr. Meha Rungta and Kevin Leung from ExxonMobil for their productive collaboration. It has also been a great privilege to work with other members of the Tsapatsis research group. I would especially like to thank: Meera Shete, for collaborating with me on several research projects; Han Zhang, for guidance with experiments and for thought-provoking conversations; Dr. Jared Stoeger, for being my first mentor in the lab and for helping me get started with experiments; Dr. Donghun Kim, for collaborating on the membrane project and for providing me with samples; Dr. Raffaele Tiriolo, for collaborating on the low-dielectric constant films project; Dr. Garrett Swindlehurst, Dr. Berna Topuz, Dr. Kumar Varoon Agrawal, Dr. Bahman Elyassi, Dr. Balu and Dr. Limin Ren for their constant guidance and help.

I would also like to thank my family in India and here. My parents, Dr. Amita and Dr. Dilip Rangnekar have made me into the person I am today and I am forever indebted to them; my brother Rohit Rangnekar and sister-in-law Sonal Gaurishankar for their continuing support; Pravin, Vandana, Esha and Shruti Rangnekar for being my second family in Minnesota – I am deeply indebted to them for making me feel at home for over five years; Sadie Ward and her family for being very supportive.

Finally, I would like to thank all my friends, without whom this would not have been possible. A special thanks to Joseph DeWilde (now my brother-in-law), Nandita Mirajkar, Harshada Karnik, Vivek Mishra, Rahul Sangodkar, Sanket Sabnis, Matt Irwin, Alex Mannion, Sid Chanpuriya, Pooja Jambunathan, Rachit Khare, Larry Stern, Jeff Peterson and Sonja Riemenschneider for their continued friendship.

Dedication

To my parents, Dr. Amita and Dr. Dilip Rangnekar.

Abstract

Separation processes account for 10-15% of US energy consumption. A large fraction of that energy is consumed by energy-inefficient thermal separation processes like distillation. If membranes could perform these separations, up to 90% of that energy could be saved. Zeolites have ideal properties for separations, which include their high thermal and chemical stability. However, there are currently very few examples of industrial zeolite membrane separation processes. This is due to the high cost associated with their manufacture, industrially unattractive throughput and lack of membrane separation experiments at industrially relevant conditions. This dissertation aims to make progress on some of these fronts. The recent advances in zeolite membranes are reviewed, with an emphasis on industrial applications. A membrane fabrication procedure using 3.2 nm-thick MFI zeolite "nanosheets" is reported, resulting in high-flux and high separation efficiency membranes. High performance membrane separations at industrially relevant conditions have also been achieved for the first time. Moreover, further progress towards synthesis of even thinner films and membranes has been made. The discovery of a novel deposition technique enables the transfer of monolayers of nanosheets to silicon wafers. By intergrowing them, the thinnest-ever MFI films have been synthesized. In future, this technique could be extended to fabricate even higher-flux membranes. An application of zeolite films on silicon wafers as a low-dielectric constant material is also described. Superior insulating properties and mechanical strength compared to previously reported MFI films is achieved. Such a film could save energy and promote the development of the next generation of computer chips.

Table of Contents

List of Tables

List of Figures

Chapter 1

Introduction

Zeolites are porous, crystalline aluminosilicates which are used in a wide variety of industrial applications.[1,2] So far, 232 zeolite frameworks have been discovered, each denoted by a different 3-letter code, and each with a unique structure and pore geometry.[3,4] The common structural feature among them is a regular arrangement of tetrahedral silicon or aluminum atoms, each bonded to four oxygen atoms. Based on the arrangement, zeolite pore sizes can vary from 0.3 to 2 nm, which creates a vast network of channels and cages.

The charge on a zeolite framework can be varied through the Si/Al ratio. The lower the ratio, the more negatively charged the framework, and greater the number of acid sites. Thus, a major industrial application of zeolites is in catalysis.[5–9] In addition, the negative charge on the framework must be balanced by a positively charged counter-ion, usually sodium or potassium. This endows charged zeolites with ion-exchange properties, with an important application being water purification.[10,11]

Neutral zeolites (Si/Al ~ ∞), also known as pure-silica zeolites, tend to be hydrophobic. A number of applications have been proposed for them, including membrane separations.[12–15] Another application that has been proposed is low-k dielectric materials in electronic circuits.[16,17] Such materials could help prevent leakage current in computer chips as the feature sizes reduce and would significantly aid in the effort to achieve higher computing power.

Of all the frameworks, the zeolite MFI is one of the most widely studied in the literature. It consists of straight channels with a pore opening of 0.54 nm x 0.56 nm along the crystallographic *b*-axis and sinusoidal channels with a pore opening of 0.51 nm x 0.55 nm along the crystallographic *a*-axis.[18,19] The structure of MFI is shown in **Figure 1-1**.

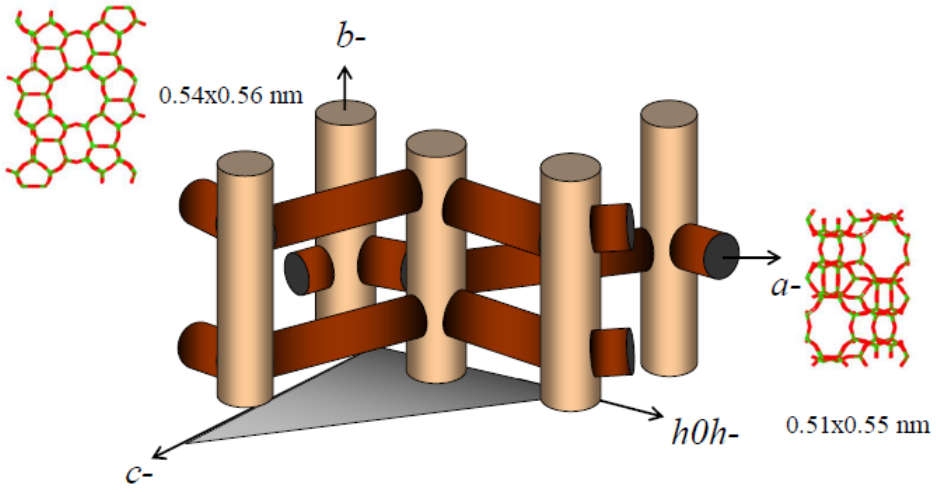

Figure 1-1: 3-dimensional schematic of the MFI framework topology. Straight channels are shown along the b-axis while sinusoidal channels are shown along the a-axis. The corresponding 2-dimensional projections along the a- and b-axes are also shown. Adapted from ref.[20]

Zeolites like MFI have long been reported for their application in membrane separations. Such separation processes are essential today when industrial separation accounts for 10-15% of US energy consumption, with energy intensive thermal separation processes like distillation consuming almost 80% of this energy.[21] Membranes have been shown to consume 90% less energy than distillation. Thus, if some of these distillation-based separation processes can be replaced with membranes, it would result in significant energy savings. This is especially important with the current threat from climate change and concerns about energy security.[22,23]

An important industrial separation in which MFI zeolite membranes have extensively been studied is the separation of xylene isomers.[15,24] Xylene isomers are aromatic molecules typically obtained from the naphtha cut of a crude oil distillation column. The most widely used of these isomers is para-xylene (*p*-xylene), with a global market of $33 billion in 2015 and a CAGR of 7%.[25] The majority of p-xylene is used as a raw material in the manufacture of polyethylene terephthalate (PET), a commodity polymer used for the production of packaging material, insulation, plastic bottles etc. Currently, separation of xylene isomers is carried out either through adsorption or fractional crystallization.[26,27]

Another application of MFI membranes is in separation of *n*-butane from *iso*-butane. *n*-butane is a widely used fuel gas, used in domestic heating and transportation while *iso*-butane is a common refrigerant and is also used in manufacture of high density polyethylene.[28–30] The demand for butanes is driven by developing countries like India and China, where *n*-butane in the form of LPG (liquefied petroleum gas) is widely used

due to lower pollution associated with its combustion.[28] The global butane market is expected to increase to about $203 billion by 2020 at a CAGR of about 4%, with LPG accounting for 66% of the market.[31] Currently, separation of butane isomers is done through an energy intensive distillation process. High capital and operating costs are required because of the close-boiling nature of butane isomers.[32]

Despite these applications having been widely studied, an industrial application of MFI membranes has not been realized. There are three main reasons for this:

1. MFI membranes are usually made as a film on top of a porous support.[33,34] The most stable support materials compatible with the MFI hydrothermal growth conditions have been ceramics like alumina. Due to the brittle nature of ceramics and their high manufacturing cost, typical ceramic-supported zeolite membranes cost >$5000/$m^2$,[35] which is more than 20 times higher than polymeric membranes like polydimethylsiloxane (PDMS).[36] Though polymer-supported zeolite membranes have been reported,[37–39] inherent incompatiblity at the zeolite-polymer interface still remains an issue.
2. Given the high cost, if the flux of permeating molecules can be increased, this would make zeolite membranes industrially attractive. One strategy is to decrease the thickness of the selective zeolite layer. However, it has been estimated that the zeolite thickness needs to be ~50 nm for feasibility of application in industrial membrane processes.[35] This is a challenging task, given that defects are bound to increase with a decrease in film thickness. This is also impossible to achieve with conventional micron-sized zeolite seeds.

3. Very little data exists on the actual operation of zeolite membranes at industrial conditions. Especially for xylene separations, high separation performance for MFI membranes has been demonstrated at low temperature (<200ºC) and low pressure of xylene (~500 Pa partial pressure).[40,41] However, for industrial applications, separation performance at high partial pressures of xylene (50 kPa or higher) is necessary. Such data is currently very limited.[24]

This dissertation aims to focus on points 2 and 3, while point 1 is currently being addressed by co-workers.[39] With regard to progress towards ultra-thin MFI films, there have been significant developments in this area in the past few years. There have been several attempts to reduce the size of the seed particles in order to reduce the final film thickness. By modifying the synthesis conditions, nano-sized seed crystals have been developed.[42] A substantial breakthrough came about in 2009 when Ryoo and co-workers developed stacked multilamellar sheets of MFI by using a modified structure directing agent (SDA).[6] Following this, the Tsapatsis group exfoliated this material to obtain MFI nanosheets which are just 1.5 unit cells (~3.2 nm) in thickness (see **Figure 1-2**).[43] By using nanosheets, the thickness of the selective layer was reduced to sub-100 nm, and has consequently resulted in *p*-xylene permeance >$3x10^{-7}$ molm-$^{2}s^{-1}Pa^{-1}$, a large improvement over previous reports.[41,44]

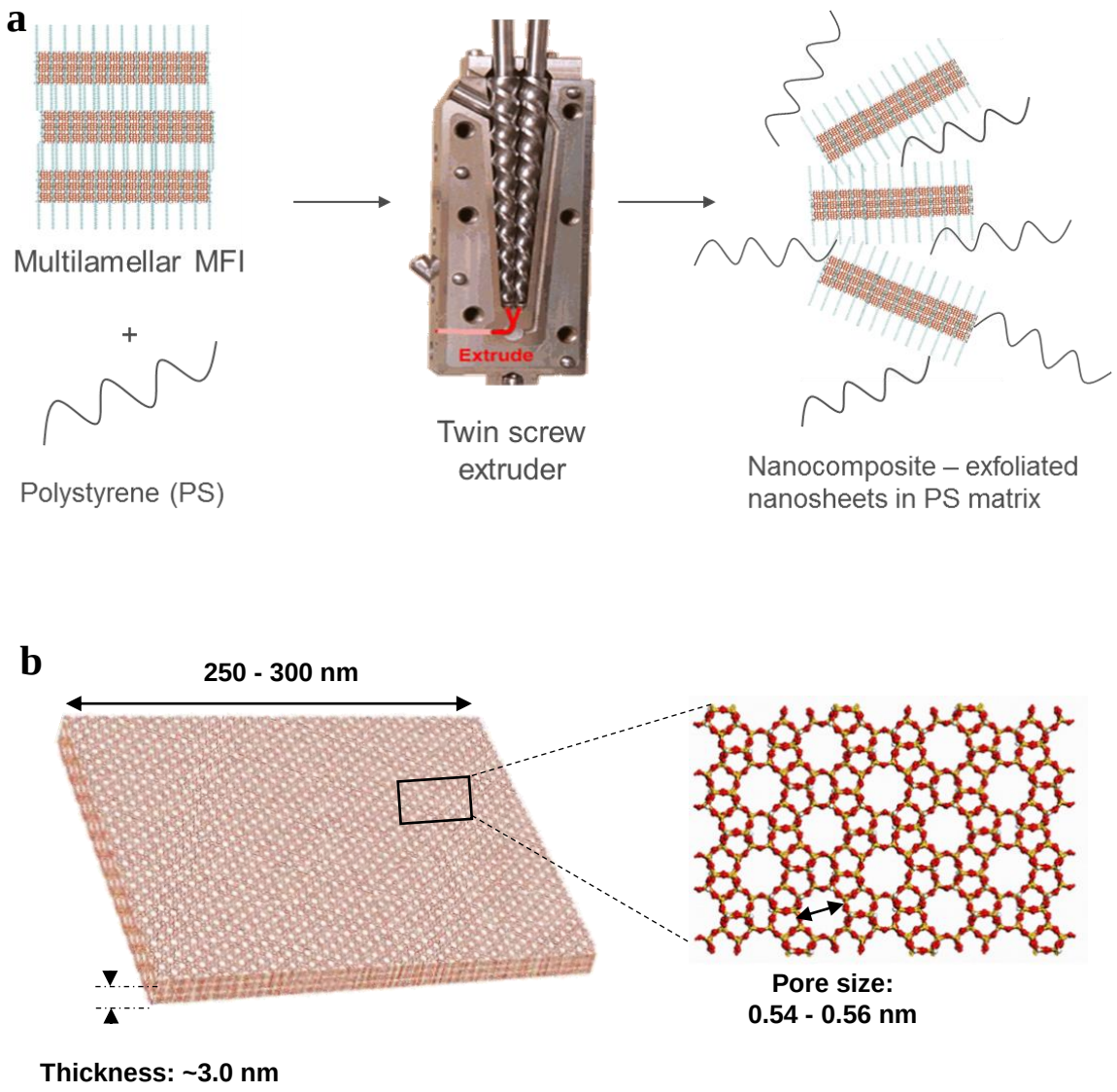

Figure 1-2. a. Schematic of exfoliation of multi-lamellar MFI by polymer melt compounding and b. schematic of an exfoliated MFI nanosheet, showing thickness, lateral size and crystal structure down the b-axis.

The secondary growth method, in which the support surface is first seeded and then seeds are further induced to grow, is currently the most preferred method for synthesis of thin

films of MFI with a specfic orientation. Several advances in secondary growth have been made recently. It has been reported previously that modification of the structure of the SDA can result in MFI crystals of different morphologies.[33,45] Other researchers have replaced the TPA^+ with other SDAs like tetraethylammonium hydroxide (TEA^+), to promote faster in-plane growth compared to out-of-plane growth.[46,47] Yoon and co-workers have recently developed a "gel-free" secondary growth technique where the silica source for growth comes from the substrate.[40,48] This prevents wastage of chemicals which typically happens in sol- or gel-based secondary growth. Recently, the Tsapatsis group has utilized this technique to synthesize ultra-thin MFI films on porous and non-porous supports.[41,49]

Further progress towards achieving the goals of an industrial application of zeolite thin films and membranes is demonstrated in this dissertation. It is organized as follows:

In Chapter 2 a new procedure for deposition of single-layer coatings of MFI nanosheets is reported.[49] First, MFI nanosheets were chemically treated with acids to partially remove some of the SDA which makes them hydrophobic. These partially hydrophilic nanosheets were then dispersed on the surface of water in a Langmuir trough, and could be transferred layer-by-layer to non-porous substrates like silicon wafers. After secondary growth, the thinnest-ever MFI films were obtained. It could be possible in future to extend this procedure, known as the Langmuir-Schaefer (LS) method, to form ultra-thin zeolite membranes by deposition on porous supports.[50] It has also been demonstrated that the LS method can be made into a continuous process for fabricating large-area films.[51,52]

In Chapter 3, an application of MFI thin films on non-porous supports is demonstrated.[53] As mentioned earlier, pure-silica zeolites are good candidates for low-k materials in electronic circuits. Previous reports have used spin-coated zeolite films on silicon wafers for low-k application. The resulting porous films have low dielectric constant but also low mechanical strength. We have shown here that sub-micrometer thin films of MFI can be synthesized on gold-coated substrates with dielectric constant and elastic modulus close to the values predicted for single-crystal MFI.[54]

In Chapter 4, the recent literature in zeolite membranes is reviewed. There is emphasis on developments in seeding techniques, including manual assembly and Langmuir trough coating. Recent advances in sub-1 μm membranes and polymer-supported membranes are discussed. There is also a discussion on developments in permeation modeling of zeolite membranes. Finally, the current industrial applications of zeolite membranes are presented.

In Chapter 5, the recent developments in ultra-thin MFI membranes from nanosheet seeds are reported. The focus is on the progress towards application of these membranes in industrial xylene separation. This involves fabrication of stronger supports and better sealing techniques to enable permeation testing at high temperature and high pressure conditions. High temperature, high pressure xylene separation results are reported. A high separation factor and flux at these conditions is achieved for the first time. Results on xylene separation by another type of high performance MFI membrane (made from bottom-up dC5 nanosheet seeds) is also reported.[55]

Chapter 2

Monolayer Deposition and Secondary Growth of 2-Dimensional MFI Zeolite Nanosheets[‡]

[‡]Portions of this chapter appear in the following:

N. Rangnekar*, M. Shete*, K. V. Agrawal, B. Topuz, P. Kumar, Q. Guo, I. Ismail, A. Alyoubi, S. Basahel, K. Narasimharao, C. W. Macosko, K. A. Mkhoyan, S. Al-Thabaiti, B. Stottrup, M. Tsapatsis, *Angew. Chemie Int. Ed.* **2015**, *54*, 6571-6575.

*Equally contributing authors

2.1. Chapter overview

In this chapter, a novel coating procedure for monolayer transfer of nanosheets is described. First, stable suspensions of zeolite nanosheets (3 nm thick MFI layers) were prepared in ethanol following acid treatment, which partially removed the associated organic structure-directing agent. Further characterization revealed that their crystal structure was preserved. Nanosheets from these suspensions were dispersed at the air-water interface and transferred to silicon wafers using Langmuir Schaefer deposition. Using layer-by-layer deposition, control on coating thickness was demonstrated. In-plane X-ray diffraction (XRD) revealed that the deposited nanosheets contract upon calcination similar to bulk MFI crystals. The monolayer coatings were then induced to intergrow through different secondary growth techniques. Gel-free resulted in sub-12 nm thick MFI films – the thinnest ever reported. Finally, it was demonstrated that on calcination, there

was no contraction detectable by in-plane XRD, indicating well-intergrown MFI films that are strongly attached to the substrate.

2.2. Introduction

2D zeolites, nanosheets with thickness comparable to the unit-cell-dimensions of the corresponding structure type (see http://www.iza-online.org),[56] open exciting opportunities for traditional uses in catalysis and separations[5,57–63] and hold promise for emerging applications of zeolite films as membranes,[35] low dielectric constant materials,[16,64] anti-corrosion coatings, etc.[16] Fabrication of thin films of 2D zeolites relies on: (i) the availability of suspensions that exhibit colloidal stability, and are free of amorphous and non-exfoliated contaminants; and (ii) development of deposition techniques by which the suspended zeolite nanosheets can be quantitatively transferred on various supports to form oriented thin coatings.

Following the discovery of multi-lamellar MFI zeolite by Ryoo and co-workers,[57] we used a polymer-melt-compounding technique (for exfoliation) combined with density gradient centrifugation (for purification) to prepare suspensions of exfoliated 2D MFI nanosheets in toluene and octanol.[43][44] In previous reports, the octanol and toluene suspensions were used to form nanosheet deposits on porous supports by filtration.[43][44] Deposition by filtration ensured transfer of all zeolite nanosheets from the suspension to the surface of the support. Such quantitative transfer from suspension to support, without nanosheet loss, is essential because high quality 2D zeolites cannot be obtained currently in large quantities. However, the filtration approach is only applicable to porous supports.

Furthermore, a uniform coating with thickness on the order of a single-layer of nanosheets is not possible by this technique. To overcome these drawbacks, the Langmuir-Schaefer (LS) deposition technique, for the formation of MFI nanosheet coatings, is described in this chapter.

Deposition from Langmuir trough is a well-known method used to obtain monolayers of surfactant molecules[65–67] and it has been used to deposit particles including zeolites[50,68–71] and various 2D non-zeolitic materials.[72,73] To employ the LS deposition, a nanosheet suspension in octanol was prepared according to a previously reported procedure.[44] The nanosheets were then transferred to ethanol and subjected to an acid treatment procedure, reported earlier by Corma and co-workers for the removal of organic structure-directing agent (SDA) from zeolites.[74] This acid treatment resulted in partial removal of the long-chain SDA used in the synthesis of multi-lamellar MFI and allowed for the formation of stable suspensions in ethanol. Nanosheets could then be introduced at the air-water interface, and transferred to silicon wafers by using the Langmuir-Schaefer horizontal lifting technique.[66] Secondary growth of these monolayers resulted in intergrown, preferentially oriented, sub-12 nm films, which were firmly attached to the support and did not show in-plane contraction upon calcination. On the other hand, non-intergrown multi-layers, could slide and contract upon calcination. LS provides the opportunity to coat monolayers of 2D zeolites such as MFI and MWW nanosheets. Secondary growth can allow formation of sub-12 nm, crack-free, intergrown zeolite films, of which to the best of our knowledge, there are no previous reports.

2.3. Experimental

2.3.1. Acid treatment of MFI nanosheets

MFI nanosheet suspensions in octanol were prepared according to the previously reported procedure.[44] The octanol suspension was then centrifuged (Beckman Coulter, Model: Avanti J-20 XP equipped with JA25.50 rotor) at 40000 g for 3 hours and the supernatant was discarded. The resulting cake was dispersed in approximately 50 mL filtered ethanol (200 proof, Decon Labs). The dispersion was centrifuged at 40000 g for 3 hours and the supernatant was discarded. This ethanol washing step was repeated two more times. The final cake was dispersed in 20 mL of filtered ethanol by vortexing (Fisher Scientific vortex mixer). For the first step of acid treatment, 0.098 g of H_2SO_4 (98%, EMD Chemicals) was taken in a 50 mL glass reaction vial. The nanosheet dispersion in ethanol was then added to it. The vial was sealed and placed in an oil bath set to 80^0C for 16 hours under stirring.

Following this, the vial was cooled and uncapped. The contents were centrifuged at 40000 g for 3 hours and the supernatant was discarded. This was followed by an ethanol washing step, as before. Further, 7.89 g (10 mL) of filtered ethanol was added to the cake and dispersed by vortexing. 1.5 g of HCl solution in water (1 M, Sigma-Aldrich) was taken in a 50 mL glass vial followed by the addition of the nanosheet suspension. 10 mL of filtered heptane (anhydrous 99%, Sigma-Aldrich) was then added to the vial. The vial was capped and placed in an oil bath at 90^0C for 16 hours under stirring.

On completion of this step, the vial was cooled and the contents were centrifuged at 40000 g for 3 hours. The supernatant was discarded and 40 mL ethanol was added to the

cake followed by vortexing. A drop of the resulting suspension was deposited on a holey carbon grid for analysis by TEM.

2.3.2 Langmuir-Schaefer deposition (LS)

Commercially available 4-inch Si wafers (Silicon Quest International, Inc.) in <100> orientation were used as substrates . They were either used as-purchased or after subjecting them to thermal oxidation. For the latter, the Si wafers were heated at 900-1000°C in oxygen atmosphere in a Tylan tubular furnace in order to grow 50 nm oxide. The wafers were then cut into 1 cm x 1 cm squares using a wafer saw (Disco DAD 2H/6T) equipped with a diamond blade (Disco NBC-ZH2030-SE). The substrates were sonicated in DI water (generated by EMD Millipore Elix 5 water purifier) in a bath sonicator (Branson 5510R-DTH, 135 Watts) for about 5 min, dried at ambient temperature and used for LS experiments.

In a typical LS experiment, 1.5 mL of nanosheet suspension in ethanol was carefully deposited on the air-water interface in a Langmuir barrier trough (Nima Liquid-Liquid trough with IU4 interface and Nima LB dipping mechanism, maximum area 120 cm^2, minimum area 23 cm^2) using a micropipette. After the deposition was completed, the trough was left without disturbance for 30 min to allow the ethanol to evaporate. Following this, the trough was set to attain a specific surface pressure and the trough barriers were compressed such that the trough area reduced at a speed of 30 cm^2/min. Once the desired pressure was attained, a previously prepared Si substrate, mounted horizontally on the dipper (NIMA), was lowered at a speed of 1 cm/min until it just

touched the air-water interface. Once contact was made, the Si substrate was lifted upwards at the same speed. The substrate was detached from the dipper and left to dry. Following the coating process, the surface pressure dropped by 5-10 mN/m. The barriers were further compressed to compensate for this. The coating process was then repeated using another substrate. Multilayer coatings were obtained by repeating the coating procedure on the same substrate for the desired number of cycles.

In order to collect surface pressure - area isotherms, the barriers were compressed and expanded between the limits of maximum and minimum area for multiple cycles, without taking coatings.

2.3.3. Secondary growth

Prior to secondary growth, the nanosheet-coated substrates were first calcined at 500°C for 6 hours in 150 mL/min air flow to remove the SDA.

a. TPA-silica sol-based growth

Clear sol secondary growth was performed according to a previously reported procedure.[75] The growth solution was prepared by sequentially adding tetrapropylammonium hydroxide (TPAOH, 1M Sigma Aldrich), tetraethylorthosilicate (TEOS, 98% reagent grade Sigma Aldrich) to distilled water in a molar composition of 5TEOS:1TPAOH:1000H_2O. The solution was hydrolyzed at room temperature for 15 hours under stirring. After hydrolysis, it was filled in a HF-cleaned Teflon liner, sealed in a stainless-steel autoclave and placed in an oven set to 150°C for 2 hours. This pretreated solution was filtered using a 0.2 μm GHP Acrodisc syringe filter (Pall Corporation) into a

HF-cleaned Teflon lined autoclave. Calcined nanosheet coating deposited on as-purchased silicon wafer was placed vertically in the solution using a Teflon holder and secondary growth was carried out at 90°C for 5 hours. The autoclave was then cooled and the substrate was removed, washed for 2-3 min with DI water, dried at ambient conditions in air and characterized.

b. TEAOH gel growth

Gel growth was carried out according to a previously reported procedure.[76] The gel composition used was 4TEOS:1.92TEAOH:0.36$(NH_4)_2SiF_6$:40H_2O (molar ratios). The gel was prepared by mixing 2/3 of the total amount of TEAOH (35% w/w Alfa Aesar) and DI water, followed by the addition of TEOS (98%, Sigma Aldrich) to the mixture and stirring with a magnetic stirrer for 30 min. In a separate container, the remaining TEAOH, DI water and $(NH_4)_2SiF_6$ (Sigma Aldrich) were mixed until complete dissolution of $(NH_4)_2SiF_6$, about 30 min. The contents of the second container were quickly added to the first under vigorous stirring. After the mixture solidified, it was left for 6 hours under static conditions for aging. 100 g of the mixture was then blended in a 500 mL glass beaker with a handheld food blender (KitchenAid) for about 10min. Approximately 10 g of the blended mixture was loaded into the bottom of a Teflon liner. Calcined nanosheet coating on as-purchased silicon wafer was inserted vertically into the gel. The liner was sealed in a stainless-steel autoclave and placed in an oven at 150°C for 6 hours. The autoclave was then removed from the oven and cooled. The substrate was removed from the liner and thoroughly washed with DI water to remove any adhering

gel. Following this, the substrate was soaked in 0.2 M aqueous solution of NH_4F (Sigma-Aldrich) for 6 hours to remove amorphous silica from the surface. It was then removed, washed with DI water, dried at ambient conditions in air and characterized.

c. Gel-less growth

Gel-less growth was done according to a previously reported procedure.[40] The calcined nanosheet coating on silicon wafer with 50 nm thermally-grown oxide was spin-coated with 0.005 M TPAOH aqueous solution (prepared from 1 M TPAOH solution, Sigma Aldrich) and then placed horizontally on a Teflon holder in a Teflon-lined stainless steel autoclave. 0.2 g of 0.005 M TPAOH was added to the bottom of the liner. The autoclave was sealed and placed in a convection oven set to 220°C for 72 hours under static conditions. At the end of this period, the autoclave was removed from the oven and cooled. The substrate was then removed from the liner and characterized.

2.3.4. Characterization

TEM samples were prepared by drop-casting suspensions of nanosheets in octanol and acid-treated nanosheets in ethanol on TEM grids (ultrathin carbon film on holey carbon support film, 400 mesh Cu, Ted Pella). The grid was dried at room temperature and imaged. Bright-field conventional transmission electron microscopy (BF-CTEM) was performed on a FEI Tecnai G2 F30 (S)TEM with TWIN pole piece, a Schottky field-emission electron gun operating at 300 kV and equipped with a Gatan 4k × 4k Ultrascan CCD. High angle annular dark field, scanning transmission electron microscopy

(HAADF-STEM) was performed at 300 kV with an incident semi-convergent angle of 19 mrad and detector collection angles of 47.5–200 mrad on an FEI Titan™ G2 60–300 scanning transmission electron microscope (STEM). To resolve the crystal structure of MFI-zeolite nanosheets, we performed BF-CTEM and high angle annular dark-field scanning transmission electron microscopy (HAADF-STEM) imaging. Data was collected using low dose of electrons to avoid beam damage of these nanosheets, thus resulting in low signal to noise ratio (SNR) in the images. In order to improve structural visibility, BF-CTEM images were digitally processed using periodic Bragg filtering to reduce the noise and resolve the structure of MFI nanosheets.

TGA analysis was performed using a PerkinElmer TGA-7 analyzer to estimate the SDA content of nanosheets before acid treatment. This was compared with weight loss from nanosheets before acid treatment.[44] Analysis was carried out by heating a few mg of the nanosheet cake obtained after centrifugation in air flow (100 mL/min) from 130 to 550°C (heating rate of 1°C/min) and holding the sample at 550°C for 8 hours.

Scanning electron microscopy (SEM) images of the nanosheet films were acquired using JEOL 6700 microscope operating at 1.5 kV.

For the preparation of atomic force microscopy (AFM) specimens, nanosheet coating was made by LS at 25 mN/m surface pressure on a thermally oxidized silicon wafer. The sample was calcined in air flow at 500°C for 6 hours to remove the SDA from the pores and surface of the nanosheets. AFM was carried out in tapping mode in the repulsive regime using a Bruker Nanoscope V Multimode 8 AFM. Analysis of AFM images was done using Gwiddion 2.31 software. In order to calibrate the AFM height data, freshly

cleaved muscovite mica was etched in 50% hydrofluoric acid for 4 hours to produce 2.0 nm steps on mica.[77] These steps were used as the calibration standard.

FTIR spectra were recorded in transmission mode on a Thermo Scientific Nicolet iS50 FT-IR spectrometer equipped with a liquid nitrogen cooled MCT detector. The spectrometer was purged with dry air and the spectra were acquired in the range of 4000-650 cm^{-1} and averaged over 16 scans. The data analysis was performed using Omnic software.

X-ray diffraction scans were performed using a Panalytical X'Pert Pro diffractometer in in-plane mode. The incident beam optics consisted of an x-ray lens with cross-slit collimator with beam in point focus. The diffracted beam optics consisted of a parallel plate collimator (PPC). The X-ray wavelength used was mainly Cu Kα1. Cu Kα2 stripping was done using MDI-Jade 2010 software. Scans were done in in-plane mode with 2θ varying from 22.5° to 24.5° with a step size of 0.02° and dwell time of 150 s.

Secondary grown MFI layer deposited on a silicon substrate was coated with a 150 nm gold layer before performing focused ion beam (FIB) milling. This gold coated layer was further coated with platinum (Fig. S6 a) to perform thinning experiments using a dual beam FEI Quanta 200 3D FIB-SEM instrument. Thinning was done using a Ga-As ion beam. The thinned sample was analyzed in an aberration corrected FEI-Titan transmission electron microscope (TEM). High angle annular dark field scanning TEM (HAADF-STEM) imaging was done at <30 pA electron beam current at 17 mrad convergence angle (Fig. S6 b, c). Spatially resolved STEM energy dispersive X-ray

imaging was performed on a 150 nm x 250 nm section. It is not possible to distinguish between SiO_2 and MFI zeolite since the elemental composition of both layers is same.

2.4. Results and Discussion

2.4.1. Acid treatment of nanosheets

Following acid treatment, removal of SDA ($C_{22}H_{45}$-$N^+(CH_3)_2$-C_6H_{12}-$N^+(CH_3)_2$-C_6H_{13}.($2OH^-$)) was quantified by thermogravimetric analysis (TGA) of zeolite nanosheets. Specifically, the nanosheet cake recovered by centrifugation was analyzed by TGA after acid treatment and compared with TGA from nanosheet cake prior to acid treatment (**Figure 2-1**).

Before acid treatment, the zeolite nanosheets contain ~29 wt% SDA, the majority of which is expected to reside inside their straight pore channels.[44] After acid treatment, the amount of SDA reduces to less than ~8 wt%. The partial removal of SDA is also indicated by a color change of the nanosheet cake from yellow to white. We believe that the acid treatment procedure reduces the lipophilicity of nanosheets and allows for their transfer out of octanol to form a stable suspension in ethanol.

Figures 2-2a and 2-2e show transmission electron microscopy (TEM) images of nanosheets, deposited on carbon coated copper TEM grids, before and after acid treatment, respectively. Nanosheets deposited from both octanol and ethanol suspensions appeared well dispersed. In contrast, nanosheets suspended in ethanol without acid treatment formed agglomerates (not shown).

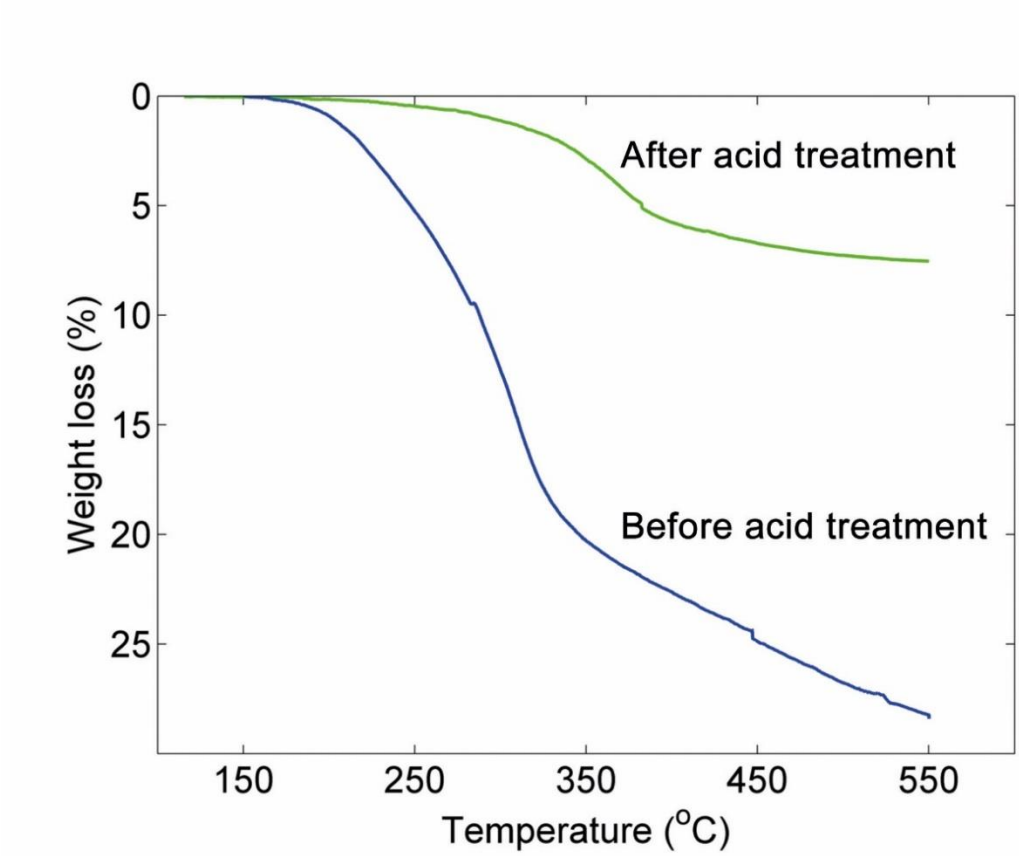

Figure 2-1. TGA analysis of as-synthesized nanosheets without acid treatment (obtained from Ref. 1) and acid-treated nanosheets. Acid-treated nanosheets show a weight loss of about 8% compared with about 29% for as-synthesized nanosheets.

High-resolution TEM images (**Figure 2-2b and 2-2f**) and electron diffraction patterns (**Figure 2-2c and 2-2g**) show that the acid treatment process does not alter their crystal structure. More detailed crystallographic investigations regarding the structural integrity and thickness of the nanosheets were performed by diffraction tilting experiments in the TEM.[78] The experimental and simulation data shown in **Figures 2-2d and 2-2h**, confirmed that the nanosheets were 1.5 unit cells thick (which corresponds to

approximately 3 nm) and further confirm that the crystalline structure of MFI was preserved.

Although a major fraction of the SDA was removed, the remaining SDA appears to be occluded in the micropores as Ar-adsorption measurements failed to detect any microporosity (data not shown). Moreover, the presence of the remaining SDA makes the nanosheets retain some hydrophobicity which prohibits their dispersion in water.

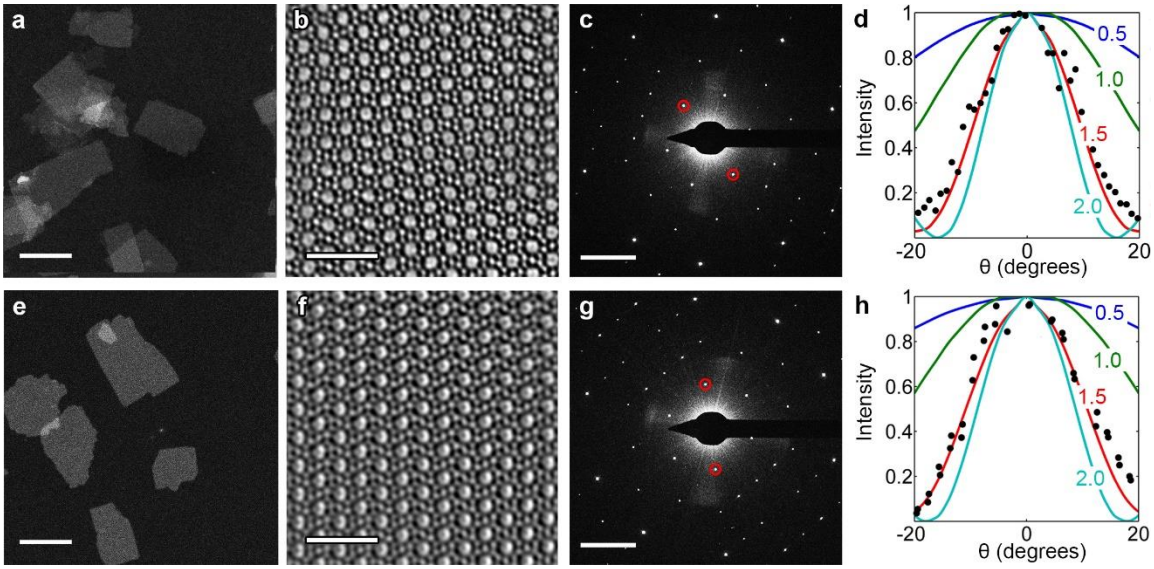

Figure 2-2. Top row: MFI nanosheets before acid treatment (deposited from octanol); Bottom row: MFI nanosheets after acid treatment (deposited from ethanol). (a),(e) Low magnification HAADF-STEM images of MFI nanosheets supported on a ultrathin carbon films showing uniform thickness of nanosheets; scale bars: 500 nm; (b),(f) High resolution Bragg filtered CTEM images of MFI nanosheets; scale bars: 2 nm; (c),(g) [010] zone axis diffraction pattern with the red circles highlighting (101) and (-10-1) spot; scale bars: 1 nm^{-1} (d),(h) Multi-slice simulated modulation of encircled diffraction spots in (c),(g) with tilting for nanosheets of different thickness (solid lines) and corresponding experimental scatter data (solid circles) confirming that the nanosheets are 1.5 unit cells thick.

2.4.2. Langmuir-Schaefer deposition

The dispersed nanosheets in ethanol were transferred to the air-water interface by simply adding droplets of the suspension on the surface of water. Ethanol evaporates or dissolves in water leaving behind the nanosheets which spread on the surface of water.

The surface pressure isotherm obtained during a typical LS experiment is shown in **Figure 2-3a**. At large trough areas, the isotherms remained horizontal until, at a certain area, a rapid increase in surface pressure was observed due to the onset of interactions between adjacent particles. When a certain minimum trough area (i.e., maximum surface pressure) was reached, the barriers were expanded, and a decrease in surface pressure is observed, which did not follow the surface pressure vs. area curve obtained during compression. The slower increase and sharper decline of surface pressure during compression and expansion, respectively, may indicate loss of particles to the water subphase and/or irreversible aggregation of the nanosheets. To avoid this, nanosheet coatings were made on silicon wafers during the first compression.

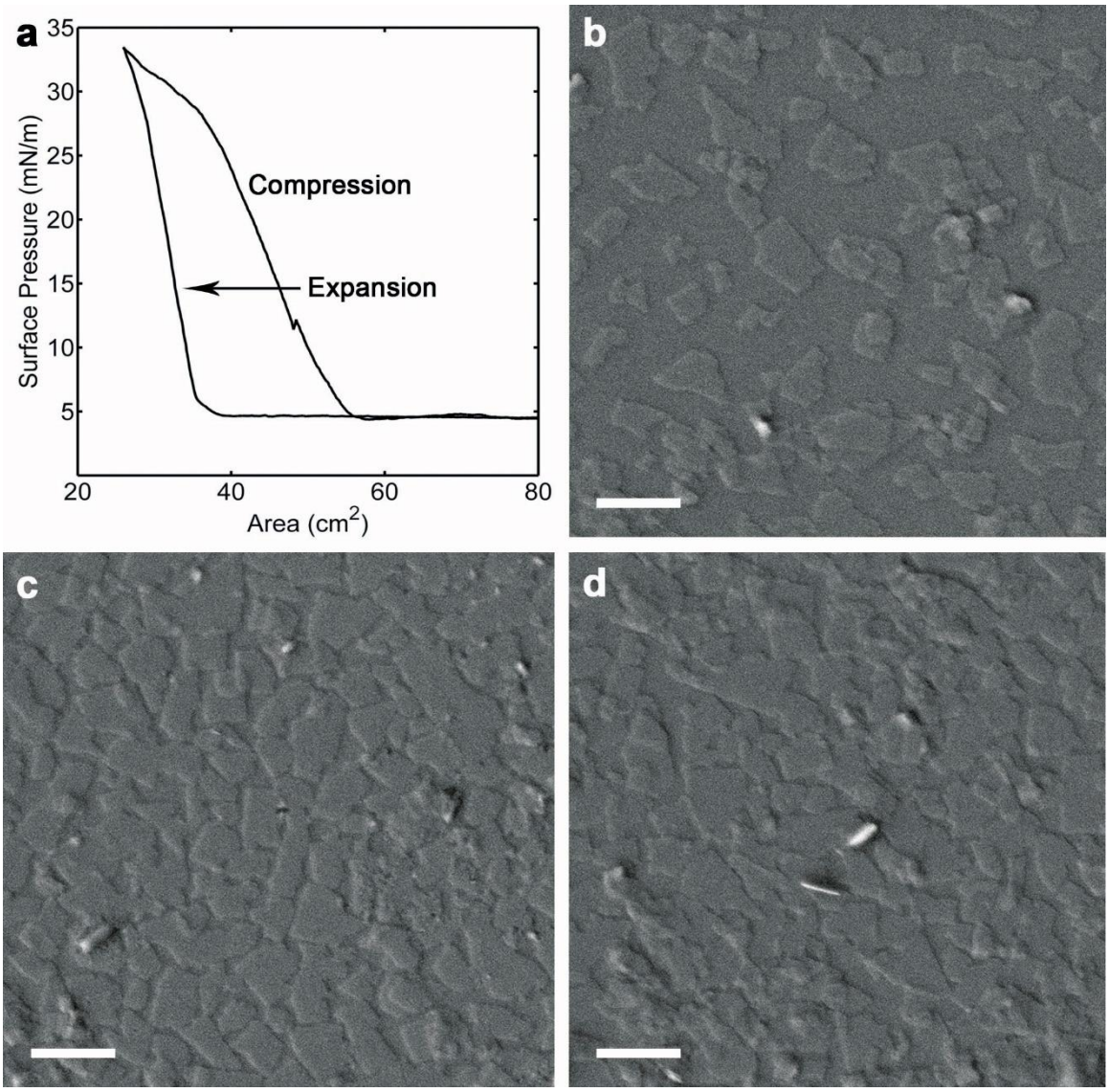

Figure 2-3. (a) Surface pressure isotherm from the first compression-expansion cycle obtained during a typical LS experiment; (b)-(d) Coatings made at 15, 20 and 25 mN/m surface pressure on thermally oxidized silicon substrates showing that packing of nanosheets increases with surface pressure, eventually resulting in overlapped coatings; scale bars: 400 nm.

Silicon wafers, as-purchased or with a ~50 nm thermally-grown oxide layer were used as the substrates for nanosheet coatings. **Figures 2-3b to 2-3d** show scanning electron microscopy (SEM) images of the coatings made on thermally oxidized silicon wafers at various surface pressures. Surface coverage by nanosheets increased with increasing surface pressure. Closely packed monolayers were obtained at 20 and 25 mN/m surface pressure. Low-magnification SEM images in **Figure 2-4a and 2-4b** show that there is uniformity in the coatings over large areas.

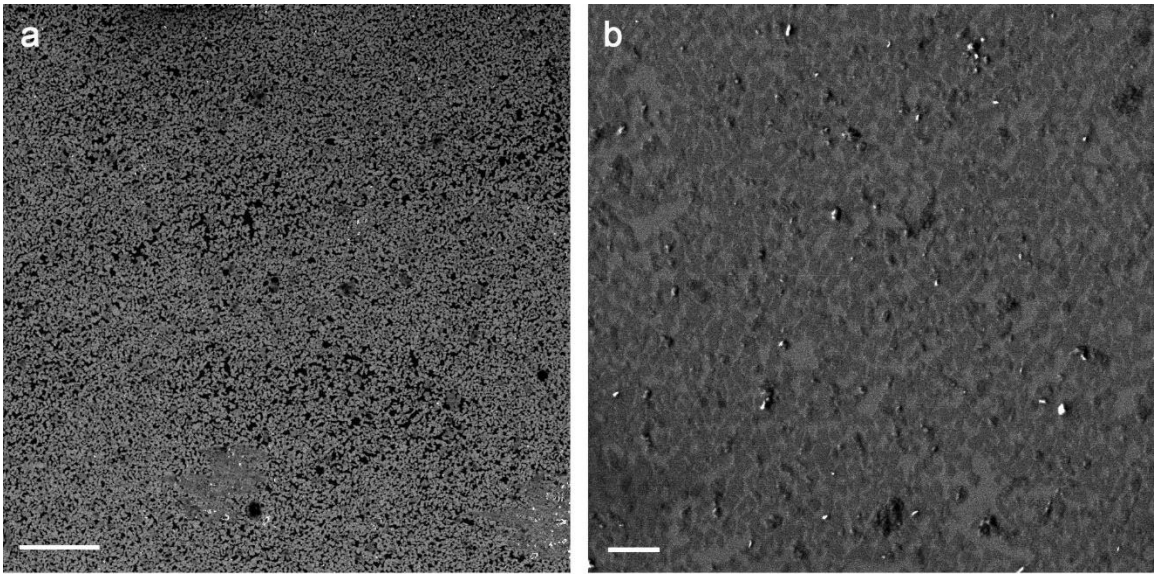

Figure 2-4. (a), (b) Low magnification SEM images of calcined nanosheet coating made by LS showing uniformity over large areas and absence of cracks. Scale bar in (a): 5 µm and (b): 1 µm.

At even higher surface pressures the onset of nanosheet overlapping (**Figure 2-5)** was observed. This is undesirable for fabricating ultra-thin films. For further experiments, we made coatings at the conditions corresponding to the films in **Figure 2-3c and 2-3d**.

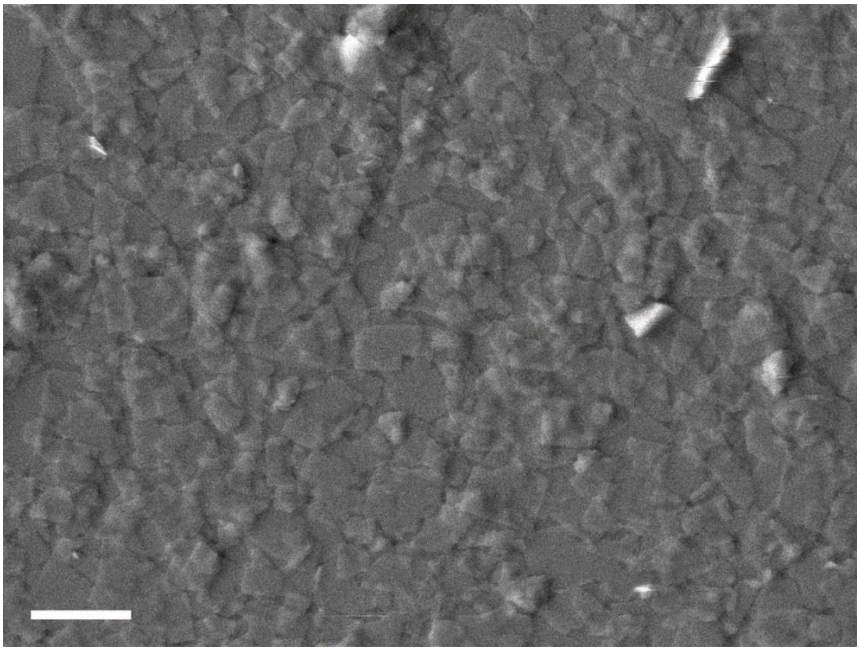

Figure 2-5. SEM image of nanosheet coating on thermally oxidized Si wafer, obtained by LS at 30 mN/m surface pressure. It reveals that considerable overlap of nanosheets occurs at high surface pressure. Bending of some nanosheets is also evident in areas of bright contrast. Scale bar: 400 nm.

The thickness of a monolayer coating of nanosheets was confirmed by atomic force microscopy (AFM), as shown in **Figures 2-6a and 2-6b**. The coating imaged by AFM was deposited at 25 mN/m surface pressure on a thermally oxidized silicon wafer (similar to the coating shown in **Figure 2-3d**). Line profiles across three randomly chosen nanosheets are shown in **Figure 2-6b**. The average thickness is measured to be 2.9 ± 0.09

nm. Almost all the nanosheets seen in **Figure 2-6a** have similar contrast, which indicates uniform thickness of the coating. A few overlapped regions are present (seen as bright spots in **Figure 2-6a**) but mostly there is monolayer coverage of nanosheets on the substrate.

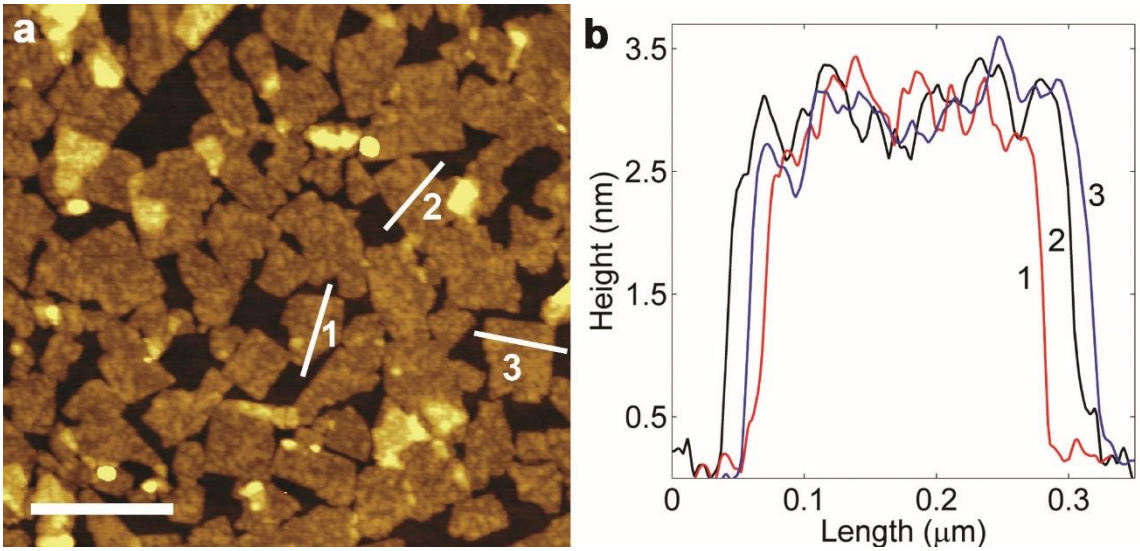

Figure 2-6. (a) AFM image of nanosheets deposited on silicon substrate using LS; scale bar: 500 nm and (b) the corresponding height profiles showing that nanosheets are approximately 3 nm in thickness. Calibration was done using 2.0 nm steps on HF-etched mica.[27]

The surface coverage of nanosheets could be increased by repeating LS several times on the same substrate. As seen in **Figure 2-7c**, some curling was observed after 10 cycles of deposition. However, the films exhibited high coverage on the silicon substrate, compared to the single-layer coating shown in **Figure 2-7a**. Infrared spectroscopy (IR) was used to detect the presence of SDA (**Figures 2-7b and 2-7d**). As expected, peaks

corresponding to the C-H stretching mode of SDA were observed in the region from 2800-3000 cm^{-1} for as-deposited single-layer and multi-layer films, while no IR signal corresponding to the SDA was detected after calcination at 500ºC.

Multi-layer coatings of nanosheets were analyzed by in-plane XRD, as seen in **Figures 2-7e and 2-7f**. Such an analysis could not be done for single-layer coatings due to the low signal-to-noise ratio obtained by the in-house diffractometer used. The deposited nanosheets were not intergrown but remained in contact through weak non-covalent bonding interactions (e.g., van der Waals and hydrogen bonding). It was, therefore, expected that they can slide with respect to each other. Indeed, in-plane XRD revealed significant differences in the crystallographic dimensions of the deposited nanosheets before and after calcination, as shown in **Figure 2-7f**.

Shifts in the (501) and (303) Bragg peaks indicated in-plane contraction of the lattice. The observed in-plane contraction of the nanosheets is comparable to that expected from bulk silicalite-1 upon SDA removal (**Table 2-1**).[3,79] No crack formation was detectable by SEM (**Figure 2-4**).

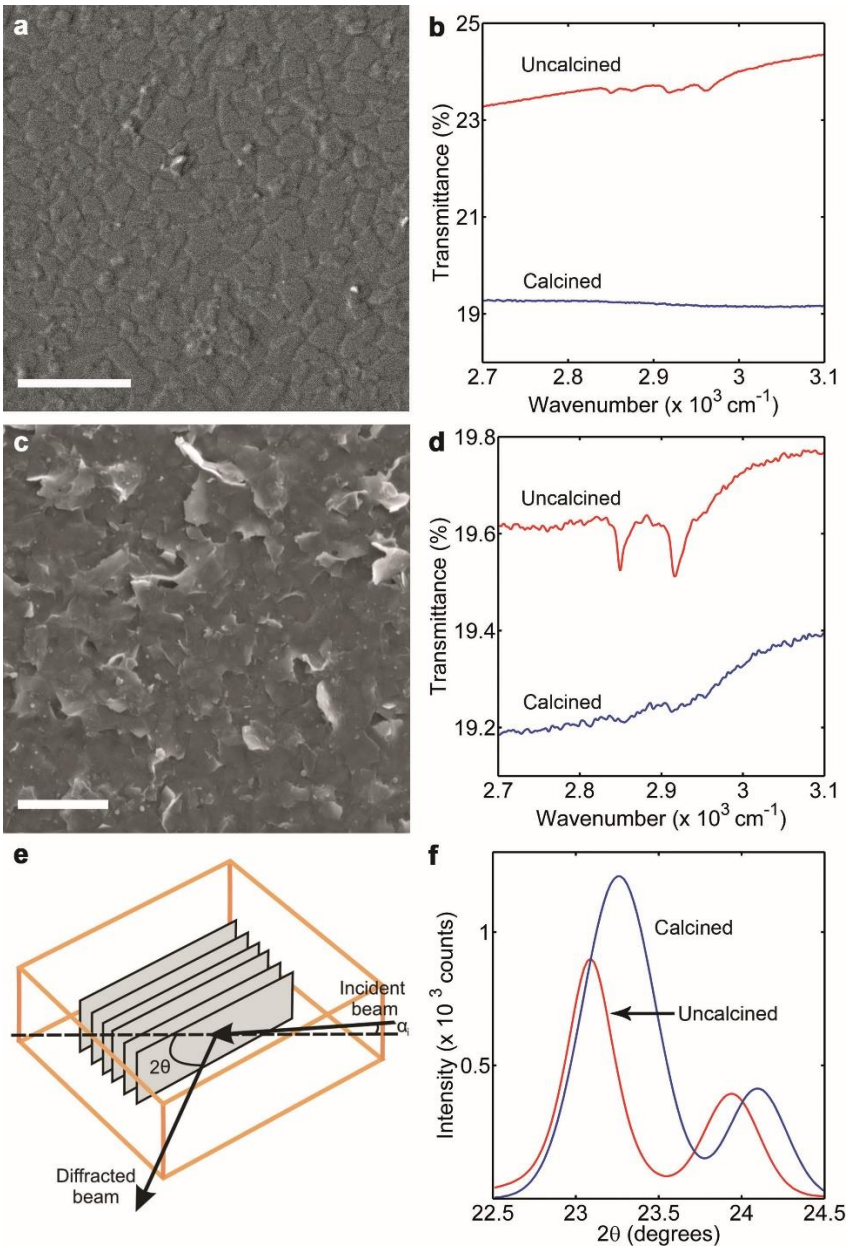

Figure 2-7. (a), (c) Single and multi-layer nanosheet films made by LS; scale bars: 1μm; (b), (d) FT-IR spectra obtained from nanosheet films similar to those shown in (a) and (c) respectively, showing that the peaks corresponding to SDA are absent after calcination; (e) Schematic of in-plane X-ray diffraction, where α_i is the angle of incidence and 2θ is the angle between the incident beam and the detector; (f) In-plane X-ray diffraction patterns obtained from a multi-layer nanosheet film

showing that there is in-plane contraction of the crystalline framework caused by SDA removal on calcination.

Table 2-1. (501) and (303) d-spacings (in Å) obtained from X-ray diffraction on multilayer LS coatings of nanosheets (see Figure 2-7f) and from bulk silicalite-1 (from www.iza-online.org).

hkl	Multilayer LS coating		Bulk silicalite-1	
	Uncalcined	Calcined	Uncalcined	Calcined
501	3.85	3.82	3.84	3.80
303	3.71	3.69	3.71	3.68

2.4.3. Secondary growth

After calcination, the deposited monolayers were subjected to secondary growth to obtain intergrown films. Depending on the secondary growth procedure and conditions, distinct microstructures were obtained. **Figures 2-8a and 2-8b** show SEM images of films after secondary growth, carried out with the nanosheet coating in direct contact with a TPA-silica sol[75,80] (5TEOS:1TPAOH:1000H_2O) and a TEAOH-silica gel[46] (4TEOS:1.92TEAOH:0.36$(NH_4)_2SiF_6$:40H_2O), respectively. In both cases, the substrates used were as-purchased silicon wafers. In the case of secondary growth using the TPA-silica sol, after hydrolysis and pretreatment of the sol at 150ºC, the coating is placed in the sol and heated to 90ºC in a sealed autoclave. After 5 hours, oriented films were obtained but some twinning was seen, a common occurrence for TPA-silica sol-based

secondary growth procedures. Specifically, a-oriented twins are visible in **Figure 2-8a** as thin protruding plates on the otherwise b-oriented film (see also **Figure 2-9a**).

For secondary growth using the TEAOH gel method, the solid gel was aged and then mixed by a blender. Nanosheet coating was inserted into the gel and heated to 150ºC in a sealed autoclave. The morphology obtained after 6 hours is shown in **Figure 2-8b**. Incomplete intergrowth was observed due to faster in-plane growth along the c-axis (see also **Figure 2-9d**). Further optimization of the secondary growth conditions in order to obtain thin and b-oriented films should be possible.

We also tried the "gel-less" method in which growth of MFI can be induced on a silicon wafer with oxide coating in the presence of TPA^+ ions.[40,48] Here, the silica source is not externally introduced but comes from the substrate. Nanosheet coatings deposited on silicon substrates with a 50 nm thermally-grown oxide (which acts as the silica source) are spin-coated with a very dilute TPAOH solution and heated to a high temperature (220ºC) for 72 hours. **Figure 2-8c** shows a top view SEM image of a representative film after gel-less secondary growth. An intergrown zeolite layer is obtained, which remains crack-free upon calcination. **Figure 2-10** shows additional SEM images from such films. **Figure 2-8d** shows in-plane XRD of the same film before and after calcination at 500ºC. Unlike the multi-layer as-deposited films of similar thickness (see **Figure 2-7f**), the intergrown MFI films do not exhibit changes in their in-plane crystallographic dimensions. This is probably a result of strong attachment to the support and to the neighboring grains by Si-O-Si bonds. Apparently, these films are under compressive strain but remain crack free.

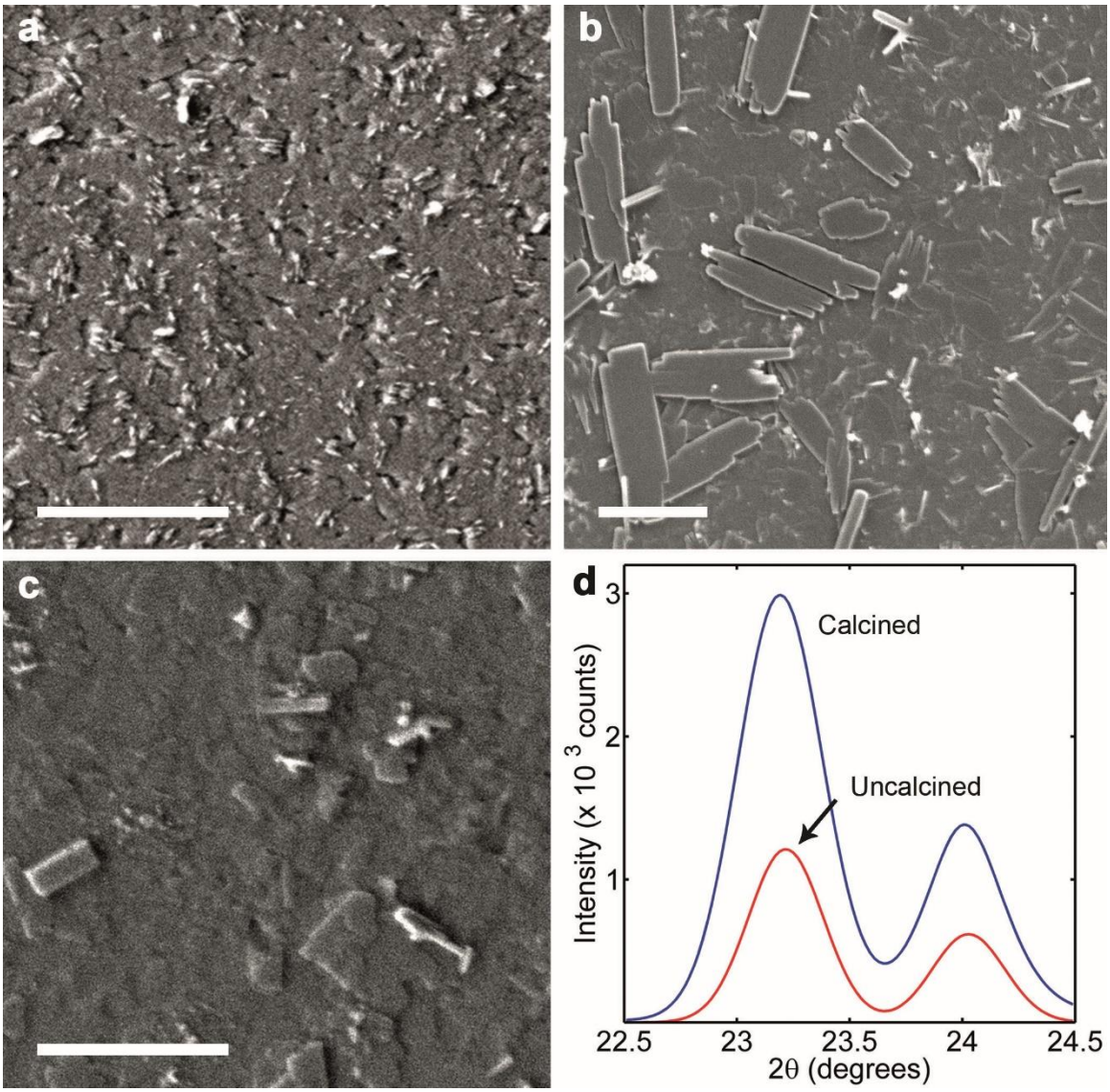

Figure 2-8. Secondary growth of single-layer nanosheet films using: (a) TPA-silica sol, (b) TEAOH silica gel and (c) gel-less growth using TPAOH; scale bars: 1μm. (d) In-plane X-ray diffraction before and after calcination at 500^{0}C obtained from the film shown in (c), indicating that there is no detectable in-plane crystallographic change caused by calcination.

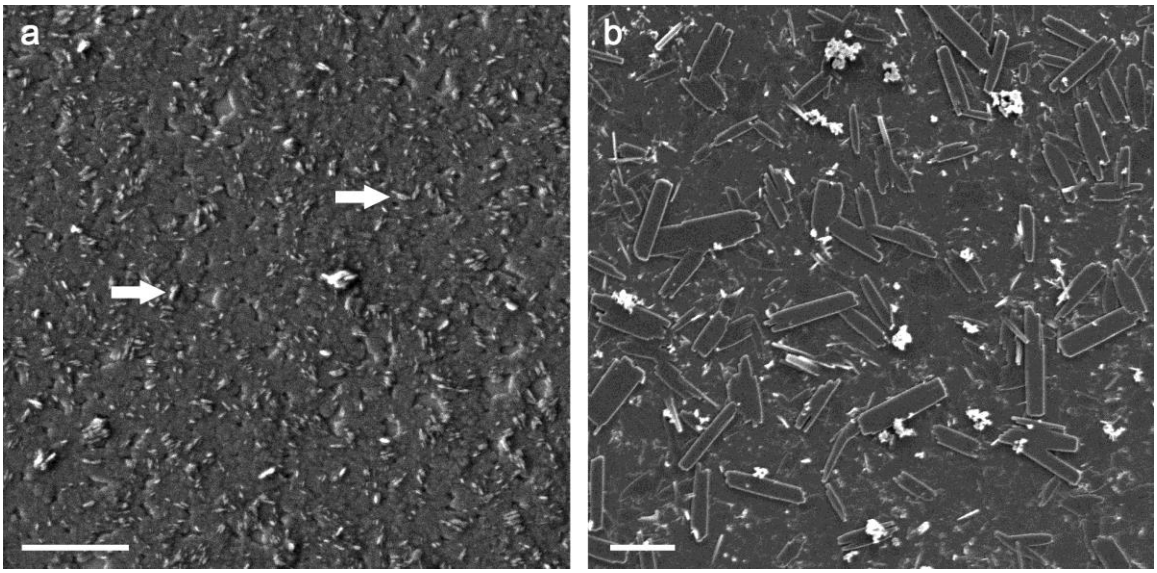

Figure 2-9. (a) Magnified image of film grown using TPA-silica sol-based method. Arrows indicate a-oriented twins. (b) Low magnification image of film grown using TEAOH silica gel method. Scale bars: 1 μm.

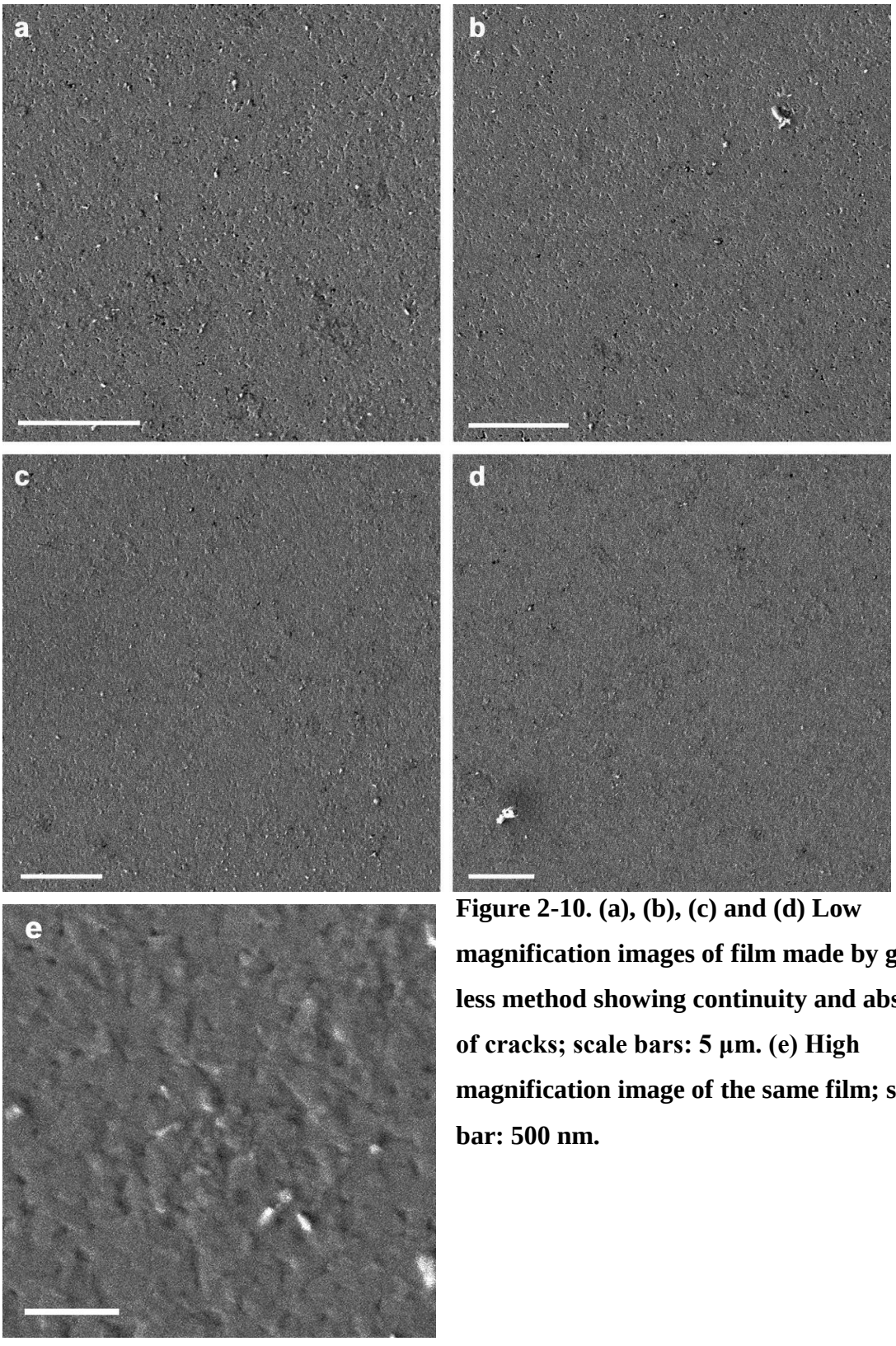

Figure 2-10. (a), (b), (c) and (d) Low magnification images of film made by gel-less method showing continuity and absence of cracks; scale bars: 5 µm. (e) High magnification image of the same film; scale bar: 500 nm.

2.4.4. Thickness determination of secondary-grown films

To determine the thickness of the films after gel-less growth, we prepared cross sections using focused ion beam (FIB) milling. The region containing Si and O is determined to be approximately 50nm (**Figure 2-11d**). This is comparable to the thickness of the SiO_2 thermal oxide layer, which was determined to be 48.8 ± 0.3 nm by ellipsometry. It was not possible to discriminate what part of this layer is SiO_2 and what part is zeolite, most likely due to amorphization of the zeolite layer by the FIB. Therefore, this technique is inconclusive in determining the exact thickness of the zeolite layer but it indicates that the film cannot be thicker than 50nm.

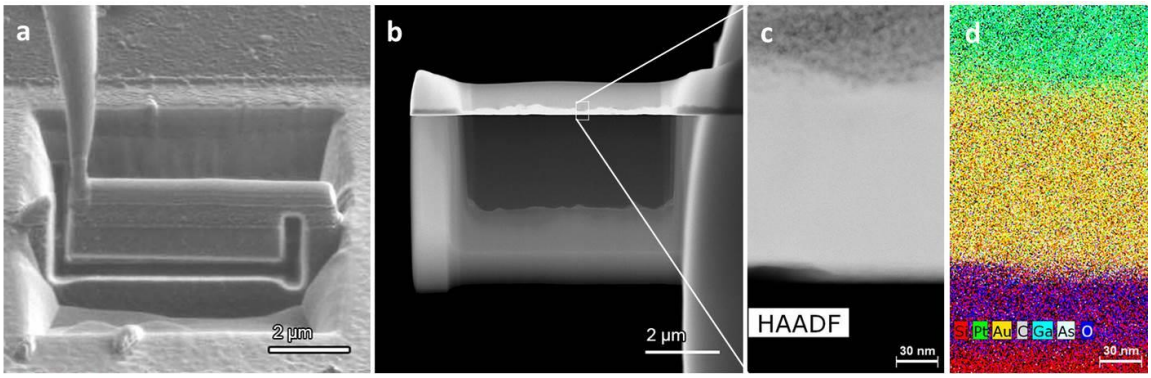

Figure 2-11. (a) Ion beam image showing a platinum and gold coated film before thinning by a focused ion beam. (b) HAADF-STEM image of a ~70 nm thin section shown in (a). Heavier atomic number (Z) elements appear brighter in the STEM image. (c) HAADF-STEM image of a 150 nm x 250 nm section from (b). (d) Spatially resolved STEM EDX composite map showing the distribution of elements in the section shown in (c). The thickness of the SiO_2 + MFI layer is ~50 nm.

To resolve the issue of zeolite film thickness, we have used sparse monolayers by depositing them at low pressures (see **Figure 2-3b**). When these layers were grown using gel-less secondary growth conditions identical to those of **Figure 2-8c**, they do not cover the entire substrate allowing one to measure the thickness of the intergrown regions by reference to the near-by exposed substrate surface. From these measurements, we determine the thickness to be less than 12 nm (**Figure 2-12**).

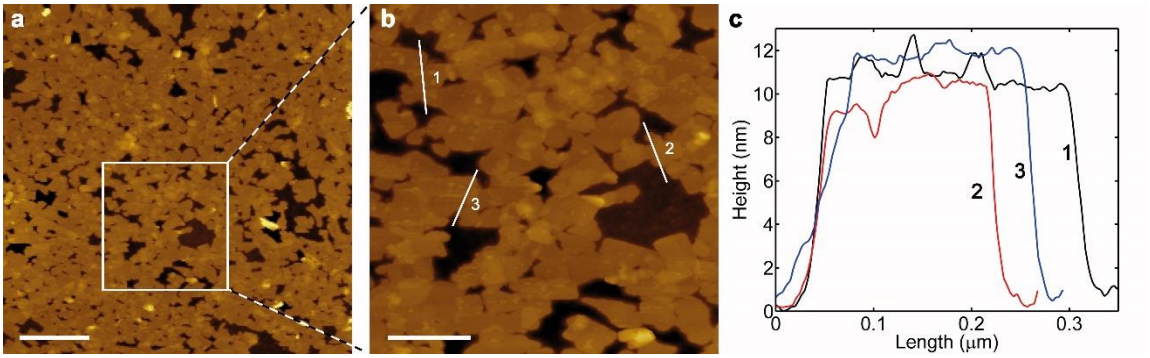

Figure 2-12. (a) Low magnification AFM image of gel-less secondary grown film. The initial seed layer was sparse resulting in gaps where substrate is visible. Scale bar: 1 μm. (b) Magnified image of area shown in (a); scale bar: 400 nm. (c) Height profiles corresponding to the lines in (b) show that the film thickness does not exceed 12 nm.

2.5. Conclusions

In this chapter, the acid treatment of MFI nanosheets has been described. It facilitated partial removal of the SDA without altering the zeolite crystal structure and thickness. This allowed for nanosheets to be dispersed in ethanol and subsequently transferred to the air-water interface. Using the Langmuir-Schaefer deposition technique, nanosheets could be transferred to solid substrates to form monolayer coatings ranging from sparse to close-packed. Successive depositions resulted in oriented multi-layer films with control over their thickness, while secondary growth of monolayers yielded intergrown, oriented films with sub-12 nm thickness. This unprecedented control over thickness and orientation uniformity of zeolite films may open new opportunities for investigating adsorption, transport, dielectric and mechanical properties of zeolites.

Chapter 3

Sub-Micron Zeolite Films for Low-Dielectric Constant Applications[‡]

[‡]Portions of this chapter appear in the following:

R. Tiriolo*, N. Rangnekar*, H. Zhang, M. Shete, P. Bai, J. Nelson, E. Karapetrova, J.I. Siepmann, E. Lamanna, A. Lavano and M. Tsapatsis, *Adv. Func. Mater.*, Accepted

*Equally contributing authors

3.1. Chapter overview

In this chapter, a low temperature process for fabrication of *b*-oriented MFI films on gold-coated silicon wafers for low-dielectric constant applications is described. Seeds of the zeolite MFI were assembled by a manual assembly process and subjected to optimized secondary growth conditions that do not cause corrosion of the gold underlayer, while strongly promoting in-plane growth. The traditional calcination process was replaced with a non-thermal photochemical activation to ensure preservation of an intact gold layer. The dielectric constant (k), obtained through measurement of electrical capacitance in a metal-insulator-metal configuration, highlights the ultra-low $k \sim 1.7$ of the synthetized films, which is among the lowest values reported for an MFI film. There is large improvement in elastic modulus of the film ($E \sim 54$ GPa) over previous reports. The values of k and E are close to the theoretically predicted values for single-crystal

MFI. These results could potentially allow for integration into silicon wafer processing technology.

3.2. Introduction

As transistor sizes in semiconductor integrated circuits (IC) are being reduced, low-*k* dielectric materials are required to insulate different components and prevent leakage current which can compromise performance.[17,81] Such materials must satisfy two major requirements:[16,82] (1) Dielectric constant (*k*) smaller than that of silicon dioxide (*k* = 3.9) which is the currently used low-*k* material and (2) elastic modulus (*E*) as high as possible, with *E* > 6 GPa preferable to allow the film to withstand the abrasive polishing processes in IC manufacturing.

All-silica zeolites are good candidates for low-*k* applications because their porosity gives them a dielectric constant significantly lower than that of silicon dioxide (*k* = 3.9).[83] and their elastic modulus can be very high (50-60 GPa in single-crystal zeolites).[54] However, the previously reported zeolite film fabrication techniques have limitations for low-*k* applications. Two different processes have been previously used to prepare low-*k* zeolite films: *in situ* crystallization[64,84–87] and spin-on[88–96] deposition of zeolite crystals. *In situ* crystallization allows for the fabrication of high mechanical strength zeolite films. However, the hydrothermal synthesis and post-synthesis calcination temperatures often exceed the ~130°C limit for silicon-based ICs.[97] Moreover, for sensing applications, high temperatures can lead to rearrangement of the metal underlayer, increased surface roughness and decreased conductivity.[98,99] In the case of spin-on films, the fabrication

process can be more easily integrated with IC manufacturing technology.[84] However, an increase in the porosity of the film results in reduction of the mechanical strength.[100–102] For silicalite-1 (pure-silica form of MFI) films, there have been recent advances in synthesis procedures, which allow for fabrication of thin and highly *b*-oriented films. A process called manual assembly has previously been used to obtain a *b*-oriented seed monolayer.[103] Secondary growth of these seed layers when brought in contact with silicate gels containing the structure directing agent (SDA) tetraethyl ammonium hydroxide (TEAOH) has been shown to result in highly *b*-oriented, continuous films.[76] Recently, this approach has been extended to low-temperature secondary growth of MFI nanosheets using clear TEAOH silicate sols .[47]

In this chapter, we show that these techniques for synthesis of sub-micron, *b*-oriented MFI films on gold-coated silicon wafers for low-*k* applications. The mild conditions used prevent damage to the gold film. Further, detemplation was performed by mild ultraviolet (UV) treatment instead of thermal calcination, to further reduce substrate damage. The dielectric constant and elastic modulus of these films show large improvements over those reported earlier.

3.3. Experimental

3.3.1. Materials

Tetraethyl orthosilicate with chemical formula $Si(OC_2H_5)_4$ (TEOS, 98%, Sigma-Aldrich), tetrapropylammonium hydroxide (TPAOH, 1 M in water, Sigma-Aldrich),

tetraethylammonium hydroxide (TEAOH, 35 wt% in water, Alfa Aesar), deionized (DI) water, silicon wafers (orientation: (100)) used as purchased from Minnesota Nano Center.

3.3.2. Characterization

Scanning electron microscopy (SEM) was performed using a JEOL 6700 scanning electron microscope at 1.5 kV and 10 mA emission current. Cross-sectional preparation and imaging was carried out in an FEI Quanta 200 3D focused ion beam SEM. High-resolution synchrotron X-ray diffraction (XRD) was performed at beamline 33-BM-C at Argonne National Laboratory, with a monochromatic X-ray beam of wavelength 0.7847 Å. Attenuated total reflectance–Fourier transform infrared spectroscopy (ATR-FTIR) measurements were made by using a Nicolet Series II Magna-IR System 750 FTIR. The zeolite film supported on the silicon wafer was directly placed on the IR window, with the film surface exposed to the IR beam. The elastic modulus was measured using an MTS NanoXP using a Continuous Stiffness Method.

3.3.3. Fabrication of gold-coated semiconductor supports

The silicalite-1 films were firstly deposited and synthesized directly on gold-coated silicon wafers. The metal coating on silicon substrate was performed by sputtering of different metals using an AJA-2 Sputter RF-DC deposition system (model number: ATC 2200). First, the wafer was coated with a layer of 50 nm thick chromium to form an adhesion layer between gold and silicon wafer surface. Following this, the metal-coated

wafer was coated with 50 nm thick layer gold. Si (100) wafers were used as obtained from the manufacturer.

3.3.4. Synthesis of MFI seed crystals

MFI seed crystals with lengths along the *a*-, *b*- and *c*-axis of approximately 1.0, 0.5 and 1.4 µm, respectively, were synthesized according to an established method.[16] In brief, TEOS, TPAOH and DI water were combined in a molar ratio of 6:1.28:620 in a beaker under stirring. The mixture converted to a clear sol after stirring for 24 hours. It was then filtered using a Whatman 0.2 µm GHP syringe filter into Teflon-lined autoclaves. The autoclaves were placed in an oven set to 150 ^{o}C and continuously rotated. After 12 hours, the autoclaves were removed, cooled and the contents were centrifuged to obtain the MFI zeolite powder. The cake was washed with DI water and centrifuged 3 times to reduce the pH to neutral. The powder was then dried at 70 ^{o}C and calcined at 550 ^{o}C under air flow of 150 sccm. Finally, the powder was characterized by SEM to image the crystal size and morphology and XRD to verify that the crystals are MFI.

3.3.5. Manual assembly of b-oriented zeolite crystals on silicon wafer

The MFI powder was manually assembled on the surface of the gold-coated Si wafer according to a method that has previously been described.[46,104] A small amount of powder was placed on the gold-coated side of the wafer and rubbed using a gloved finger (latex or nitrile glove). The rubbing was done until the surface of the wafer appeared

shiny to the eye and excess powder had been removed. The assembled zeolite film was characterized by SEM to image the packing and orientation of the film.

3.3.6. Secondary growth to form a continuous b-oriented zeolite film

The assembled zeolite film on Si wafer was placed at the bottom of a Teflon-lined autoclave with the zeolite-coated side facing up. The composition for the gel was 1TEOS:0.48TEAOH :0.09$(NH_4)_2SiF_6$:*y*H_2O and for clear solution it was 1TEOS:0.2TEAOH:100H_2O. Secondary growth gel/sol was made according to a previously described method (for gel we used the procedure for Gel-2 preparation in ref.[46] and for clear sol we used the procedure described in ref.[47]). After several trials, we concluded that the gel caused etching and peel-off of the gold layer in most cases while the sol did not lead to damage of the gold layer. Here, we describe only the process for sol-based secondary growth.

TEAOH and water were combined under stirring in a beaker. TEOS was added slowly to it and the mixture was left under stirring at room temperature. After 24 hours of hydrolysis, the solution was filtered through a Whatman 0.2 μm GHP syringe filter into the Teflon-lined autoclave in which the zeolite film had been placed. The autoclave was placed in an oven set to 120 °C in static condition for different durations. Following this, the autoclave was cooled and the Si wafer was removed, washed with DI water and dried at 70 °C. The combinations of synthesis time and *y* are shown in Table S-1. In order to ensure complete intergrowth of the crystals and eliminate gaps, the secondary growth procedure was repeated one more time.

The film was then characterized using SEM (to image film morphology), ATR-FTIR (to characterize SDA content of film before and after UV treatment), synchrotron XRD (to characterize the orientation and change in crystallographic dimensions on SDA removal) and focused ion beam SEM (to measure film thickness).

3.3.7. UV-ozone activation of zeolite film

The film surface was exposed to UV light for different periods of time with the aim to remove the organic structure directing agent (SDA) molecules occluded in the pores. In order to compare the effects of both photochemical and thermal activation, each sample was cut into two pieces. One of the two pieces was calcined by a traditional procedure according to which samples are heated to 500 °C with a heating rate 1ºC/min and kept at 500 °C for six hours. The other piece of the sample was exposed to a photosensitized oxidation processes by using a Jelight UVO-cleaner, (Ultraviolet light ranging from 185 nm and 254 mm coupled with ozone) for 12 h, 24 h, 36 h, 48 h and 72 h.
The removal of the occluded SDA species was investigated by ATR-FTIR, analyzing each sample both as-synthetized and after UV treatment or thermal calcination.

3.3.8. Parallel plate capacitor and vacuum chamber setup for dielectric constant measurement

To measure the electrical capacitance of the films, a parallel plate capacitor configuration (metal-insulator-metal) was used (see **Figure 3-4b**). Prior to the deposition of the precursor layer, a small region of the gold coated substrate was wrapped with Teflon tape

to prevent zeolite deposition in that region. After the secondary growth of the precursor layer the tape was removed and the sample was rinsed with DI water. Crystal growth was not observed in the space covered by Teflon and it has been utilized as one of the two capacitor plates. Six 1 mm aluminum dots were deposited by metal sputtering on the zeolite films through a shadow mask, in order to obtain the top parallel plate. The capacitance of the zeolite films was measured inside a glass vacuum chamber connected to an electrical pump. The grid of the chamber was fabricated with conductive material and equipped with a Faraday cage and two on-fit micro-positioners. The micro-positioners were drawn by Rhinoceros, fabricated by 3-D printer and equipped with sliding supports, scrubs and springs in order to obtain very sensitive displacements of the probes. Two gold-coated and round tip needles were fixed on the tips of the two micro-positioners. Two cables connected the probes to a voltage generator. They were fixed on the chamber cap through a hole in the glass and then linked to a Hewlett Packard 4284A LCR (inductance-capacitance-resistance) meter. The settings of the LCR meter are shown in Table S-3. In order to obtain a reliable measurement, the capacitance was measured inside the chamber at a pressure of 10^{-3} Torr, to prevent alteration of zeolite film capacitance due to adsorption of water and organics. Capacitance was measured at all 6 aluminum dots on each film and then averaged.

The dielectric constant was calculated by the equation:

$$\kappa = \frac{Cd}{\varepsilon_0 A} \quad (1)$$

Where C is the measured capacitance (F), d is the film thickness (m), A is the area of 1 mm metal dot (7.85 x 10^{-5} m^2) and ε_0 is the vacuum permittivity of 8.854 x 10^{-12} m^{-3} kg^{-1} s^4 A^2.

3.3.9. Measurement of elastic modulus

As described previously,[105] nanoindentation was used to measure the elastic modulus (E), which was calculated dynamically as a function of indentation depth. Data was collected with the MTS NanoXP using a Continuous Stiffness Method first described by Oliver and Pharr. Multiple (>10) indentations were made on each specimen with a Berkovitch diamond (3-sided pyramid). Total depth of each was 500 nm but only the data from 25-50 nm were utilized. Data from below 25 nm were unreliable due to calibration limitations. Above 50 nm the effect of the stiffer substrate became noticeable. The values between 25 and 50 nm were averaged for each indent and then those averages were averaged for all indents on a particular specimen.

3.3.10. Simulation of dielectric constants for MFI

We have also probed the relative permittivity of an MFI single crystal with empty pores using density functional perturbation theory.[106,107] Table S-2 summarizes computed high- and low-frequency dielectric constants. At the high-frequency limit, the framework nuclei are assumed to be immobile and unable to respond to changes in the external electric fields. A value of 1.96 was found for an empty MFI zeolite along the *b*-direction

(with similar values for the *a* and *c* directions), which agrees well with the experimental result of 1.71 measured for a *b*-oriented MFI film at a voltage frequency of 1 MHz. Dielectric constants were calculated via density functional perturbation theory[106,107] for an empty MFI zeolite. The Vienna Ab initio Simulation Package, version 5.4.1[107,108], was used to perform the periodic Kohn-Sham DFT calculations using the PBE exchange-correlation functional[109], PAW pseudopotentials[108], and a plane-wave basis set with a kinetic energy cutoff at 400 eV.

3.4. Results and Discussion

3.4.1. Deposition of seed layers on gold-coated silicon wafers

MFI seed crystals were obtained by using a previously reported hydrothermal growth procedure.[76] As seen from **Figure 3-S1a**, the average crystal dimensions along the *a*, *b* and *c* crystallographic axes were 1.0 x 0.5 x 1.4 μm^3, respectively. The substrate used was a silicon wafer coated with a metal adhesion layer (nickel, titanium, or chromium) on top of which a gold film was sputtered. After optimization, it was found that the gold/chromium combination, with thickness of each layer being 50 nm, had the best adhesion and resistance to corrosion during hydrothermal secondary growth.

The assembly of monolayers of MFI crystals on gold-coated silicon wafer substrates was performed through the direct attachment by hand (rubbing),[40,103] without using solvents, chemical treatments or adhesive layers to promote binding to the substrate. A small part of the substrate was covered with Teflon tape prior to manual assembly, in order to prevent the attachment of zeolite crystals in this area. After the film synthesis this

uncoated area was used as one of the electrodes for capacitance measurement. As seen in **Figure 3-S1b**, the crystals are highly *b*-oriented and close-packed. Despite the simplicity of this deposition technique, the rubbed precursor films show good adhesion to the substrate.

3.4.2. Secondary growth

In order to intergrow the film and form a continuous layer, hydrothermal secondary growth was performed. A strategy that has been shown earlier for obtaining *b*-oriented MFI films is to replace the commonly used SDA tetrapropyl ammonium hydroxide (TPAOH) with tetraethyl ammonium hydroxide (TEAOH).[76] This approach avoids the formation of twinned crystals, which usually form during growth with TPAOH, and leads to a highly *b*-oriented film. However, this approach is not applicable here. Some of the attempted combinations of such growth are given in Table S-1. During secondary growth with TEAOH gel (1TEOS:0.48TEAOH:0.09$(NH_4)_2SiF_6$:yH_2O, with y = 50 or less), at a temperature of 120ºC, etching, peel-off and corrosion phenomena were evident, along with incomplete growth in certain areas (see **Figure 3-S2**). Clearly, a different approach is required in order to avoid damaging the gold layer.

Recently, it was shown that secondary growth using dilute TEAOH clear sols with temperatures ranging from 110-130ºC can result in faster in-plane (compared to out-of-plane) growth for MFI,.[47] These conditions, when attempted on the gold-coated silicon substrates, led to little to no damage to the gold layer. After some trials, we determined that a sol with composition 1TEOS:0.2TEAOH:100H_2O and a hydrothermal growth

temperature of 120ºC led to highly intergrown crack-free films. Since the growth rate is slow at lower temperatures, two cycles of secondary growth were performed. The first growth was carried out for 5 days and a subsequent growth with fresh sol was carried out for 3 days. A continuous and defect-free, *b*-oriented MFI film was obtained, as shown in **Figure 3-1a**. The thickness of the synthesized films was determined following focused ion beam (FIB) cross-sectioning. The FIB image (**Figure 3-1b**) indicates that the thickness of the MFI film synthesized on gold/chromium coated silicon wafer, below an aluminum dot deposited on the top of the film, is 0.55±0.1 µm.

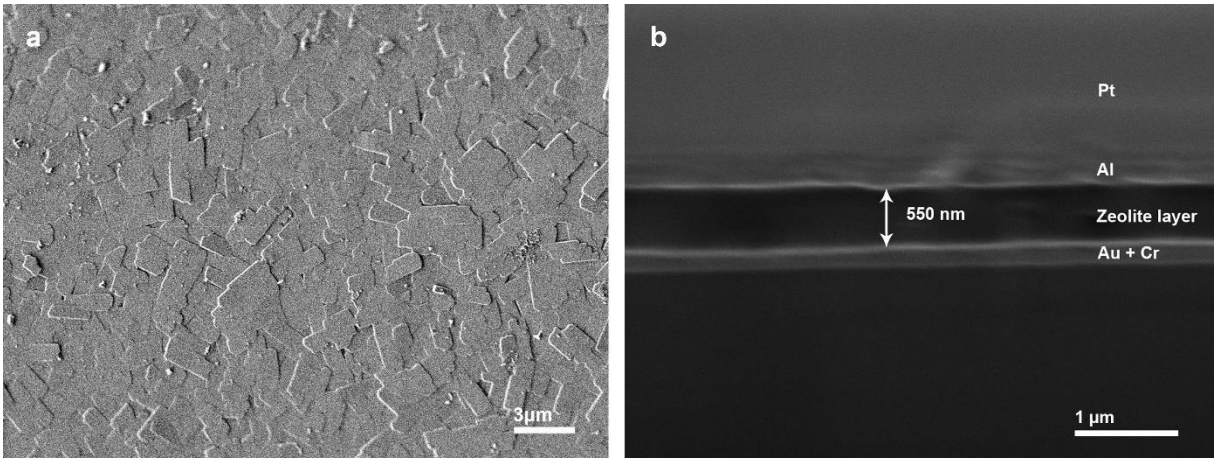

Figure 3-1. Scanning electron microscopy (SEM) images of: a. top surface of MFI film after secondary growth of the seed layer and b. cross section (made by focused ion beam (FIB)) of the film shown in (a) demonstrating that the thickness of zeolite layer is ~550 nm.

3.4.3. UV-ozone treatment for SDA decomposition

Unlike earlier reports on zeolite film fabrication, calcination is not suitable in this case, because it can lead to rearrangement of the sputtered gold film and increase in its surface

roughness.[110] In addition, after calcination the film can suffer from crack formation due to thermal expansion mismatch between film and substrate.[111,112] We have avoided the use of calcination, by carrying out UV-ozone treatment, which has been previously shown to be successful for SDA decomposition.[41,113] UV-ozone allows for decomposition of SDA at low temperature through photo-induced chemical reactions, in which the organic species are disintegrated by ozone and atomic oxygen generated by UV radiation. **Figure 3-2a** shows the attenuated total reflection Fourier transform infrared (ATR-FTIR) spectrum of the film as synthesized compared with those obtained after 72 h UV-ozone treatment or after thermal calcination. The inset highlights the three bands centered at 2980 cm^{-1}, 2942 cm^{-1} and 2880 cm^{-1}, assigned to the methyl ($–CH_3$), methylene ($–CH_2–$) and methyne (–CH) stretching vibrations, respectively, associated with the presence of the SDA.[114] These bands are not present in the spectra of the UV-treated and the calcined samples. The comparison of UV-treated and calcined spectra indicates that the removal of SDA achieved through UV-ozone treatment is comparable to thermal calcination. **Figure 3-2b** shows the spectra obtained from the same film after 12, 24, 48, and 72 h UV exposure. These results show that the intensity of the peaks assigned to SDA C-H stretching vibrations decrease with exposure time, and become undetectable after 72 hours of UV-ozone treatment.

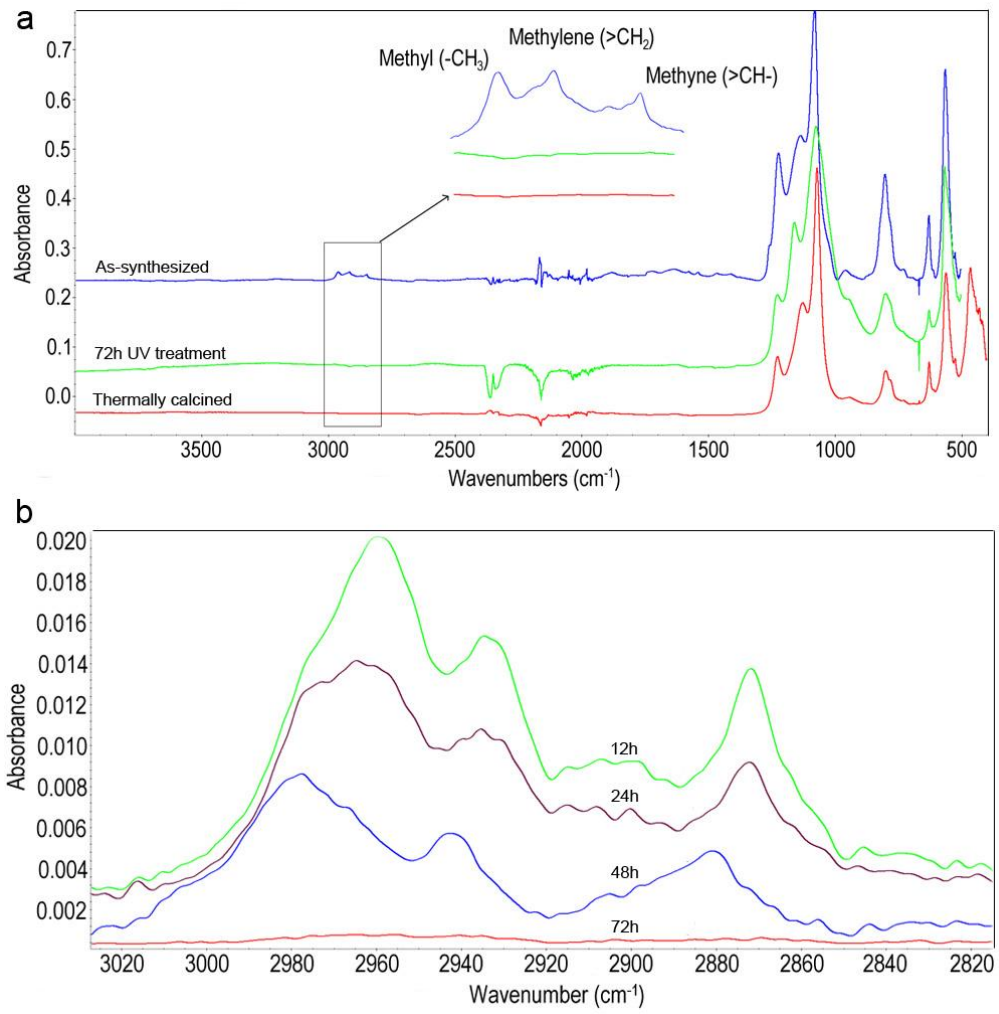

Figure 3-2. a. ATR-FTIR spectra of zeolite films: As-synthesized, after 72 h UV-ozone treatment and thermally calcined, b. Decreasing IR bands assigned to SDA after 12, 24, 48, and 72 h UV-ozone exposure.

3.4.4. Characterization of films by synchrotron X-ray diffraction

In addition to ATR-FTIR, synchrotron X-ray diffraction (XRD) was used to characterize the films before and after SDA removal. This technique which has been previously used to determine calcination-induced crystallographic changes in a thick *c*-oriented MFI membrane.[115] We have also recently used XRD to monitor calcination induced in-plane

(parallel to substrate) contraction of MFI nanosheets before and after secondary growth.[49]

Here, performed synchrotron XRD on secondary-grown films in both in-plane and out-of-plane modes was performed. As illustrated in **Figure 3-3a**, in-plane peak shifts are absent indicating that the film is strongly bound to the substrate and does not undergo contraction after calcination. This finding agrees with our previous results for secondary grown films.[49] In **Figure 3-3b**, only the *b*-out-of-plane peaks are visible, i.e. (020), (040), (060), (080) and (0100). This pattern demonstrates the highly *b*-oriented nature of the synthesized films. In contrast with the absence of detectable changes in the in-plane XRD, in the out-of-plane XRD patterns obtained from the detemplated films, the peak positions shift to slightly higher angles compared to the positions from as-synthesized films. This shift corresponds to a detemplation-induced decrease of the *b*-axis dimension from 19.85 Å to 19.83 Å. The FTIR and XRD results demonstrate that the SDA molecules can be removed by UV-ozone treatment without causing in-plane crystallographic changes. Only a small contraction of the MFI film in the direction perpendicular to the substrate is detectable after calcination.

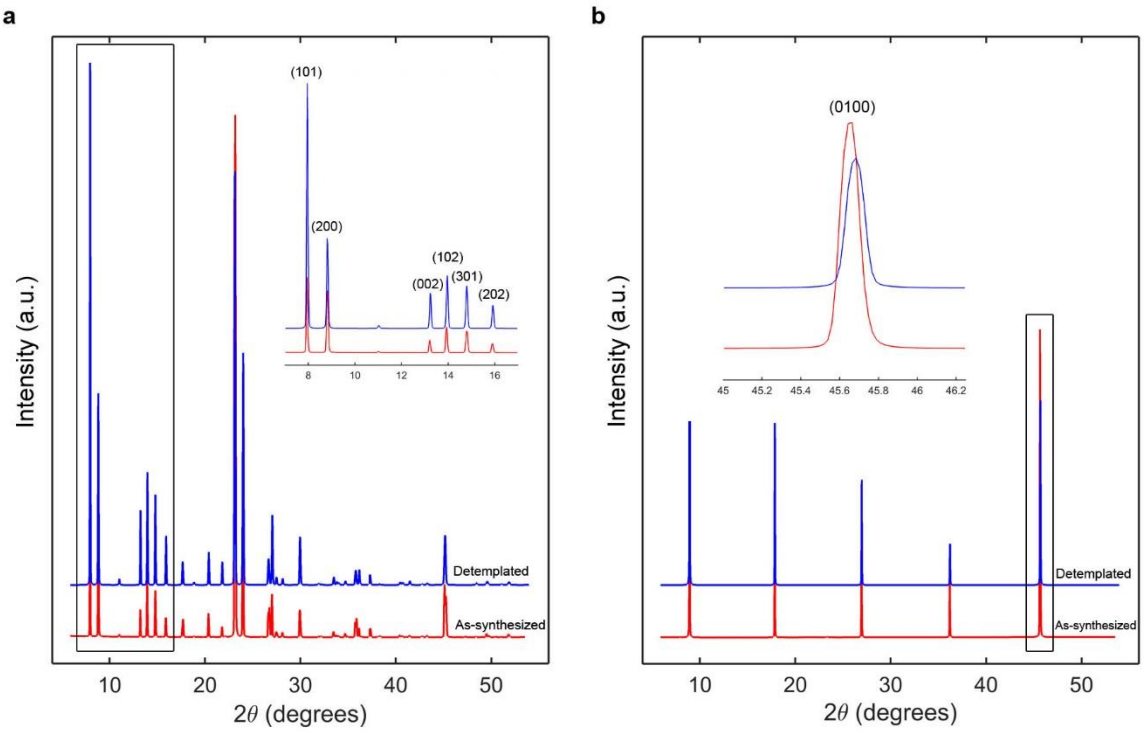

Figure 3-3. Synchrotron X-ray diffraction patterns of as-synthesized (red) and detemplated (blue) MFI films. a. In-plane X-ray diffraction patterns. Inset shows that there are no peak shifts, indicating that the film does not expand or contract in the in-plane direction. b. Out-of-plane X-ray diffraction patterns of the same films. Inset shows that during calcination the film contracts slightly in the *b*-direction.

3.4.5. Measurement of dielectric constant and elastic modulus of intergrown films

Following synthesis and characterization of the film, a metal-insulator-metal configuration aimed at measuring the electrical capacitance of the zeolite film was achieved. Here, the exposed gold substrate is connected to one electrode, while an aluminum dot on the surface of the zeolite film is connected to the other electrode. This configuration allows for direct measurement of the true capacitance of the zeolite layer, unlike previously reported methods which included the silicon substrate in the

measurement.[88,116] By eliminating the substrate from the measurement, we eliminate its effect on the capacitance along with any associated measurement uncertainties (e.g., caused by the doping of the silicon wafer). The differences between the current configuration enabled by the gold layer and the previously used one are illustrated in **Figures 3-4b and 3-S3**.

The measurements were performed inside a chamber equipped for capacitance measurement under vacuum conditions, with the aim of preventing humidity and contamination with organic vapors in order to evaluate the intrinsic relative permittivity of the films. An average *k* value of 1.71±0.08, measured for 3 films at a voltage frequency of 1 MHz, was obtained. This is among the lowest *k* values ever reported for a MFI film and is close to the computed value corresponding to a perfect all-silica MFI single-crystal (see **Figure 3-4a** and **Table 3-S2**).

The mechanical integrity of the films is another major requirement for low-*k* application, and it can be assessed through measurement of the elastic modulus. This was done using the previously established procedure of nanoindentation.[54,105] The average value of the elastic modulus obtained from measurements for 3 films is 54±6 GPa. This elastic modulus is much higher than those previously reported for synthesized low-*k* spin-on zeolite films, and is again close to the value obtained by simulations for a single-crystal of MFI (see **Figure 3-4a**). The combination of low dielectric constant and high elastic modulus makes the sub-micron MFI films produced here an excellent potential candidate for low-*k* application in an integrated circuit. Future work should involve reduction in film thickness (to <100 nm) to obtain films suited for low-k applications. Moreover, the

in situ dielectric response of these films to adsorbates could be studied as a way towards sensing applications.

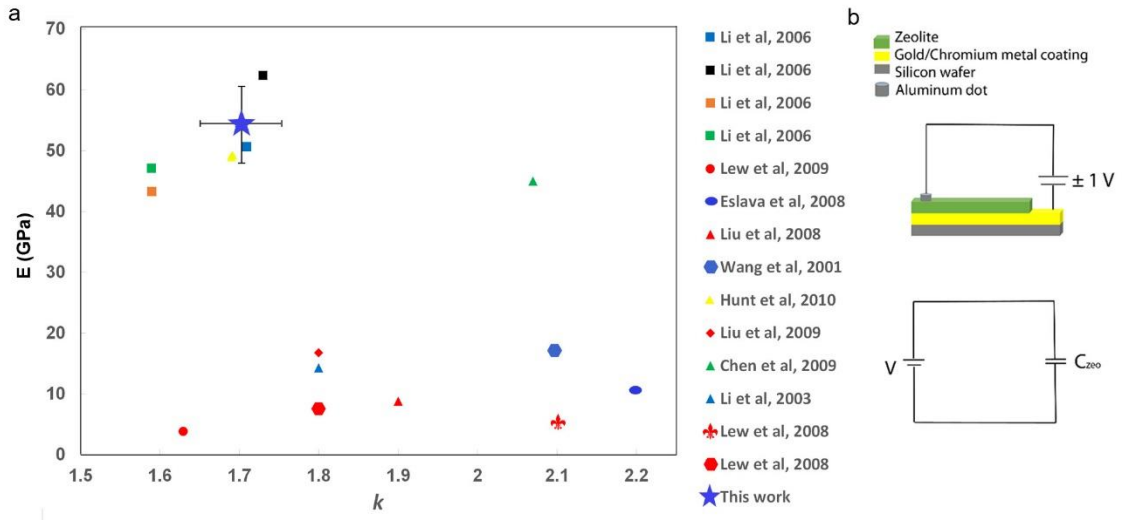

Figure 3-4. a. Elastic modulus (GPa) vs. dielectric constant, comparing this work to prior reports on zeolite films for low-*k* applications. The values found here are comparable to the simulated values for single-crystal MFI (blue square). The dielectric constant is close to the lowest value obtained for MFI films. Color code for zeolite type used – Blue: MFI, Red: MEL, Black: FER, Green: BEA, Orange: CHA, Yellow: LTA. Square symbols correspond to the simulated values of *E* and *k* for zeolite single-crystals with different framework structures.[54] b. Configuration for capacitance measurement (top right) with the equivalent circuit shown (bottom right).

3.5. Conclusions

In this chapter, we have described the fabrication of a metal-insulator-metal configuration by depositing a 550 nm, well-intergrown, *b*-out-of-plane oriented, all-silica MFI zeolite film on gold-coated silicon wafers. The zeolite film deposition method consists of an oriented seed deposition step, and a novel combination of a secondary growth step using

a clear silica tetraethylammonium sol, and a UV-ozone activation step that removes occluded organic molecules. The *k* and *E* achieved are close to the theoretically predicted values for single-crystal MFI, and constitute a significant improvement over previous reports. As the feature size of computer chips reduces further, low-*k* films such as these could potentially play an important role in energy efficiency.

3.6. Supporting Information

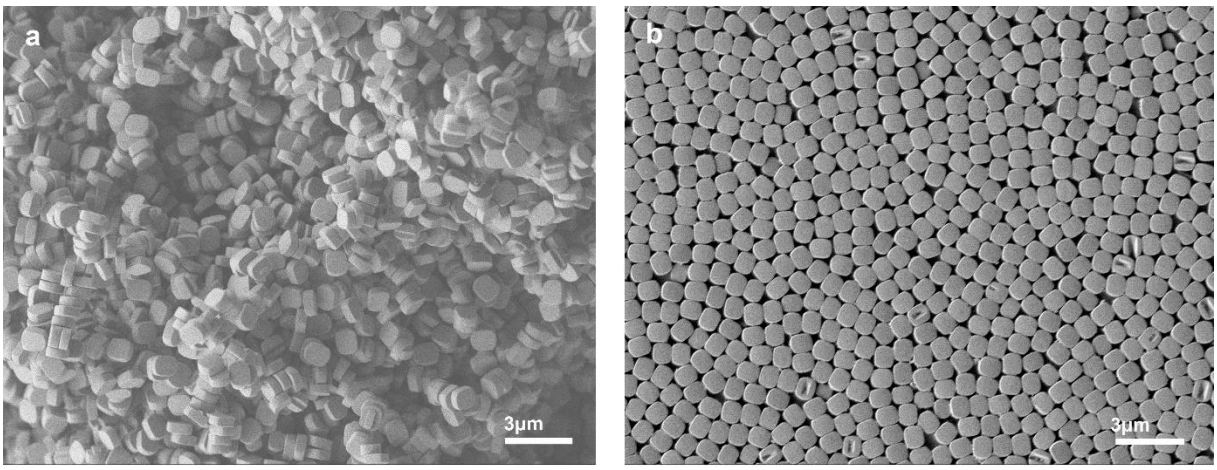

Figure 3-S1. SEM images of: a. as-synthesized MFI seed crystals and b. MFI crystals on gold-coated silicon wafer after manual assembly.

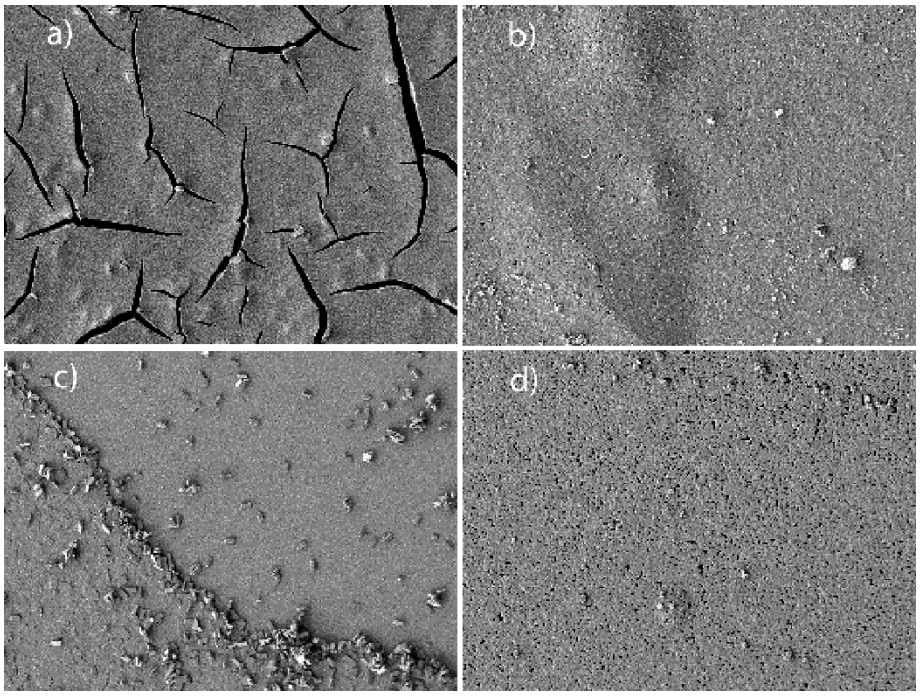

Figure 3-S2. SEM images showing a. film cracks (sample 1), b. peel-off of gold layer (sample 3), c. film peel-off (sample 2), and d. incomplete film growth (sample 4). Refer to Table S-1 for growth conditions of the respective samples.

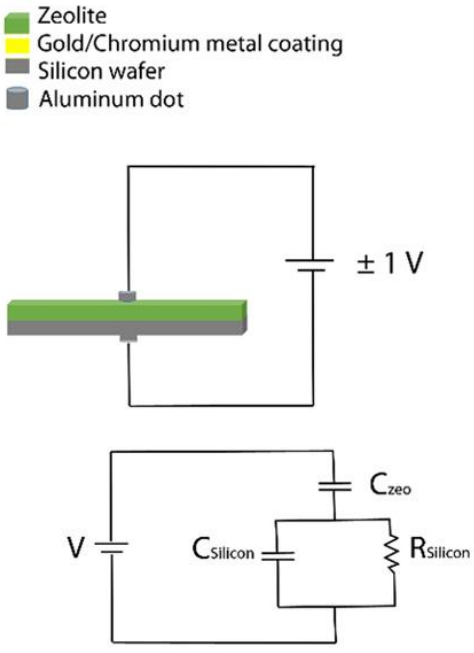

Figure 3-S3. Schematic of previously reported[84] capacitance measurement configuration (top) and the equivalent circuit (bottom).

Table 3-S1. Secondary growth conditions with different combinations of secondary growth time, DI water to TEOS ratio (*y*), and result obtained after the growth. Temperature was 120 ºC in all cases.

Sample No.	Growth time (days)	*y*	Result
1	3	10	Au etching / film cracks
2	5	20	Au etching / film peel-off
3	3+5	50	Defects / Au peel-off
4	3	100	Partial growth
5	5	100	90% surface coverage / defects
6	5+3	100	Full coverage / no defects

Table 3-S2. Calculated dielectric constants for zeolite MFI with an empty framework at the high- and low-frequency limits.

Direction	Dielectric constant	
	High	Low
a	1.97	3.41
b	1.96	3.35
c	1.94	3.29

Table 3-S3. LCR parameters for capacitance measurements.

Parameter	Set value
Starting voltage	−1V; −5V
Stopping voltage	+1V; +5V
Voltage step size	0.05 V
Step delay time	0.01 sec
Maximum leakage current	0.1 mA
Voltage frequency	1 MHz
Terminal contact surface area	0.00785 cm^2

Chapter 4

A Review of Advances in Zeolite Membranes ‡

‡Reproduced from N. Rangnekar, N. Mittal, B. Elyassi, J. Caro and M. Tsapatsis, *Chem. Soc. Rev.* **2015**, *44*, 7128-7154, with permission from The Royal Society of Chemistry.

4.1 Chapter overview

This chapter describes the recent advances in zeolite membranes. First, progress in fabrication techniques is presented, which includes synthesis of seed crystals, coating techniques for seed deposition and secondary growth methods. The recent developments in sub-1 um membranes and polymer membranes are highlighted. A major constraint for industrial application of zeolite membranes has been the low flux and high cost, which make the required membrane area economically unviable. With an order of magnitude reduction in zeolite membrane thickness and by using less expensive polymer supports, there are now new opportunities for industrial applications. The current industrial applications of zeolite membranes are reviewed. Hydrothermal stability of zeolites and modelling of permeation through zeolite membranes are some other topics that are covered in this chapter.

4.2. Progress in seeding techniques

Since self-supporting thin zeolite layers cannot be handled, mainly because of mechanical problems, the molecular sieve layer (zeolite, MOF etc.), is usually directly grown on a porous ceramic or metal support. However, zeolite nucleation and subsequent crystal growth on the surface of such supports is difficult to control. A well-established method for the growth of thin and defect-free molecular sieve layers is based on seeding and secondary growth. Seed crystallites of the desired zeolite or MOF are synthesized *ex situ*. In a second step these seed crystallites are brought by different techniques using electrostatic forces (zeta potential differences), covalent chemical anchoring or capillary forces during dip or spin coating to the support surface. Finally, these seed crystallites can grow *in situ* to a homogeneous thin film.

There have been significant developments in the formation of seed layers through the use of techniques such as manual assembly[46] and Langmuir trough deposition.[49] Further, secondary growth of these seed layers has advanced through novel methods such as gel-free growth[40] and minimization of twinning.[12] These and other developments have enabled the formation of sub-1 μm zeolite membranes.[117] Recent reports of 100-200 nm zeolite membranes are promising advances for their commercial viability.[41,44]

4.2.1. Synthesis of zeolite seeds

Traditionally, zeolite seeds have been synthesized by direct (bottom-up) synthesis strategies. For all-silica or high-silica zeolites, this typically involves hydrothermal

treatment of a sol containing silica/alumina source, organic structure directing agent (SDA) and water. SDA-free synthesis of certain zeolites is also possible.[42] There are several reports on shape control of zeolite seeds, i.e. favoring growth along certain crystalline directions and suppressing growth along others.[45,118,119] This is usually done by changing the SDA structure or the growth conditions. There exist several studies on the influence of these conditions on zeolite nucleation and growth, which are summarized in a review article.[33]

The top-down approach for seed synthesis, in which a parent material is first synthesized and then broken down or modified in order to yield seeds, has been considerably advanced. In one approach three-dimensionally ordered mesoporous zeolites are synthesized within carbon templates. They can be disassembled to give spherical nanoparticles precisely sized in the 10-50 nm range, which is not readily accessible by direct synthesis.[120–122] Another approach involves exfoliation of layered zeolites[123,124] and has been discussed recently in a perspective.[125] Although zeolite exfoliation was reported in 1998,[5] only recently MFI and MWW suspensions containing exfoliated nanosheets at sufficient quantity and quality for membrane application were reported.[43] It was further shown that nanosheets could be coated on alumina supports and secondary-grown to form selective membranes. For this approach, it is important to develop methods to remove large, unexfoliated particles which can compromise membrane performance.[44] The exfoliated MFI nanosheets were coated using vacuum filtration to form an 80 nm-thick seed layer, which was secondary grown to give a 200 nm-thick membrane. In a recent work, it was shown that the gel-free secondary growth method

(see **Section 1.3**) can be used in combination with nanosheet seeding to obtain MFI membranes of 100 – 200 nm thickness which are highly selective for xylene and butane isomer separation.[41]

4.2.2. Techniques for seed assembly

4.2.2.1. Manual and self-assembly

Manual and self-assembly of seed monolayers was studied extensively by Yoon and co-workers and it has been reviewed in 2007.[126] According to one version of this technique, zeolite seeds are manually rubbed on a substrate. Either ionic bonding or hydrogen bonding was found to be responsible for the assembly. For example, ionic bonding could be induced between trimethylpropylammonium groups on silicalite-1 and butyrate groups tethered to glass. Hydrogen bonding occurred by direct bonding of hydroxyl group on silicalite-1 crystals and those on glass or mediated by poly(ethyleneimine). A direct covalent bonding between the support and the seed crystals can be established by using water-soluble bi-dentate additives like di-isocyanates as proposed by Yoon.[127] In a first step, the OH groups of the support react with an isocyanate group and in a second step the OH groups of the seed crystals react with the other isocyanate group which results in a strong attachment of the seed crystals to the support. **Figure 4-1** shows the attachment of seeds to an oxidic support surface using the bidentate di-isocyanate as linker.[128] Another way for the attachment of seed crystals is the treatment of the ceramic support with aminopropyl-triethoxy-silane (APTES) before synthesis.[129] The ethoxy groups

react with surface hydroxyl groups of the support resulting in an amino group anchored to the support with a positive zeta potential.

The reversal in charge from a negative to a positive can be also obtained by van der Waals adsorption of positively charged macromolecules.[130]

In subsequent studies, this method has been used to obtain continuous a- and b-oriented MFI films by manually assembling the seeds followed by secondary growth.[46] In a recent work, a 200 nm thick b-oriented MFI membrane on porous silica support was obtained by manual assembly followed by gel-free secondary growth.[40] **Figures 4-2a and 4-2b** show the seed layer generated by manual assembly. **Figures 4-2c and 4-2d** show the final membrane obtained by secondary growth using gel-free secondary growth (see **Section 4.3**).

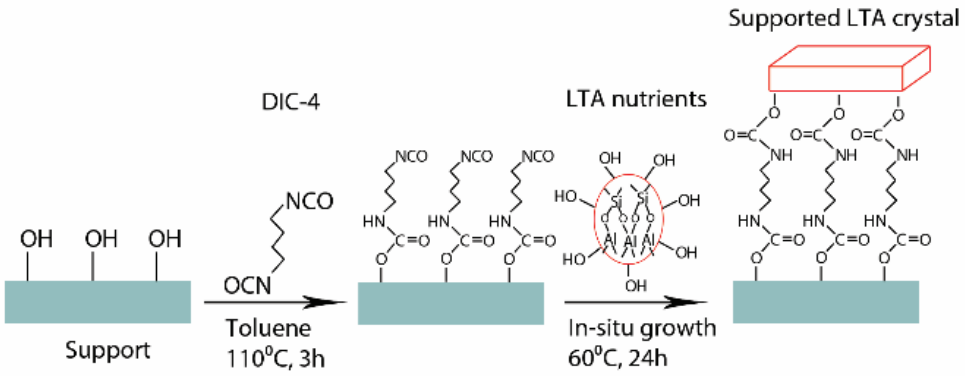

Figure 4-1. Covalent attachment of seed crystals to a ceramic surface by di-isocyanate as bidentate linker between seed crystallite and support.[128]

Other groups have also successfully adapted the Yoon technique in recent years for the synthesis of zeolite films or membranes.[131–137] Recently, Hedlund and co-workers extended the manual assembly technique to nanocrystals by controlling the humidity of

the environment during the coating process.[138] The authors proposed, as shown in **Figure 4-2**, that for hydrophilic substrates like hydroxylpropyl cellulose (HPC), at high relative humidity, assembly is mediated by hydrogen bonding with water molecules from the vapor phase (**Fig. 4-2e**). At lower humidity, the hydroxyl groups on the substrates prefer to bond with each other and nanocrystal assembly is not as strongly favored (**Fig. 4-2g**). For less hydrophilic substrates like poly(methylmethacrylate) (PMMA), high humidity causes the hydroxyl groups to be converted to epoxy groups and nano-crystal assembly is not favoured. Low humidity allows favorable contact between the crystals and the surface (**Figs. 4-2f and 4-2h**).

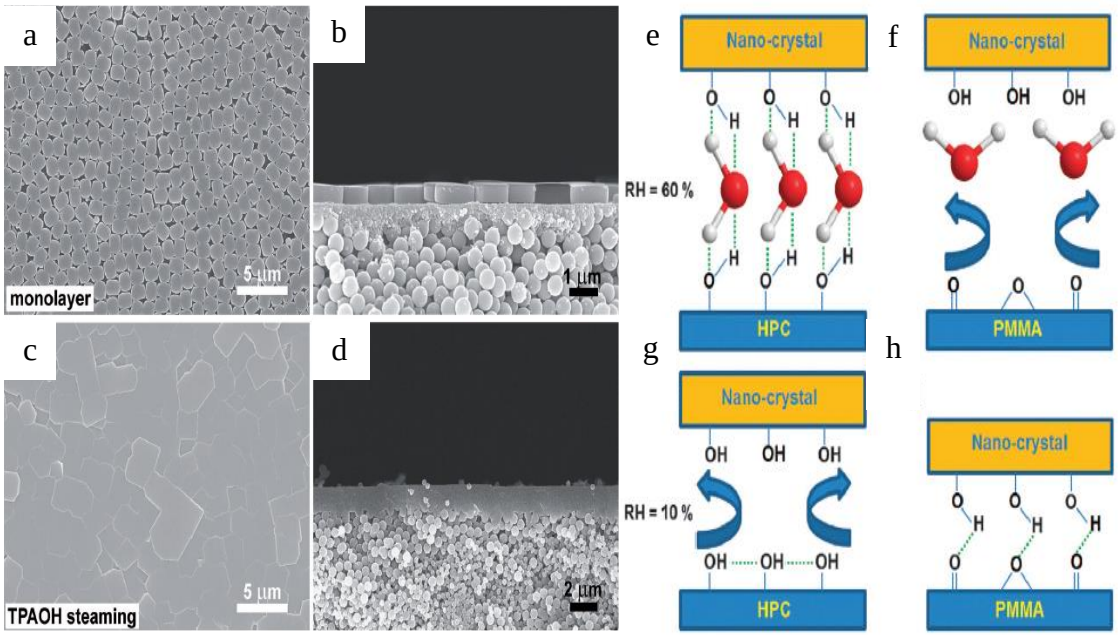

Figure 4-2. (a) Top-view of rubbed MFI seeds on silica fiber support, (b) Cross-sectional view of the same seed layer, (c) Top-view of MFI membrane after gel-free secondary growth, (d) Cross-sectional view of the same membrane (from ref. [40]) (e), (f), (g), (h) Influence of humidity on nano-crystal assembly on two different substrates (HPC and PMMA). (e), (f) Assembly at 60% relative humidity; (g), (h) assembly at 10% relative humidity (from ref. [138]).

Manual assembly has been adapted as a facile seeding technique for lab-scale efforts. An important point to note regarding rubbing by hand is that gloves must be used due to safety considerations. Although manual assembly is not currently scalable for large area membrane fabrication, it could be scaled up by automation of the rubbing process. Rubbing by a rotating or lateral polishing device could be envisioned for large scale application of this technique. Moreover, sonication assisted deposition could also offer a route towards scalable implementation.[139]

4.2.2.2. Langmuir trough assembly

Langmuir trough deposition has been typically used in the past to obtain monolayers of surfactant molecules and other non-zeolitic materials.[65–67,73] A recent review summarizes the current state of the art of this technique.[140] Its use to obtain coatings of zeolites is a more recent development. Following an initial report in 2002, in which a commercial micron-sized zeolite was deposited from the air-water interface onto a silicon wafer,[68] there have been several attempts to obtain thin films of zeolite particles on substrates. In 2007, it was shown that 500 nm thick intergrown films of silicalite-1 could be obtained on silicon wafers by deposition of 95 nm seeds followed by secondary growth.[70] In the same year, monolayer films of zeolite beta of two different sizes (1 μm and 180 nm) were also obtained on silicon wafers.[69] The following year, 100 nm silicalite-1 seeds were deposited as monolayers using the Langmuir-Blodgett (LB) technique.[71] Deposition was followed by secondary growth, resulting in a ~100 nm thick intergrown zeolite film. Recently, LB was used to obtain a 1.5 μm intergrown film,[141]

while an attempt was made to extend the approach to porous supports[50] with the goal of obtaining zeolite membranes.

Moreover, the Langmuir-Blodgett and Langmuir-Schaefer techniques were used to deposit 3 nm thick MFI nanosheet seeds (previously discussed) on silicon wafers.[49] This advancement allowed the formation of an ultrathin seed layer which can be subjected to secondary growth to obtain a continuous film. The final film thickness is sub-12 nm, which is the thinnest intergrown MFI film reported.

Although intergrowth of seed layers prepared by the Langmuir-Blodgett deposition method has been demonstrated, there is no evidence for macroscopic continuity. From our experience, using LB to form coatings with uniform packing over hundreds of micrometers reproducibly can be challenging. Therefore, although continuous LB deposition can be realized we remain sceptical regarding the potential of this approach for large scale zeolite membrane manufacturing. The approach appears better suited to metal organic framework (MOF) films and membranes made by stepwise deposition of reactants, liquid phase epitaxy and other layer-by-layer assembly approaches.[72,142–148]

4.2.2.3. Varying temperature hot dip coating

In the recent literature, there are reports of practical significance with respect to scalable production of zeolite membranes based on a varying temperature hot dip-coating (VTHDC) method,[149,150] which is capable of making seed layers while also plugging defects on the support. In this technique, a tubular support (for example, alumina) is inserted into a solution containing large zeolite seeds at high temperature (177ºC). After

removal of the superfluous crystals by rubbing, the support is dipped into a suspension containing smaller seeds at a lower temperature (77ºC) and withdrawn. This seeding method is reported to allow for reproducible membrane manufacturing of relatively thick films on coarse supports.

4.3. Secondary growth developments

After seeding of the support, a hydrothermal growth step is usually required in order to induce secondary growth of zeolite seeds and close gaps, which are detrimental to membrane performance. Synthesis of a selective membrane without the use of secondary growth has so far not been achieved for zeolites but it has been achieved in other materials, including graphene oxide[151] and MOFs.[152] Development of large aspect ratio nanosheets may enable selective seed layers even in the case of zeolites, by enabling good overlap of nanosheets and minimizing gaps. However, up to now, secondary growth remains a necessary, albeit undesirable step from the large scale production standpoint.

A very important development in secondary growth of zeolite membranes was achieved by Pham et al. recently.[40] They reported a gel-free method of secondary growth which uses a small quantity of structure directing agent but circumvents the use of a gel for growth. Instead, the silica source for secondary growth comes from the support. A precursor version of such a process was published by Chaikittisilp et al.,[48] who showed that the amorphous silica layer on a silicon wafer could be transformed into MFI by steaming in the presence of TPA^+. In the technique of Pham et al., a silica support, coated with a layer of 50 nm silica particles was seeded with b-oriented MFI crystals using the method of rubbing.[46,104] The support was then impregnated with a solution of

tetrapropylammonium hydroxide (TPAOH) and tetraethylammonium hydroxide (TEAOH), which can act as structure directing agents for MFI. The SDA-laden support was then sealed in an autoclave and placed in a convection oven at 190ºC. After heating for several hours, the supported membrane was removed, dried, calcined and subjected to permeation testing. As shown in **Figure 4-3**, the silica source for the growth of the zeolite seeds to form a continuous film is provided by the underlying silica nanoparticles. As the authors mention, this method is simple, saves chemicals and most importantly, preserves the orientation and can be scaled up. It is important to note that this method has so far been demonstrated only for silica supports and all-silica zeolite MFI. It should be possible though to extend it to aluminosilicate zeolites, including zeolite A, by use of the appropriate underlayer and support.

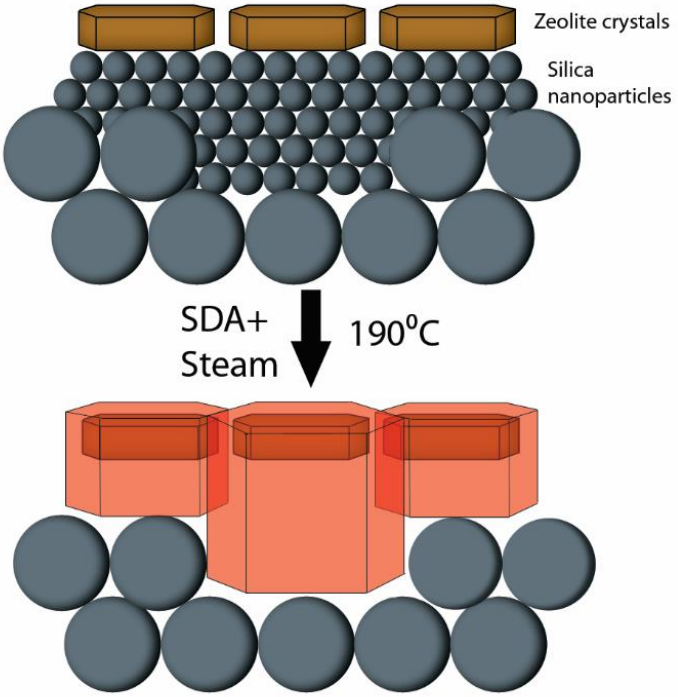

Figure 4-3. Schematic of gel-free secondary growth mechanism (adapted from ref. [40])

4.3.1. Conventional secondary growth and efforts to avoid twinning

Li et al. discovered that accurate control of SDA concentration during solution-based secondary growth promotes in-plane growth of MFI crystals and prevents twinning.[153] b-oriented MFI seed layers were first prepared using manual assembly. For secondary growth solutions of composition 1TEOS: xTPAOH: 165H_2O, 0<x<0.005 was found to result in c-axis elongated crystals which did not fully intergrow, whereas x>0.1 resulted in a large number of a-oriented twins. At intermediate TPAOH concentration, mostly b-oriented intergrown films of about 400 nm thickness were obtained.

A similar approach to secondary growth was extended to the synthesis of MFI membranes on porous alumina supports.[12] It was proposed that twin crystals could be responsible for membrane defects. Thus the TPA^+/Si ratio was optimized to 0.05 for preventing formation of twin crystals. This resulted in an EtOH/water selective membrane.

Other developments are the use of microwave heating for aging of growth solution and for secondary growth.[154,155] It is hypothesized that the rapid heating rate by microwave causes a nucleation bottleneck, allowing a compact film to form within 60 minutes without twin formation. For conventional heating, nucleation occurs around 60 minutes, whereas, it requires around 180 minutes or more for formation of a compact film. This leads to twin formation.

Although numerous reports exist on twin suppression in TPA-based MFI film growth, fundamental understanding is lacking. Also, reproducibility and robustness have not been proven. Secondary growth depends on several factors, including the solution composition, temperature and aging time. Also, the growth procedure has been found to vary based on the type of seed used. For example, the gel-based growth method first reported by Pham et al[46] was used for secondary growth of MFI nanosheet seed layers made by Langmuir trough deposition.[49] However, nanosheets do not grow in the same way as that reported for large bulk MFI crystals. Growth does not uniformly occur with nanosheets, leading to some of the nanosheets growing very fast and others growing very slowly or not at all. This results in a discontinuous film. The same approach when applied to large MFI seeds gives nicely oriented and intergrown films. However, Shete et al recently reported that use of the SDA tetraethylammonium ions (TEA^+) in dilute clear solutions, led to mainly in-plane secondary growth of MFI nanosheets.[47] The disadvantage here is that secondary growth with such dilute solutions is very slow and difficult to use for a practical membrane application.

The recent work by Lupulescu et al.[156] indicates that growth of silicalite-1 takes place according to a combination of both classical and non-classical mechanisms. Classical growth mechanisms suggest that growth takes place by the addition of atoms and molecules, as opposed to non-classical mechanisms which hypothesize that growth occurs through attachment of nanoparticles or aggregates.[157] By in-situ AFM imaging, Lupulescu et al. have conclusively shown that initially the increase in height of a silicalite-1 crystal perpendicular to the <010> face happens linearly, in accordance with

the addition of molecules. However, after a certain time has elapsed, there is a step-change in the height, which corresponds to nanoparticle attachment. This work may help settle the debate regarding silicalite-1 growth mechanisms and identify conditions for twin-free MFI growth and could be extended towards elucidating the growth mechanisms of other classes of hydrothermally grown zeolites.

4.3.2. Secondary growth at neutral pH

During membrane synthesis using alumina supports, use of alkaline environment generally causes leaching of Al^{3+} ions and may lead to membrane deactivation. To circumvent this, there have been several reports of using HF to obtain a neutral pH during secondary growth.[136,158] However, use of HF is undesirable due to the hazards associated with it. Very recently, Peng et al. overcame this by using TPABr as SDA and fumed silica as silica source for secondary growth.[159] The growth is carried out after rubbing MFI seed crystals on glass substrates. The use of glass is crucial because dissolution of Na_2O from glass creates a local mild alkaline environment, allowing growth to proceed. Also, use of TPABr is beneficial as it is inexpensive compared to the conventionally used TPAOH.

4.3.3. SDA-free secondary growth

In order to further minimize the use of SDA, several groups have explored the possibility of a seed-assisted synthesis procedure. Some recent reviews summarize the progress towards synthesis of zeolites by such a procedure.[160–163] Here, seeds are first synthesized

using SDA and further used for zeolite growth from a sol that is devoid of SDA. There are significant advantages to using an SDA-free synthesis procedure. For large-scale zeolite production, there will be some environmental and economic benefits from eliminating the use of organic SDAs. Most importantly, an SDA-free synthesis approach when applied to membranes will circumvent the final calcination step, which is prone to crack formation due to zeolite shrinkage upon SDA removal. Previously, Xie et al. and other research groups have reported the template-free synthesis of beta-zeolite.[164–168] This procedure has been extended to other zeolites, including levyne, EMT and ZSM-5.[169–174]

For membrane applications, this technique has been used to obtain zeolite films on porous supports. Tang et al. synthesized MFI membranes on α-alumina supports without using SDA.[175] A H_2/SF_6 separation factor of 1700 and H_2 permeance of $3x10^{-7}$ $molm^{-2}s^{-1}Pa^{-1}$ at room temperature was obtained. Wang et al. synthesized ~6 μm thick ZSM-5 membranes on porous α-Al_2O_3 supports coated with a YSZ barrier layer (to prevent leaching of aluminum).[176] Zhu et al. synthesized template-free ZSM-5 membranes which showed high water perm-selectivity.[177] A H_2O/IPA separation factor of 3100 was obtained during pervaporation of a 10wt.% H_2O/IPA mixture at 70ºC. Recently, this technique was used to obtain supported growth of zeolite beta.[178] Seed-induced hydrothermal synthesis resulted in 3 μm thick *h0l* oriented beta membranes on α-Al_2O_3 supports. Pervaporation of a 10wt.% TIPB-ethanol mixture at 30ºC resulted in a total flux of 1.58 $kgm^{-2}h^{-1}$ and an ethanol-TIPB separation factor of 320.

4.4. Sub-1μm membrane synthesis

High capital investment and thus long payback times for zeolite membrane separation processes have prevented their large scale implementation. Tsapatsis estimates that one way to reduce the membrane cost to economically viable levels could be by reducing the zeolite membrane thickness to ~50 nm.[35] However, ultrathin membranes, i.e., sub-1 μm thickness of the selective layer, has been an elusive goal for some time in the zeolite community.

As mentioned earlier, Agrawal et al. recently obtained 100-200 nm-thick MFI membranes by gel-free secondary growth of 80 nm-thick seed layers consisting of nanosheets (**Figure 4-4a, b**).[41] For 10 membranes made by this method, the permeance for p-xylene varied between 1.7-3.6x10^{-7} molm^{-2}s^{-1}Pa^{-1} with a maximum p-xylene/o-xylene separation factor of 185 at 150ºC. These membranes were also efficient at separating n-butane and i-butane, achieving a separation factor of 60 at room temperature with an n-butane permeance of 4.3x10^{-7} molm^{-2}s^{-1}Pa^{-1}. At higher temperatures (150ºC), the permeance of n-butane went as high as ~13x10^{-7} molm^{-2}s^{-1}Pa^{-1} but the separation factor dropped to 15. The permeances are consistent with the previous report on 200 nm-thick MFI membranes made from nanosheet seeds, but grown using conventional solution-based growth.[44] However, the earlier separation factor of 25-45 for p-xylene/o-xylene is greatly improved (to >100) by use of gel-free secondary growth. Other efforts for ultrathin MFI membranes are discussed below.

Recent developments by Sjöberg et al. have led to the synthesis of sub-micron MFI zeolite membranes. A 0.7 μm think MFI membrane was used to separate CO_2 from the

synthesis gas (or syngas) derived from black liquor, a byproduct of the paper processing industry.[179] Typically, syngas from black liquor has high CO_2 and H_2S and must be "sweetened" by removal of these gases. The authors synthesized MFI membranes by first masking the α-Al_2O_3 flat supports. The masking process results in impregnation of the support with wax and prevents invasion of the synthesis solution into the support pores and subsequent leaching.[24] The masked supports were seeded and intergrown to form a 0.7 μm MFI film. The use of such thin films results in very high CO_2 permeance of 11.0 x 10^{-7} $molm^{-2}s^{-1}Pa^{-1}$ at 2.25 MPa feed pressure and 0.3 MPa permeate pressure at room temperature. However, the CO_2 permeance reduces to almost half this value after 10 hours of testing, due to competitive adsorption of H_2S. This also causes the CO_2/H_2 separation factor to decrease from 10.4 to 5.0. Thus these membranes are only suitable for feed with small quantities of H_2S.

In another recent work,[117] a similar method to the one described above was used for synthesis of 0.5 μm thick MFI membranes for separation of alcohol and water by pervaporation (**Figure 4-4c, d**). The fluxes obtained for separation of 3wt.% n-butanol/water and 10wt.% ethanol/water mixtures were the highest reported in the literature. However, the alcohol/water separation factors were low (4-5) at 30ºC. This was attributed to the support favoring the transport of water due to Knudsen diffusion. The separation factor for the membrane alone was calculated to be almost 50% higher. The authors conclude that to improve both flux and selectivity, the support resistance needs to be reduced – a general challenge for achieving high flux membranes from thin zeolite films.

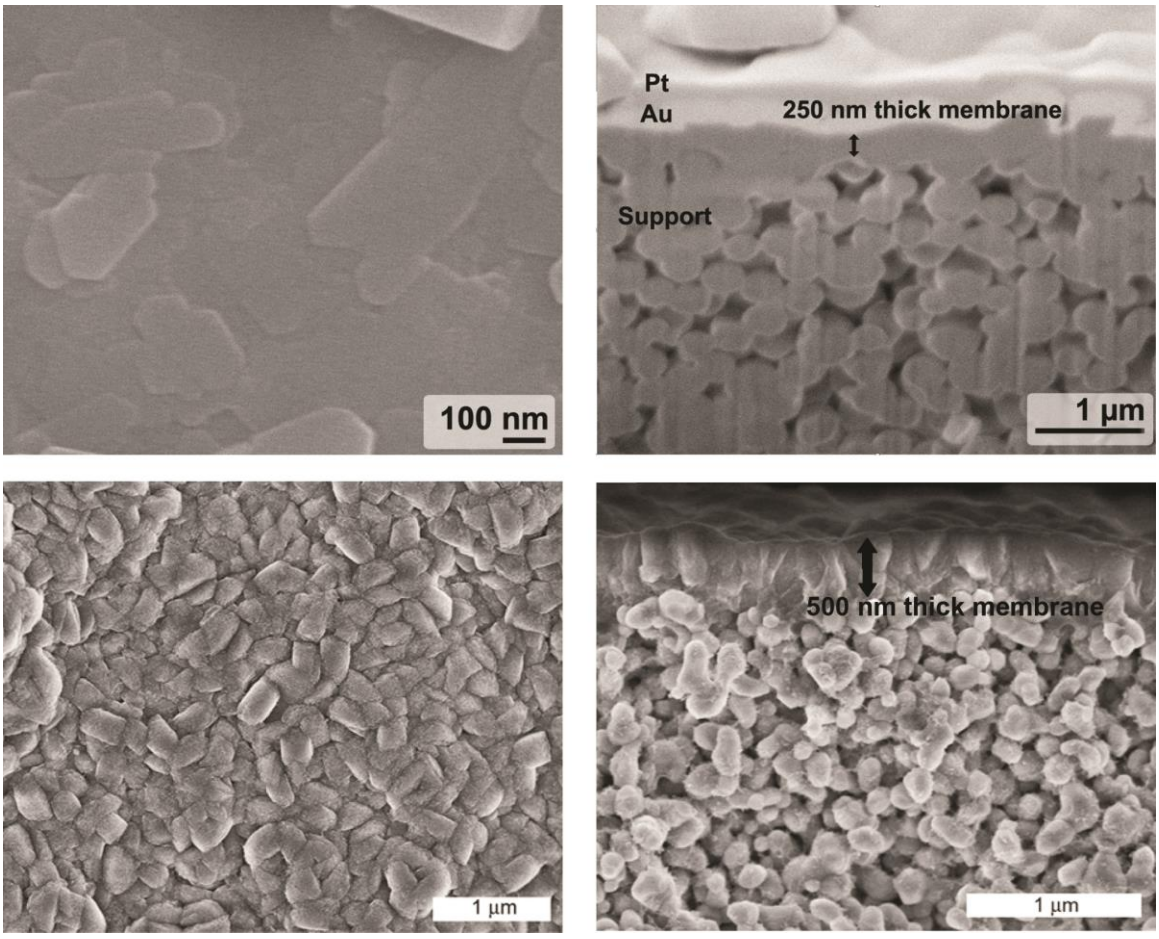

Figure 4-4 (a): Top view SEM image of 250 nm MFI membrane made by gelless secondary growth, (b): cross-sectional SEM image of membrane shown in (a). (c): Top view SEM image of 0.5 mm MFI membrane made by the masking method followed by secondary growth, (d): cross-sectional SEM image of membrane shown in (c). (a), (b) reprinted from ref. [41] with permission from Wiley-VCH. (c), (d) reprinted from D. Korelskiy, T. Leppäjärvi, H. Zhou, M. Grahn, J. Tanskanen, J. Hedlund, *J. Membr. Sci* 2013, *427*, 381. (ref. [117]). Copyright 2013, with permission from Elsevier.

The same group also investigated the separation of n-butanol and water in vapor phase by using a hydrophobic MFI membrane.[180] The supports were first seeded (without

masking) and intergrown using a synthesis solution containing TPAOH and HF. The final membrane thickness was found to be 0.5 μm. Permporometry experiments using n-hexane indicated that the defects in this membrane were almost half that of the membrane synthesized using conventional synthesis sol. For separation of 50/50 mol% n-butanol/water, the hydrophobic MFI membrane had an n-butanol permeance of 7 x 10^{-7} $molm^{-2}s^{-1}Pa^{-1}$, which was half that of the conventional MFI membrane at 160ºC. However, the separation factor (8.3) of the former was twice that of the latter. The lower permeance and higher separation factor of these membranes was attributed to higher hydrophobicity and lower defect density.

The use of hydrophobic MFI membranes was further extended to CO_2/H_2 and CO_2/CO separations.[136] In this case as well, a 0.5 μm membrane was obtained which was confirmed to be b-oriented by x-ray diffraction. The orientation as well as the use of HF for synthesis served to reduce defects even further to 0.13% of membrane area. A CO_2/H_2 separation factor of 100 was obtained at -35ºC and it decreased with increasing temperature. CO_2/CO separation factor was 20 at -15ºC. The CO_2 permeances remained very high, in the range of 50-60 x 10^{-7} $molm^{-2}s^{-1}Pa^{-1}$.

As selective zeolite films become very thin, a number of challenges emerge. Transport may be dominated by pore entry resistance rather than intracrystalline transport and this may alter the transport behavior compared to that of thicker membranes. Also, the development of supports that offer low resistance to permeation is required.

4.5. Polymer-supported membranes

Since the overall cost of membranes is determined in large part by the support cost, it is desirable to develop inexpensive polymeric supports. This would overcome the current limitations of ceramic membranes, including their high failure rate and cost of manufacture. In addition to being less expensive per unit area, membranes supported on polymeric hollow fibers would also be able to pack better, giving higher membrane area per unit volume.[181]

Mixed matrix membranes combining polymers with zeolites have long been studied extensively aiming at low-cost, high-performance membranes.[182–190] However, the inherent incompatibility between zeolites and polymers still remains a limitation, while performance of these membranes has remained low to modest at best.

MOFs, generally, appear to have better compatibility with polymers in mixed matrix membranes compared to zeolites.[191–193] However, performance gains have been similarly modest. Even if compatibility is resolved there are other issues like the flux matching requirement which allow only a small fraction of the zeolite/MOF selectivity to be harvested in a mixed matrix setting.[194] For this reason, deposition of a continuous zeolite deposit on or in a porous support is more desirable.

Following this approach, Wang, Yan and co-workers have fabricated high-flux composite hollow fibers (CHF) consisting of zeolite NaA and polyethersulfone (PES).[195] Two different sizes (4.0 μm and 1.5 μm) of zeolite particles were combined with the polymer solution in different concentrations and extruded through a spinneret. Zeolite membranes were prepared on the external support of the CHFs by a hydrothermal process. It was

found that increasing the loading of zeolite in CHF led to more void spaces and agglomeration of crystals, thus increasing the CHF porosity. The larger zeolite particles led to CHFs with lower porosity. At 85wt.% zeolite loading the difference between the two particle sizes becomes small and dense zeolite coverage is obtained. At this loading, 4-5 hours of growth time gives a high flux membrane for water-ethanol separation. For pervaporation of 90wt.% EtOH-H_2O feed at 70ºC, a flux of >10 $kgm^{-2}h^{-1}$ is obtained with a H_2O/EtOH separation factor of >10000.

These types of membranes were further improved by having the membrane on the inner surface of zeolite/PES-PI hollow fibers.[196] The addition of PI (polyamide) gives added temperature resistance and mechanical strength. Membrane on the inner surface helps to prevent damage to the selective zeolite layer. Similar EtOH/H_2O pervaporation performance was obtained as in the previous report. However, the fibers with higher mechanical and bending strength and with membrane on the inner surface are significant improvements, which could enable commercialization of this technology in the future.

Synthesis of zeolite membranes on flat polymeric supports was also reported recently.[37] Faujasite membrane was synthesized on PES supports supported on a polyester backing. A continuous FAU membrane with a thickness of 500-700 nm was fabricated using just 1 hour of hydrothermal growth on seeded PES supports. The synthesis was further improved so that a 300 nm thick FAU membrane could be obtained on flat PES supports.[38] After elimination of intercrystalline defects by using a PDMS coating (see **Section 4.6**), CO_2/N_2 selectivities of ~72 could be obtained.

4.6. Post-synthesis modification

There are several reports on post-synthesis techniques for improving membrane performance. It has been shown early on that post-synthetic coking of MFI membranes by impregnating and then pyrolyzing TIPB, can be used to plug macro voids and defects between zeolite crystals.[197] This causes a remarkable increase in the n-butane/i-butane selectivity but causes reduction in permeance. In some cases, membranes have been subjected to a UV or thermal treatment, to either cause cross-linking of the polymer matrix in composite membranes or to seal defects in the zeolite layer.[198,199] In other cases, membranes have been post-synthetically treated with chemicals such as oxalic acid, which causes the membrane selectivity to increase.[200]

CVD modification is another widely used post-modification technique. Nomura et al. applied the counter diffusion CVD technique in which TEOS and ozone cause amorphous silica to deposit on the membrane.[201,202] This plugs the intercrystalline defects without completely plugging the zeolite pores as TEOS is too large to enter them. A similar TEOS/O_3 system was used recently for plugging of defects in porous silica membranes of pore size ~1 nm.[203]

Lin and co-workers have used the CVD technique for post-synthesis modification of MFI and DDR-type membranes.[176,204–206] For small non-adsorbing molecules like H_2 and CO_2, the transport is governed by Knudsen diffusion. Thus, plugging of large intercrystalline defects by CVD using a molecule like methyldiethoxysilane (MDES) or TEOS increases the H_2/CO_2 separation factor. However, this is true only for membranes with good initial quality, i.e. those lacking large intercrystalline voids.

Apart from CVD, catalytic cracking deposition (CCD) of MDES was also used in order to reduce the pore size of MFI and effect better separation of H_2 and CO_2.[176] CCD causes deposition in the pores of zeolite and thus reduces H_2 permeance of a ZSM-5 membrane by an order of magnitude (from $2.2x10^{-7}$ to $0.6x10^{-7}$ $molm^{-2}s^{-1}Pa^{-1}$at 450ºC). However, the H_2/CO_2 separation factor increases from about 5 to 19.1. Tang et al. improved on this work by obtaining H_2/CO_2 separation factor larger than 100 at 450ºC and 1.5 bar feed pressure.[207] CCD of MDES only causes a slight decrease in the H2 permeance (from $3.75x10^{-7}$ to $2.2x10^{-7}$ $molm^{-2}s^{-1}Pa^{-1}$).

However, the limitations of CVD and CCD post-treatment are the expensive equipment and difficulty in scaling up. Moreover, amorphous silica deposits are known to undergo densification upon prolonged heating especially in the presence of water vapor.[208] Therefore, the long term stability of these membranes is uncertain.

An alternative approach is the use of a permeable polymer like polydimethyl siloxane (PDMS) to seal membrane defects.[209] CO_2/N_2 separation factors of >1000 at 130ºC are reported after application of a 150 nm PDMS top layer to silica and zeolite Y membranes. The only limitation of using PDMS is that the temperature has to be limited to 250ºC. Fluoropolymers or other temperature resistant polymers may be able to overcome this limitation, provided that they can be made sufficiently permeable.

A post-synthesis modification that improves the hydrophobic properties of the membranes is using silylation. It is known that treatment of zeolites or silica surfaces with triethoxyfluorosilane (TEFS) converts surface silanol groups to Si-F groups, thus increasing the hydrophobicity.[210,211] Use of TEFS is advantageous over carbon-based

silanes due to decomposition of the latter leading to re-formation of silanol groups on calcination.[212] Recently, Kosinov et al. showed that treatment of high silica MFI and MEL membranes (Si/Al ~ 100) improves the ethanol/water separation performance.[213] The best performing membrane had an EtOH/water separation factor of 34 and a flux of 1 $kgm^{-2}h^{-1}$ after treatment with TEFS twice. There is only a marginal reduction of flux (1.5 $kgm^{-2}h^{-1}$ initially) indicating that TEFS mainly modifies the membrane surface and retains the porosity.

4.7. Modeling permeation through zeolite membranes

The Maxwell-Stefan approach provides a fundamental description of multi-component diffusion. Krishna and co-workers have extended this approach to formulate the generalized Maxwell-Stefan model for surface diffusion of adsorbed species in a zeolite membrane.[214–219] Permeation through a zeolite membrane is a combined effect of adsorption and diffusion characteristics. The influence of adsorption is taken into account through the fractional loading at the surface and the thermodynamic factors while the mobility is determined by the two kinds of diffusion coefficients – the corrected diffusivity which is also known as Maxwell-Stefan diffusivity and the exchange coefficients. One of the advantages of using these equations is that the mixture adsorption and diffusion parameters, for most of the cases, can be obtained using only pure component data.[217]

4.7.1. Adsorption

The pure component adsorption isotherm is most commonly modeled using dual site Langmuir model.[220,221] Other forms of isotherm e.g. Toth, Langmuir-Sip, Langmuir-Freundlich have also been used.[222–224] The mixture isotherm can be predicted, from pure component isotherm, by implementing appropriate mixture rules.[225] However, the use of mixture rules is only moderately successful and a thermodynamically consistent model, known as Ideal Adsorption Solution (IAS) theory[226] is widely used for predicting mixture isotherm from pure component data; **Figure 4-5a** shows that the prediction of IAS theory for mixture of alkanes is in excellent agreement with simulation results.[227] One of the drawbacks of IAS theory is the assumption that the system behaves like an ideal solution and therefore it is inadequate to describe multicomponent adsorption for non-ideal mixtures. The existence of non-idealities in the mixture is either due to

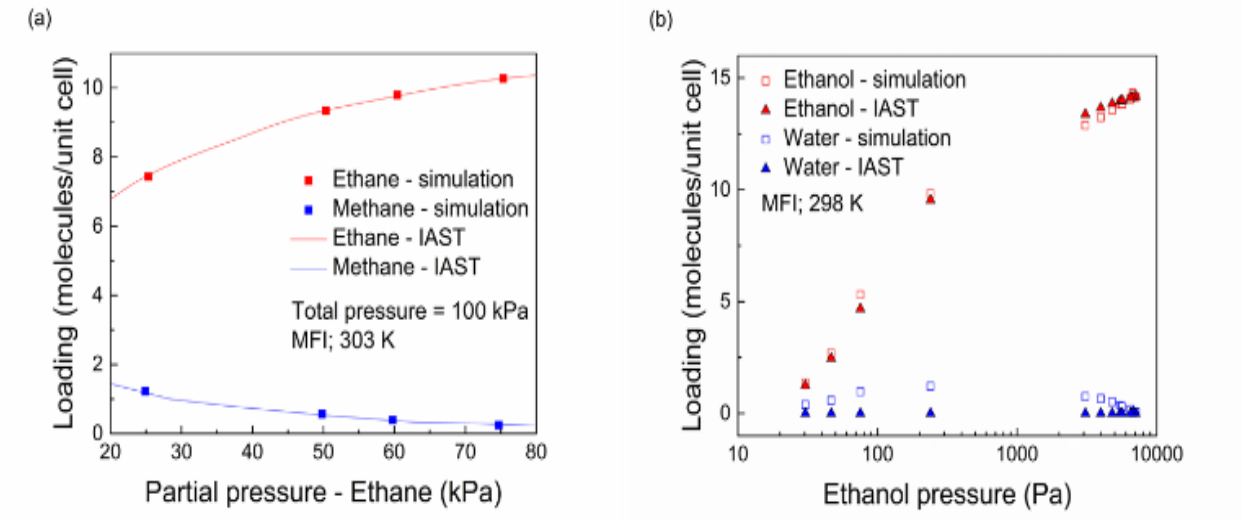

Figure 4-5. Molecular simulation results and IAST prediction for multicomponent adsorption on MFI crystals: (a) success of IAST for methane-ethane mixture (adapted from ref. [227]), (b) failure of IAST for water-ethanol mixture (adapted from ref.[230]).

energetic or surface heterogeneity or due to a non-ideal mixture itself. Energetic heterogeneity arises due to varying heat of adsorption for different sites while surface heterogeneity is caused due to different surface area (sites) available for adsorption of different species. Various extensions of IAS theory have been described to account for these non-idealities; heterogeneous IAS theory has been used to account for energetic heterogeneity[228] and surface area corrected IAS (SAC-IAS) theory has been used to account for surface heterogeneity.[229]

The presence of non-idealities in the mixture can also lead to failure of IAS theory as shown in **Figure 4-5b** for water-ethanol mixture in MFI zeolite;[230] non-ideal behavior arises due to hydrogen bonding between the molecules. Such deviations from ideality are captured by using a more general theory than IAS, known as real adsorption solution (RAS) theory.[226] The RAS theory makes use of the activity coefficients to account for these deviations; these coefficients are, in general, functions of temperature, composition and spreading pressure but the dependence on spreading pressure is often neglected due to complexities. Thus the activity coefficient models such as UNIQUAC, NRTL and Wilson, which are used to describe vapor-liquid equilibrium are often applied with good accuracy to the mixture adsorption as well.[231–235] The parameters are obtained by fitting the experimental or simulation data.

4.7.2. Diffusion

The corrected diffusion coefficient accounts for sorbate-sorbent interactions and exhibit different kinds of loading dependency. Various models have been used to predict this

loading dependency. The most commonly used are the weak confinement scenario and the strong confinement scenario which are based upon the vacancy factor and the repulsion factor.[236] The vacancy factor accounts for the probability of the adjacent adsorbing site being vacant and decreases with loading while the repulsion factor accounts for inter-molecular repulsion and increases with loading. However, these are the ideal scenarios and the actual dependency varies between the two scenarios (see **Figure 4** in ref. 149). Another model, based upon the quasi-chemical approach of Reed and Ehrlich also accounts for the reduction of energy barrier for diffusion with increased loading and is also widely used.[237,238] Since the corrected diffusivity is interpreted in terms of hopping form one adsorbed site to another, the loading dependence is strongly influenced by adsorption thermodynamics. It has been shown that the corrected diffusivity is inversely proportional to the thermodynamic factor which signifies the change in fractional loading with respect to a change in fugacity and can be calculated from the adsorption isotherm (see **Figure 3-5** in ref. 152).[239–241] The corrected diffusion coefficient of a species in a mixture is usually taken equal to that of the pure component at the same total loading.

The exchange coefficients account for sorbate-sorbate interactions and capture the effect that a faster moving molecule is slowed down in presence of slower moving species and vice-versa.[242] The incorporation of the exchange coefficients in the Maxwell-Stefan equations leads to computational difficulties and thus are often neglected; this scenario is known as the Facile exchange.[216,236] However, these effects have been shown to be significant and various models have been proposed for their incorporation.[243,244] Vignes

correlation for species with similar loading and Sholl correlation for species with variable loading are the two most commonly used models.[236] Since the exchange coefficients capture the sorbate-sorbate interactions, it has also been found that there is a dependence of the exchange coefficients on the corresponding fluid phase diffusivity; the proportionality factor depends upon the degree of confinement and the correlation effect increases with the degree of confinement.[245] The factor is often linearly dependent upon the degree of confinement, however, other expressions such as Darken-type interpolation and Vignes-type interpolation have also been proposed.[245]

4.7.3. Predictions

The Maxwell-Stefan approach using the above discussed models for adsorption and diffusion have proven to be very useful in predicting the separation performance of zeolite membranes and also verified against experimental and molecular simulation results.[246–248] The key to success for the Maxwell-Stefan model is the accurate determination of multi-component adsorption and diffusion characteristics of the permeating species. Though these equations have provided a deep insight into the permeation through zeolite membranes, there are cases for which the Maxwell-Stefan model fails to interpret the experimental results. This is either due to the fact that the assumptions used for predicting multi-component adsorption and diffusion characteristics are not adequate or due to some other factors which are discussed next.

One of the examples where the Maxwell-Stefan model fails to provide quantitative agreement with the experimental results is the xylene isomer separation using MFI zeolite

membrane. The adsorption and diffusion characteristics of p-xylene and o-xylene in MFI crystals have been extensively studied and the adsorption parameters and the diffusion coefficients have been extracted from the experimental results.[249–252] The permeation of xylene isomers was also studied using Maxwell-Stefan equations. Though the permeance of p-xylene has been observed to be of the same magnitude, the Maxwell-Stefan model predicts much higher o-xylene permeance as compared to the experiments (see **Figure 5** in ref. 164). This discrepancy may be attributed to surface resistances in zeolite crystals or to the changes in crystal structure on adsorption of p-xylene.[251,253] It can also be due to the fact that the diffusion coefficient used in the Maxwell-Stefan equations was measured for a flexible zeolite crystal while an intergrown supported membrane is constrained by a support and does not permit flexibility, as in the case of a free crystal. Another phenomenon where the Maxwell-Stefan approach fails is the intersection blocking.[254] It is usually observed when branched or cyclic hydrocarbons are present in the mixture along with linear hydrocarbons in MFI. The branched hydrocarbon preferentially adsorbs at the intersection of MFI membrane which causes blocking of the pore and severely reduces the diffusivity of the normal alkane.[221] In general, the tardy species slows down the fast moving species and the effects are captured by the exchange coefficients but this effect is more severe and can cause the diffusivity of n-alkane to reduce nearly to zero. The effect of intersection blocking for methane in presence of i-butane is shown in **Figure 4-6a**; the reduction in diffusivity is more severe as compared to methane/n-butane mixture which does not have intersection blocking.[254] Similarly,

the Maxwell-Stefan equations fail to interpret the experimental results for permeation of n-hexane/3-methylpentane across a MFI membrane.[255]

In mixtures governed by hydrogen bonding or molecular clustering effects, the adsorption and diffusion coefficients cannot be obtained by using only the pure component data.[256] As already discussed, IAS theory leads to a higher separation factor for water-alcohol separation as the adsorbed alcohol molecules also bring the water molecules into the zeolite due to hydrogen bonding.[230] The corrected diffusion coefficient for such systems also depend upon the mixture composition along with the total loading as shown in **Figure 4-6b**.[224,257]

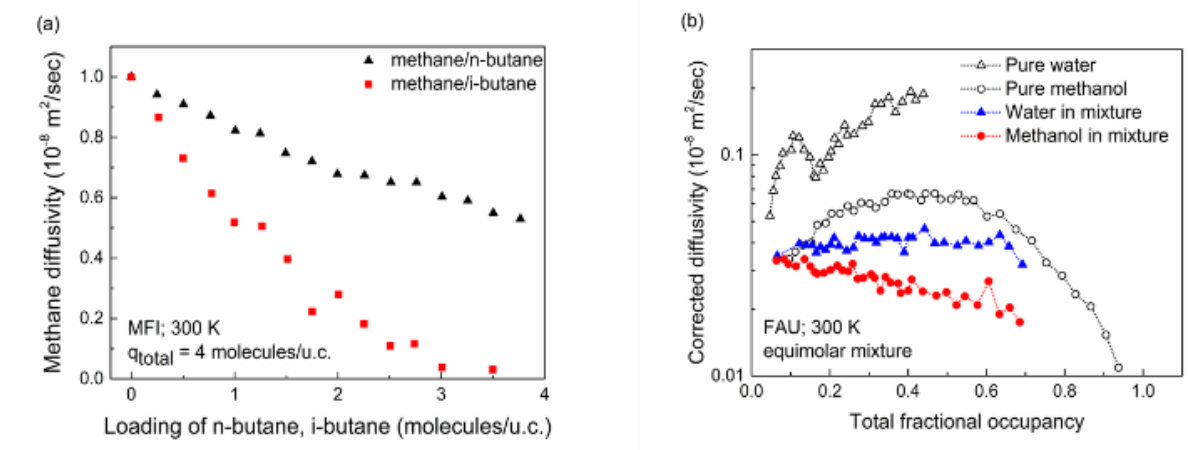

Figure 4-6. (a) Effect of intersection blocking: diffusivity of methane (linear alkane) decreases more steeply in presence of i-butane (branched alkane) as compared to n-butane (linear alkane) in MFI (adapted from ref.[254]), (b) Corrected diffusivity of water-methanol mixture in FAU at 300 K obtained through MD simulations (adapted from ref. [224]).

The correlation effects are also stronger than Vignes interpolation. One peculiar characteristic of such mixtures is the mutual slowing down of both permeating species.[258,259] Thus, using the pure component data to predict the separation performance will lead to higher flux and higher separation factors.[260–262]

4.7.4. Effect of impurities

Another concern for industrial application of zeolite membranes is the presence of impurities. It has been shown that a strongly adsorbed component, even present in small quantity, can suppress the flux of other component and affect the separation performance.[263] Similar degradation in the separation performance of CHA zeolite membranes has been observed when propane is introduced in separation of CO_2/CH_4 and N_2/CH_4 mixtures.[264]

4.7.5. Other factors

Apart from these challenges, some external factors can significantly affect the separation performance of the membranes. These include the effect of porous support, sweep gas and concentration polarization.

The zeolite membranes are usually supported on a porous support. The support layer is usually neglected in most of the modeling studies. However, it has been shown that the support can play a significant role especially for thin or high-flux membranes.[265,266] The significant mass transfer resistance in the support adversely affected the separation performance of MFI and FAU membranes for ethanol/water separation.[117,267] The effect

is more prominent for strongly adsorbing species as shown for H_2/CO_2 separation where the pressure drop for CO_2 over the support was quite large and influenced the separation performance.[268] Thus, flux and selectivity for high flux membranes can be increased by preparing less resistive supports and it is essential to incorporate the effects due to the support layer in the model. The models proposed in the literature are well established and incorporate flux through the Knudsen and bulk diffusion and viscous flow.[220,269,270]

The sweep gas is introduced to drive away the species on the permeate side and thus increase the driving force for permeation. In most of the modeling studies, the effect of sweep gas is incorporated by assuming zero partial pressure of the species on the permeate side. However, it has been shown that the rate of flow of sweep gas can play a significant role.[271] The sweep gas increases the driving force for the permeating species and enhances the separation performance; this effect has been shown for methane/ethane separation.[272] A negative effect on the permeation can occur due to the counter flux of the sweep gas. A higher pressure of helium on the permeate side increases its counter flux and thus decreases the permeance of ethane.[273]

Selective permeation usually shifts the adsorption equilibrium at the membrane surface and thus reduces the separation factor.[274] This effect is known as concentration polarization and is depicted through a schematic in **Figure 4-7a**. Though not many modeling studies of zeolite membranes consider concentration polarization effects, it can play a significant role.[275,276] It has been shown that the CO_2/CH_4 selectivity increased by 180% and CO_2 flux by 80% when measures were taken to reduce the external boundary layer resistance for a SAPO-34 membrane, as shown in **Figure 4-7b**.[276] The effects of

concentration polarization are more prominent for pervaporation as compared to gas permeation since diffusion coefficient is higher for gases. Various models have been proposed in the literature to include its effect by introducing a mass transfer coefficient.[268,277,278] or solving the full concentration profile in the boundary layer.[279,280] The effects can be suppressed by introduction of sweep gas, mixing and making flow turbulent.

Another common assumption in modeling zeolite membranes is that it is defect free. However, it has been illustrated that the defects can significantly affect the separation performance in H_2/CO_2 separation,[268] xylene and butane isomer separation.[281] It has also been shown that defects can be induced and shrink or expand during adsorption and

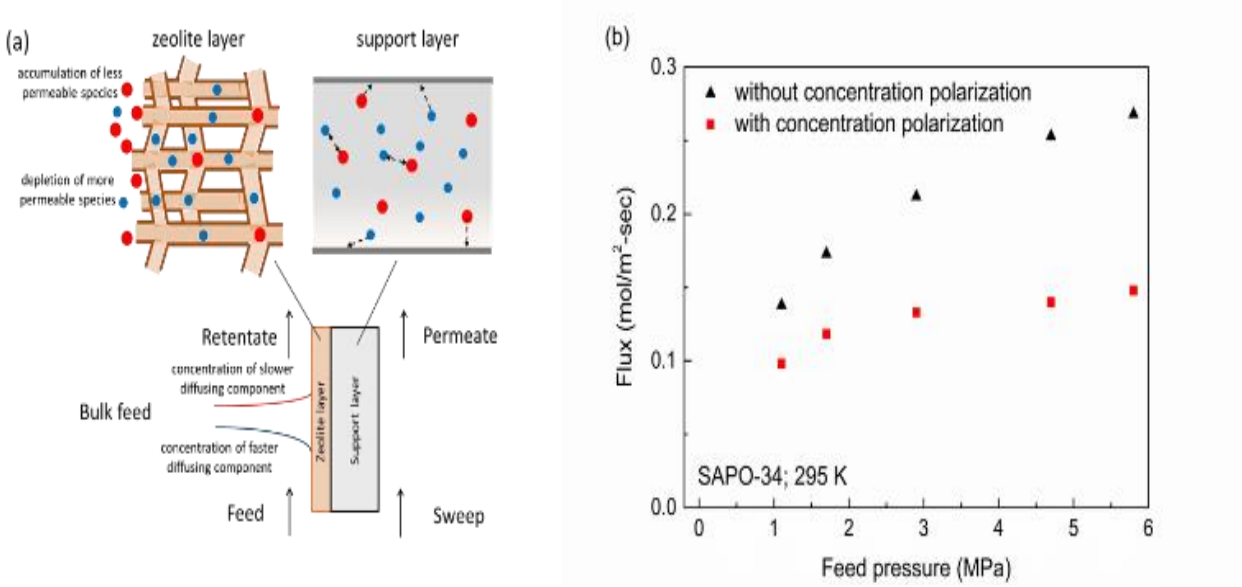

Figure 4-7. (a) Schematic of concentration polarization for permeation through a zeolite membrane, (b) Effect of concentration polarization: CO_2 flux through a SAPO-34 membrane for an equimolar mixture of CO_2/CH_4 at 295 K (adapted from ref. [276]**).**

affect the permeation.[253] Permporometry, flux of molecules larger than zeolite pores, ratio of single gas permeance and other methods have been used to characterize the defects.[282–285] These effects have been incorporated in some of the modeling studies by determining the permeation through the defects as a combination of Knudsen diffusion and Poiseuille flow.[286,287] A general pore network model has also been developed to account for the flux through intercrystalline pores.[288]

4.7.6. High throughput computational screening of zeolite structures

By using this technique, a library of structures consisting of several thousands of structures can be rapidly screened based on desirable attributes. These could include pore size, adsorption properties and gas separation performance. A recent review summarizes the work that has been done so far on high throughput screening of MOF structures.[289] Two important factors for the characterization of porous networks are the largest cavity diameter (LCD) and the pore limiting diameter (PLD). The LCD gives an estimates of whether two molecules of different species can pass each other within the structure. This is useful for separations. If a molecule's size is smaller than the PLD, it can diffuse freely through the network. If not, there is a significant energy energy barrier towards diffusion. Haldoupis et al. characterized >250,000 hypothetical zeolite frameworks based on their PLD and LCD.[290] First et al. characterized the existing zeolite frameworks with respect to the accessible pore volumes, surface areas, PLDs and LCD.[291]

First et al. also screened 196 zeolite frameworks and 1690 MOF frameworks to find candidate structures for gas separations such as CO_2/N_2, CO_2/CH_4, CO_2/H_2 and

hydrocarbons such as propane/propylene and ethane/ethylene.[292,293] The screening was based on the calculation of the shape selectivity of the framework for the gases of interest using a minimum-energy pathway approach.

Martin et al. developed a method for computational screening of zeolite structures for adsorption-based separations such as CO_2/N_2.[294] The Henry coefficient (K_H) and heat of adsorption (H_A) were computed through Monte Carlo simulations for about 140,000 structures. Those with the highest K_H and H_A for CO_2 were screened as possible candidates for CO_2/N_2 separation. This technique of selection was a large improvement (60-70 fold enrichment of possible structures) over the previous random selection or brute-force approaches.

Kim et al. screened the experimentally verified IZA structures and 30,000 hypothetical structures for ethane/ethene separation.[295] They found about 30 potentially high-performing structures for this separation. Other studies have used computational screening to identify possible candidates for CO_2/CH_4, CO_2/N_2 separation,[296] natural gas purification,[297] ethanol purification from fermentation broths and hydroisomerization of alkanes.[7]

4.8. Progress in industrial application of zeolite membranes

The review by Gascon et al. highlights the progress made on synthesis and application of zeolitic membranes and coatings during the last few years[298]. However, so far only one type of zeolite membrane has been commercialized. LTA membranes are used in the dehydration of different solvents because of their strong hydrophilicity and suitable pore size. There is still no gas separation process worldwide in operation using zeolite

membranes. Ambitious aims for the development of an industrial process for xylene isomers[24] and butene isomers[299] separation using MFI membranes could not be realized yet. Despite excellent lab test results and successful scale-up work, the industrial installation of SAPO-34 and DD3R membranes in the CO_2/CH_4 separation could not be realized either. [300–302]

The established technology for the production of dry (bio) ethanol is the pressure swing adsorption (PSA) using 3 A zeolite (K^+ exchanged LTA).[303,304] Polymers are of interest for replacing PSA by a membrane technology, since they have advantages over inorganic membranes such as lower production costs, easy manufacture and scale up.[305] Especially polyimides and polyamide-imides turned out to be promising pervaporation membrane materials because of high separation performance, low swelling and excellent thermal, chemical and mechanical stability[306–308].

A pioneering role in the development of zeolite Na-LTA zeolite membranes for the dehydration of bio-ethanol was played by Bussan Nanotech Research Institute Inc. (BNRI), Japan, a Member of the Mitsui Holding, which developed a process for the production of fuel-grade ethanol by hybrid distillation/vapor permeation process.[309,310] Further milestones in the development of commercial LTA membranes for de-watering of different liquids by pervaporation are the advancements of BNRI,[311] Inocermic GmbH, Germany (ethanol[312]), Smart Chemical Company (t-butanol[313] and tetrahydrofuran[314]), Nanjing Jiusi Hi.Tech Co. (different solvents), and a 100% daughter of Dalian Institute of Chemical Physics working for Jiangsu Xinhua Chemical Co. Ltd. (mainly i-propanol, but also other solvents).[315]

In this review, the Chinese activities will be highlighted since the Nanjing and Dalian teams have so far established over 50 plants for dehydration of industrial solvents from chemical and pharmaceutical industry in China. The separation systems concern methanol, ethanol, isopropanol, acetonitrile, tetrahydrofuran, MTBE, ethylene glycol etc. Recently, the more stable zeolite T (erionite-offretite) membranes[316,317] came into the focus.

A combined seeding method by using ball-milled seeds was developed at Nanjing University of Technology for the synthesis of LTA zeolite membranes, which could improve reproducibility and reduce synthesis time significantly.[318] In 2011, the Jiangsu Nine Heaven High-Tech Co. Ltd. was founded as a spin-off, to promote the commercial application of the LTA membrane dehydration technique. A production line of LTA zeolite membranes with the productivity of 10,000 m^2/year has also been established. The NaA zeolite membranes are prepared on the outer surfaces of home-made 80 cm long mullite supports.

Figure 4-8 shows an industrial apparatus for the dehydration of ethanol (1,500 tons/year) from 93wt.% to 99.5 wt.%.[319] It has 7 membrane modules connected in series with each module having a membrane area of 3 m^2. The apparatus is operated under vapor permeation mode. A significant reduction (over 50%) in the separation cost was achieved for the membrane technique instead of extractive distillation with salt. The lifetime for the membranes used in the system is more than two years. **Figure 4-8** also shows an apparatus for dehydration of acetonitrile (15,000 tons/year) from 80 wt.% to 99 wt.%. The apparatus has 20 membrane modules (10 m^2/each) with total membrane area of 200

m^2. The membrane dehydration technique can save more than 50% steam consumption for production of acetonitrile compared with rectification under vacuum.

Figure 4-8. Apparatus for dehydration of ethanol (1,500 tons/year) left, apparatus for dehydration of acetonitrile (15,000 tons/year) right, above, and membrane modules for dehydration, right below at Jiangsu Nine Heaven High-Tech Co. Ltd.[319]

In 2012, Dalian Institute of Chemical Physics (DICP) installed at Jiangsu Xinhua Chemical Co. Ltd.an LTA zeolite membrane unit for i-propanol dewatering with a capacity of 50,000 tons/year. The separation unit consists of 35 modules with a total permeation area of about 350 m^2 (**Figure 4-9**) which is the largest zeolite membrane facility in the world.[320] This progress of the researchers at DICP is mainly due to the use of microwave heating.[321–325] Microwave heating does not only reduce synthesis time, but it also appears to reduce the formation of non-zeolitic defect pores in comparison with conventional heating.[326]

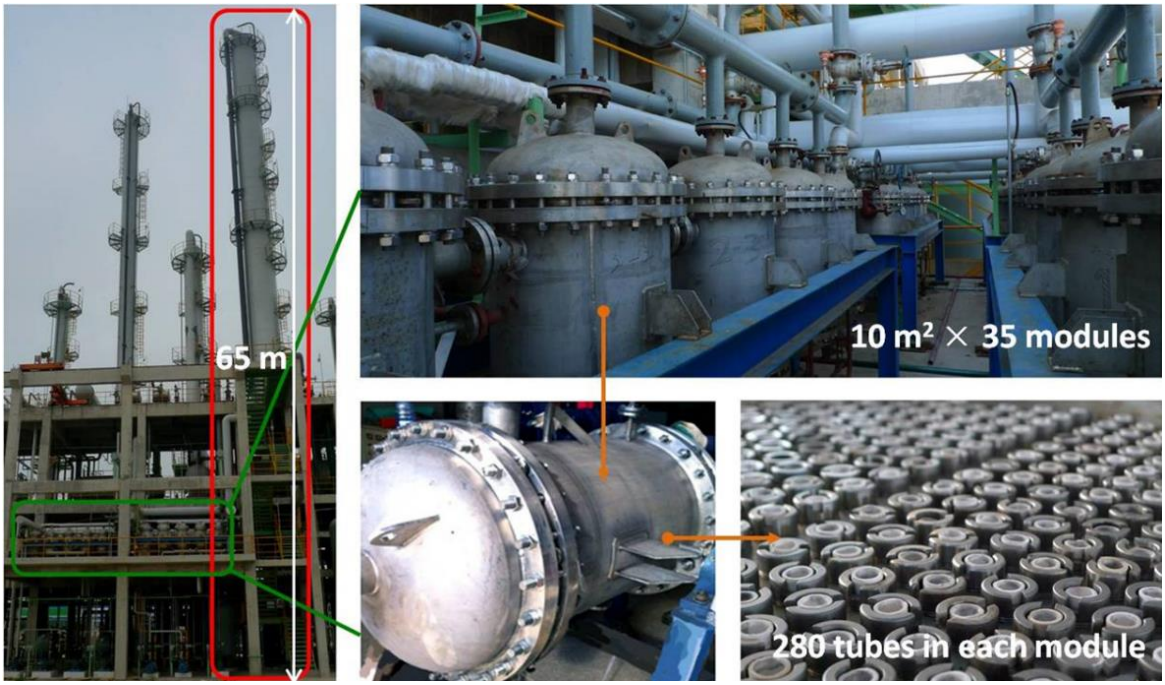

Figure 4-9. DICP plant with LTA zeolite membrane units for a capacity of 50,000 t/year for i-propanol dewatering for Jiangsu Xinhua Chemicals Co. Ltd. The membrane unit (in the green frame) replaces the distillation column (in red frame) achieving a remarkable reduction in energy consumption.[315]

4.9. Zeolite membrane reactors for the intensification of chemical processes

During the last 5 years, a few comprehensive reviews on zeolite membrane reactors appeared.[327,328] Membrane reactors are one of the concepts for intensified chemical processes.[329]. A (catalytic) membrane reactor combines a chemical reaction with an *in situ* separation in one unit.[330–332] Catalytic membrane reactors can be classified according to their function into (i) Extractor-, (ii) Distributor-, and (iii) Contactor-type reactors. The extractor mode especially requires a high separation selectivity, which can be provided by zeolitic molecular sieve membranes. In addition to their molecular sieving function, zeolite membranes are relatively stable at the temperatures of most chemical

reactions and they are stable against solvents in comparison with organic polymer membranes. In the past, there were numerous examples of increase in yield of a dehydrogenation or esterification reaction if the product molecules, hydrogen or water, respectively, could be removed selectively under equilibrium-controlled reaction conditions from the product mixture.[333]

Here, the progress after 2010 is reviewed. There are increasing activities to develop hydrophilic water-selective membranes which are more stable than LTA. Zeolite SOD is hydrophilic like LTA, but with a higher framework density of 17.2T/1000Å^3, it shows a higher chemical and thermal stability compared with zeolite LTA (12.9T/1000Å^3).[334] The small pore size of the 6-ring of H-SOD (2.65 Å) allows molecular sieving, i.e. the selective permeation of small molecules like H_2O with kinetic diameters of 2.6 Å. Therefore, due to their hydrophilicity and molecular sieving properties, SOD membranes can accomplish the removal of steam under harsh reaction conditions[335–337] and could be used in the synthesis of methanol (MeOH, eq.1), dimethylether (DME, eq.2) and dimethylcarbonate (DMC, eq.3) in catalytic membrane reactors with carbon dioxide, hydrogen or methanol as reagents:[338]

$$CO_2 + 3\ H_2 \leftrightarrows CH_3OH + H_2O \qquad (1)$$

$$2\ CO_2 + 6\ H_2 \leftrightarrows CH_3OCH_3 + 3\ H_2O \qquad (2)$$

$$CO_2 + 2\ MeOH \leftrightarrows CH_3OCOOCH_3 + H_2O \qquad (3)$$

The separation performances of SOD membranes for equimolar mixtures of steam with H_2, CO_2, MeOH, DME or DMC, were evaluated in the temperature range from 125 to 200°C. The mixture separation factors for steam from DME and DMC through the SOD

membrane were found to be higher than 200 and 1000, respectively. To increase the hydrothermal stability of SOD membranes, SOD can be doped with sulphur.[339]

MFI membranes modified by catalytic cracking deposition (CCD) have been successfully evaluated in catalytic high-temperature water-gas shift (WGS) reactors.[340] Despite the relatively modest hydrogen selectivities ($\alpha_{H2/CO2} \approx 31$, $\alpha_{H2/CO} \approx 25$), the CO conversion could be increased over the thermodynamic limit. MFI membranes modified by CCD coking have been also successfully evaluated in low-temperature WGS reaction to overcome the equilibrium constraints (**Figure 4-10**).[341] For the applications mentioned above, long term thermal and hydrothermal stability are important and they are addressed next.

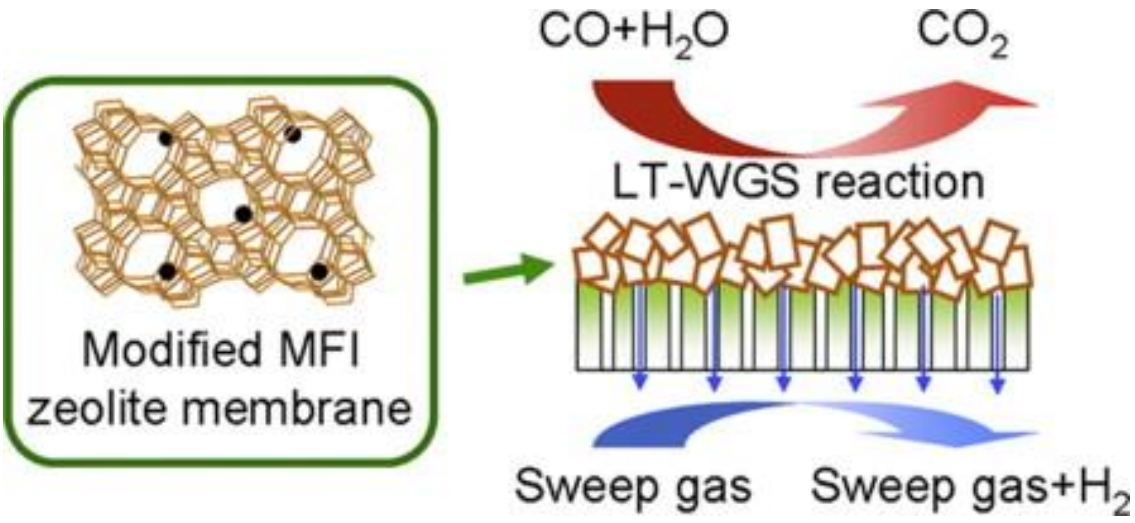

Figure 4-10. Schema of a membrane supported water-gas shift reaction: In an extractor-type membrane reactor, hydrogen is selectively removed through an MFI membrane modified by coking.[341] Reproduced with permission from Elsevier.

4.10. Hydrothermal stability of zeolite membranes

Water vapor at temperatures higher than ~200°C is present in many industrially important reactions (e.g. water gas shift (WGS), steam methane reforming (SMR), methanol synthesis, Fischer-Tropsch (FT)). This makes steam stability of membranes of immense importance for the realization of membranes in chemical industry. Research in this area has primarily been focused on the effect of steam on catalytic activity of zeolites for use in catalysis. In general, steaming can cause dealumination via hydrolysis of Si-O-Al bonds and formation of extra-framework aluminium oxide or hydroxide species.[342] While these studies can provide some insights for the initial screening of zeolites for use in membrane fabrication, the concept of steam stability in membrane science requires different standards. Furthermore, all-silica zeolites, being intrinsically hydrophobic but not very active catalytically, are of particular interest for membrane studies in steam-containing environments. In this context, detailed short- and long-term steaming effect on the structure, morphology, film-support interaction, and grain boundaries need to be addressed. In practice, the effect of steam on membranes rather than powders can serve as a low-cost bullet proof test of membrane applicability for the intended process. In this section, we briefly cover the steam stability of zeolites followed by permeation studies in zeolite membranes involving high temperature steam.

Steaming of zeolite Y has been widely used to form ultrastable Y (USY) catalyst for the petroleum industry. Stability comes from partial dealumination of aluminum framework and incorporation of silica, by migration from other parts, into the generated vacancies.[343]

Kennedy et al.[344,345] and Ma et al.[346] studied the effect of water vapor on MCM-22 at 850ºC for 8 h and 450 and 550ºC for 2 h, respectively. Both found that steaming enhanced the spectral resolution of ^{29}Si solid state MAS NMR, pointing to the reduction of defects in the framework. It has been suggested that a minimum lifetime of 2-3 years is required for membranes to keep up with periodic turnarounds for maintenance in industry.[347]

Recently, the long-term steam stability of MWW framework zeolites (MCM-22 with Si/Al=40 and all-silica ITQ-1) was investigated.[348] MCM-22, ITQ-1, and $SiCl_4$-treated ITQ-1 were steamed (95 mol% H_2O, 5 mol% N_2) at temperatures of 350ºC and 600ºC

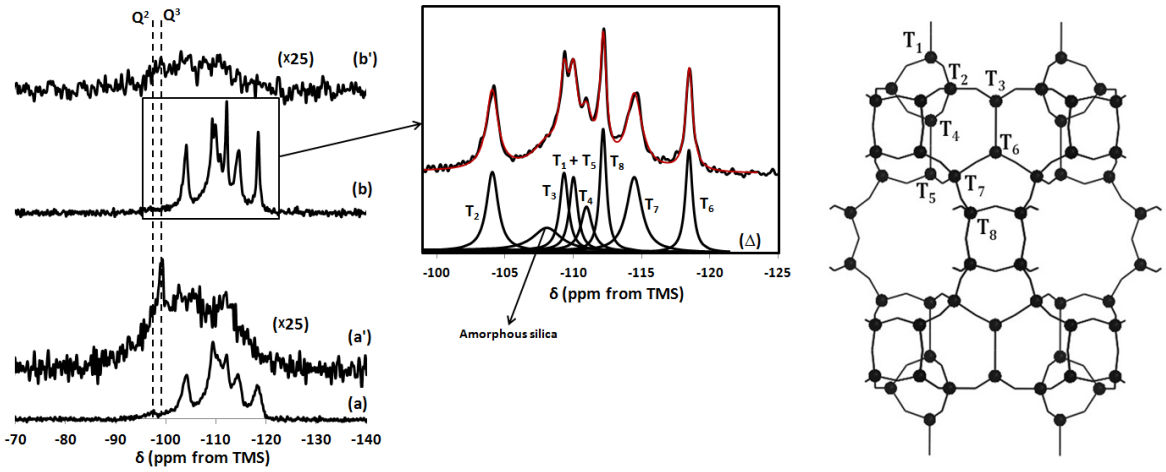

Figure 4-11. 29Si MAS NMR (a, b) and CP/MAS NMR (a′ and b′) spectra of MCM-22 (left): before (bottom) and after (top) 84 days of steaming at 350°C and 10 barg (95% H2O, 5% N2), respectively. (Δ) is the deconvoluted components of the experimental spectrum (b) and the resulting fit is shown in the solid red line. Projection of the MWW unit cell viewed along the b axis with eight crystallographically unequivalent tetrahedral sites is shown on the right side (from ref. [348]**).**

under 10 barg pressure for 84 days. Under high steaming temperature of 600ºC, both zeolites underwent significant morphological changes exhibiting cavity formation in the crystals and significant loss of microporosity. However, at the lower steaming temperature of 350ºC, MCM-22 and $SiCl_4$-treated ITQ-1 retained 70% and 60% of microporosity, respectively. Consistent with the studies of Ma et al. and Kennedy et al., steaming enhanced the short range ordering of the crystals by reducing the structural defects (see **Figure 4-11**). It was also found that defects in the structure can significantly lower the steam stability of zeolites. It was concluded that any efforts for application of zeolite membranes under such steaming conditions require eliminating (or minimizing) the structural defects. This can be achieved by methods such as fluoride synthesis or post-synthesis techniques ($SiCl_4$ treatment).[348]

In the following, some membrane permeation studies under water vapor at high temperatures are highlighted. While some of these reports are not directly aimed at investigating the long-term steam stability of membranes, they can provide valuable insights on the performance of difference zeolite membranes under steam conditions.

Sato et al.[349] investigated the performance of FAU-type zeolite membranes for application in methanol synthesis. It was shown FAU-membranes can separate water and methanol from water-methanol-hydrogen mixtures at temperatures and pressures as high as 180^{o}C and 5 MPa, respectively. The authors attributed membrane selectivity to the preferential adsorption of water and methanol onto the zeolite.

Sawamura et al.[350] investigated the performance of mordenite membrane for water-methanol-hydrogen vapor mixtures in the temperatures range of 150-250^{o}C and pressures

up to 0.7 MPa. The water permeance was $1.8x10^{-8}$ $molm^{-2}s^{-1}Pa^{-1}$ while the separation factors for H_2O/H_2 and H_2O/CH_3OH at 250ºC were 50 and 75, respectively. In the absence of water in the feed, membrane lost its selectivity. The authors speculated that the zeolite water loss, in the absence of water in the feed at temperatures higher than 230ºC, caused the membrane failure by crack formation.

Sadat Rezai et al.[351] investigated the performance of MFI zeolites (silicalite-1 and ZSM-5) membranes in ternary H_2O/H_2/n-hexane (in balance He) vapor mixture in the temperature range of 25-350ºC and at atmospheric pressure. Membranes showed the highest H_2O/H_2 separation factors of 15 and 20 at 25ºC for silicalite-1 and ZSM-5, respectively. However, at temperatures higher than 180ºC the separation factor approached 1. The loss of selectivity was attributed to the reduced water adsorption at higher temperatures. No negative effect of water on the zeolite structure or zeolite membrane integrity was reported in this study.

Masuda et al.[352] proposed catalytic cracking of silanes (CCS) to reduce the effective pore size of MFI zeolite. The idea was to deposit silanes inside the pores (as opposed to outside as a film) for separating small molecules for which MFI zeolite is otherwise not very selective (see **Section 4.6**). Highly hydrogen permselective MFI membranes were made at the cost of one order of magnitude reduction in permeance. Dong's group extensively studied[353] and enhanced this method by developing an on-stream catalytic cracking deposition (CCD) process using methyldiethoxysilane (MDES). The modified MFI membranes were hydrogen permselective (H_2/CO_2 ideal selectivity as high as 19 and H_2 permeance of $1.5x10^{-7}$ $molm^{-2}s^{-1}Pa^{-1}$) in the temperature

range of 400-550ºC. Further, the membranes remained selective, although there was some loss in permeance and selectivity, under water gas shift reaction conditions after 1800 h ((1100 h wet + 700 h dry) of testing, as shown in **Table 4-1**.

Bernal et al.[354] investigated the effect of water vapor on the performance of ZSM-5 and composite mordenite/ZSM-5/chabazite membranes in the temperature range of 30-225ºC at atmospheric pressure. ZSM-5 membrane was stable for ~60 h of testing under about 4 kPa of water vapor.

Lin's group[355] investigated ZSM-5 and silicalite-1 membranes under dry and wet mixture of H_2-CO_2 in the temperature range of 400-550ºC and pressures up to 388 kPa. They showed water can have suppression effect on the permeance of both hydrogen and carbon dioxide at these high temperatures. This effect was attributed to the intrinsic hydrophilicity of ZSM-5 and silanol groups in silicalite-1. The membranes showed a low H_2/CO_2 selectivity of about 3.5, however, no crack formation was reported. Günther et al.[339] reported hydrothermally stable S-SOD (sulfur-doped sodalite) membranes for H_2/CO_2 separation. They indicated that S-SOD is stable at 270ºC and 40 bar in the presence of 30 wt.% water.

It follows from the above, that zeolites are not the thermodynamically most stable product. They can re-crystallize into dense phases or even become amorphous, but the energy barrier of these transformations is relatively high in comparison with MOFs. For MOFs, stability is a major issue. As an example, MOF-5 decomposes at room temperature in atmospheric air by hydrolysis. In some recent reviews by Canivet and Burtch, the limits and promises of the MOF stability towards water are treated.[356,357] In a

previous pioneering paper by Low, a good overview on the steam stability of MOFs as a function of temperature is given.[358] In many studies on steam stability of MOF membranes, the tests have been carried out only for short periods of time (1-2 days) and it is hard to make conclusions on the long-term stability.[359,360]

Table 4-1. Gas permeance ($P_{m,i}$, 10^{-7} $molm^{-2}s^{-1}Pa^{-1}$) and H_2 selectivity for the modified MFI membrane. Reproduced from ref. [353] with permission from ACS.

		Fresh after modification		After operating for 1800 h at >400ºC				
T (ºC)	**Property**	**H_2**	**CO_2**	**H_2**	**CO_2**	**H_2O**	**N_2**	**CO**
400	$P_{m,i}$[a]	1.20	0.08	0.83	0.09	0.31	0.06	0.07
	$\alpha^0_{H2/i}$[0]		14.2		9.23	2.64	12.7	12.6
	$P_{m,i}$[b]	0.85	0.09	0.62	0.08			
	$\alpha_{H2/i}$		9.76		7.47			
450	$P_{m,i}$[a]	1.25	0.08	0.90	0.09	0.33	0.06	0.07
	$\alpha_{H2/i}$[00]		15.6		10.3	2.77	14.2	12.5
	$P_{m,i}$[b]	0.93	0.09	0.64	0.08			
	$\alpha_{H2/i}$		10.9		7.79			
500	$P_{m,i}$[a]	1.33	0.07	1.03	0.09	0.34	0.06	0.07
	$\alpha^0_{H2/i}$		18.1		11.4	2.99	16.1	14.3
	$P_{m,i}$[b]	0.99	0.09	0.65	0.08			
	$\alpha_{H2/i}$		11.1		8.28			
550	$P_{m,i}$[a]	1.45	0.07	1.03	0.08	0.35	0.07	0.07
	$\alpha_{H2/i}$		18.8		12.2	2.95	15.9	14.5
	$P_{m,i}$[b]	1.01	0.09	0.66	0.08			
	$\alpha_{H2/i}$		11.3		8.6			

4.11. Conclusions and outlook

There has been significant progress in the development of supported zeolite membranes. Though there are several industrial processes for dewatering of organic liquids using LTA membranes, there is still no industrial process for gas separation using zeolite membranes. A major impediment is the relatively high costs of these membranes due to the use of graded ceramic supports. Multi-channel monoliths or temperature-stable hollow-fiber polymer supports could be viable substitutes for ceramic supports.

The scale up of supported zeolite and membranes will remain a challenge due to the current discontinuous synthesis processes. Membrane formation by continuous processes (e.g. extrusion, spinning, coating-based) should be the technological focus. Well characterized membrane microstructures (e.g. preferred orientation, designed interfaces, grain boundary control), emphasis on reproducibility and stability of performance under industrially relevant conditions (high temperature, pressure and multicomponent mixtures) should remain the focus of fundamental studies. The next chapter describes progress towards achieving some of these goals.

Chapter 5

Ultra-Thin Zeolite Membranes for Gas Separations: Progress Towards Industrial Applications[‡]

[‡]Portions of this chapter appear in the following:

K. V. Agrawal, B. Topuz, T. C. T. Pham, T. H. Nguyen, N. Sauer, N. Rangnekar, H. Zhang, K. Narasimharao, S. Basahel, L. F. Francis, C. W. Macosko, S. Al-Thabaiti, M. Tsapatsis, K. B. Yoon, *Adv. Mater.* **2015**, *27*, 3243. (Reproduced with permission from John Wiley and Sons).

M. Y. Jeon, D. Kim, P. Kumar, P. S. Lee, N. Rangnekar, P. Bai, M. Shete, B. Elyassi, H. S. Lee, K. Narasimharao, S. N. Basahel, S. Al-thabaiti, W. Xu, H. J. Cho, E. O. Fetisov, R. Thyagarajan, R. F. Dejaco, W. Fan, K. A. Mkhoyan, J. I. Siepmann, M. Tsapatsis, *Nature*, **2017**, 543, 690-694. (Reproduced with permission from the Nature Publishing Group).

5.1. Chapter overview

In this chapter, the recent results on high performance zeolite membranes are described. Ultra-thin MFI membranes were synthesized from nanosheet seeds using gel-free secondary growth. Previously, these membranes have shown good performance for separation of xylene isomers. However, they had not been applied for separation of xylene isomers at industrially relevant conditions. Here, we show that by increasing the support strength and using an appropriate sealing technique, high temperature and high pressure xylene isomer separation data can be obtained. For the first time, high flux and separation factor is obtained under these conditions, which is promising for potential industrial applications. High performance for separation of butane isomers was also demonstrated by these membranes. Finally, xylene isomer separation performance of

membranes synthesized from bottom-up dC5 MFI nanosheets is presented. Such nanosheets can enable scalable production of ultra-thin zeolite membranes.

5.2. Introduction

Zeolite membranes is an area of research that has been consistently growing for the past decade. A search for the terms “zeolite+membrane” in the Web of Science database yielded over 4,500 results over the past 20 years. The past five years have seen a very large output of academic research in this area, with more than 300 articles published each year (see **Figure 5-1**).

Even though there has been considerable academic work in this field, the industrial applications of zeolite membranes are few, as discussed in Chapter 4. The large-scale applications consist of LTA zeolite membranes for dewatering of organic liquids like ethanol and isopropanol.[326] No industrial application exists for gas separation using zeolite membranes.

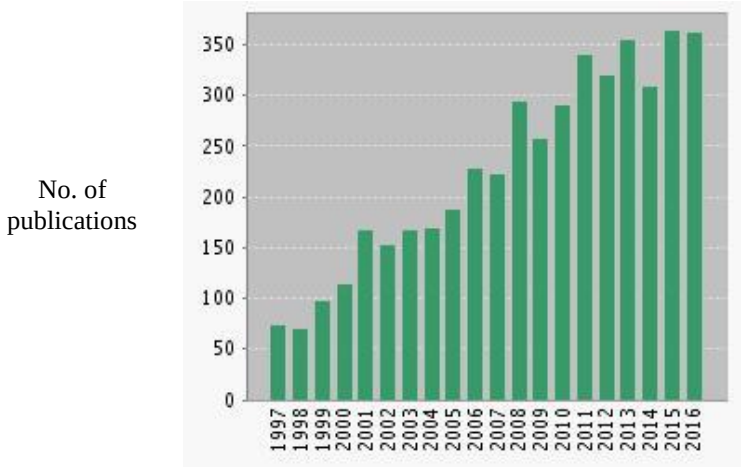

Figure 5-1. Number of publications vs year for the phrase “zeolite+membranes” in the Web of Science database.

The MFI framework is a good candidate for large-molecule gas separations, due to its 5.5 Å straight-channel pores along the b-axis. The pore size is such that MFI can differentiate between aromatic (e.g. xylene) and aliphatic (e.g. butane) isomers. As mentioned in Chapter 1, separation of *p*-xylene from its isomers is industrially very important because *p*-xylene is an essential raw material for manufacture of polyethylene terephthalate, a widely used commodity polymer.

Earlier reports of MFI membrane fabrication techniques consisted of in-situ crystallization on porous supports.[361–363] In this method, the support is immersed in a sol or gel containing the silica source, structure directing agent (SDA) and water. However, this method allowed for little control over the microstructure, thickness and sealing of defects. At dilute xylene permeation conditions (partial pressure of component ~ 0.3 kPa) and a temperature of 125ºC, *p*-xylene permeance of ~10^{-8} molm^{-2}s^{-1}Pa^{-1} and *p*-xylene/*o*-xylene separation factor (S.F.) of ~100 could be achieved.[364]

Subsequent reports improved on these results by making use of secondary growth, where a seeded support was induced to grow into a continuous film.[20,365–367] With this technique, the film thickness could be reduced and a desired orientation could be achieved. Membranes of 500 nm thickness showed a high *p*-xylene permeance (6x10^{-7} molm^{-2}s^{-1}Pa^{-1}), however, *p*-xylene/*o*-xylene S.F. of only 3.2 could be achieved, at conditions similar to those mentioned above.[24] This indicates that while there was reduction in membrane thickness, defects could not be completely eliminated. Lai et al. later reported a *p*-xylene permeance of ~10^{-7} molm^{-2}s^{-1}Pa^{-1} and a *p*-xylene/*o*-xylene S.F.

between 400-500 for a 1 µm-thick b-oriented MFI membrane.[15,20] This was achieved by modification of SDA structure (use of trimer-TPAOH instead of monomer-TPAOH), in order to obtain a mostly defect-free b-oriented MFI membrane.

Further improvements in separation performance came about as a result of modifying secondary growth conditions. Pham et al. reported the use of a tetraethyl ammonium (TEA^+) SDA-based gel growth method.[46] Use of TEA^+ prevents twinning during secondary growth and leads to perfectly b-oriented films. *p*-xylene/*o*-xylene S.F. as high as 1000 was achieved, however, *p*-xylene permeance kept decreasing from $2x10^{-7}$ $molm^{-2}s^{-1}Pa^{-1}$ to $0.5x10^{-7}$ $molm^{-2}s^{-1}Pa^{-1}$ after 400 hours. This decrease has been attributed to gradual adsorption of *o*-xylene leading to channel blocking. Later improvements by the same group led to the development of a gel-free secondary growth technique, in which the silica source for secondary growth comes from the support.[40] Using this method, 200 nm thick MFI membranes were synthesized, with a *p*-xylene permeance of $1.2x10^{-7}$ $molm^{-2}s^{-1}Pa^{-1}$ and S.F. ~ 1000. Here, the drop in permeance with time is not observed, possibly due to the short channel length.

The Tsapatsis group has reported on the reduction in membrane thickness through the use of MFI nanosheets, which are 1.5 unit cell thick sheets of MFI.[43,44] Recently, 100-200 nm thick MFI membranes were fabricated through the use of nanosheet seeds, with secondary growth done using the gel-free method.[41] Some of the results from this work, including support fabrication and n-butane/iso-butane separation, are described in this chapter.

Despite the above developments in the field of MFI membranes, there have been no examples of scale-up of MFI membranes for xylene separations at industrial scale. As mentioned in Chapter 1, one way to increase the flux of *p*-xylene, to make membrane separations industrially attractive, is to carry out permeation measurements at high pressure conditions.

5.2.1. Motivation for high temperature, high pressure xylene separations

So far, almost all reports of MFI membranes for xylene separation have used very dilute feed mixtures (*p*-xylene partial pressure ~ 500 Pa or less). Under such conditions, even with a *p*-xylene permeance ~10^{-7} mol m^{-2} s^{-1} Pa^{-1}, the effective flux of *p*-xylene will be on the order of 10^{-5} $molm^{-2}s^{-1}$, or ~$4x10^{-3}$ kg m^{-2} hr^{-1}.[41] Even if we assume an area of 350 m^2, which is the largest zeolite membrane facility in the world,[320] the maximum production that can be achieved is ~1.3 kg h^{-1}, or 12 Tons/year. The capacity of a typical plant for *p*-xylene production is on the order of 300,000 tons/year or higher,[368] so the flux of the zeolite membrane must be increased by several orders of magnitude.

One way to do this is to test with high pressure feed mixtures. By increasing *p*-xylene feed concentration by a few orders of magnitude (from 0.5 kPa to >50 kPa), the membrane can be operated at higher "stage cut", which is defined as the ratio of feed gas that permeates the membrane. At higher stage cut, flux is expected to increase proportionally. To our knowledge, only one report exists so far of high pressure xylene separation testing with MFI membranes.[24] The relevant data from this report is shown in

Table 5-1. Here, the temperature has to be raised in order to avoid saturation of MFI by *p*-xylene at high partial pressures.

Table 5-1. High temperature, high pressure xylene separation data from ref[24]. Temperature for both data points is 400ºC.

Total feed pressure (kPa)	Feed hydrocarbon partial pressure (kPa)	*p*-x feed partial pressure (kPa)	*p*-x permeance (10^{-7} mol m^{-2} s^{-1} Pa^{-1})	*p*-x/*m*-x selectivity
200	100	25	1.1	13
1800	500	125	0.275	5

Note - Feed composition: 65% *m*-xylene, 25% *p*-xylene, 5% ethylbenzene, 5% 1,3,5-trimethylbenzene, H_2 balance.

As seen in **Table 5-1**, a *p*-x permeance of >10^{-7} mol m^{-2} s^{-1} Pa^{-1} can be achieved even with *p*-xylene partial pressure 50 times higher than in the typical dilute feed conditions. This implies that a flux of about 2x10^{-3} mol m^{-2} s^{-1} is achieved, two orders of magnitude higher than the flux typically measured at dilute conditions. However, as Table 1 shows, the selectivity for *p*-xylene is low. In fact, even at dilute conditions, the highest selectivity reported in this paper is 16.

With recent improvements in zeolite membranes, including achievement of high *p*-xylene permeance and selectivity, there is a large scope to improve on the results reported in ref[24]. However, in order to successfully test at these conditions, the support should be able to withstand the high thermal and mechanical stresses. In addition, the sealing technique must ensure that there are no leaks, the likelihood of which is increased due to high temperature and pressure conditions.

Such experiments are also valuable from a fundamental transport perspective, since *p*-xylene adsorption isotherms at these temperatures do not exist in the literature. Thus, the behavior of MFI membranes at these conditions is currently hard to predict.

In this chapter, we describe the fabrication of SSF-SiC (sintered silica fiber with silicon carbide) supports, which have higher mechanical strength than previously used sintered silica fiber (SSF) supports.[41] Sealing with different types of *o*-rings is described, in order to evaluate the best sealing method. We then describe dilute Wicke-Kallenbach xylene isomer separation and high temperature, high pressure xylene separation for membranes synthesized from MFI nanosheet seeds. For the first time, we show that *p*-xylene/*o*-xylene high flux and S.F. can be achieved at 300ºC and 100 kPa full xylene feed. A high stage cut obtained implies that most of the feed gas permeates through the membrane. We further describe n-butane/iso-butane separation results, which shows much higher permeance and separation factor compared to previously reported results. Finally, the xylene permeation results for a new type of high performance membrane, made from "dC5 nanosheet" seeds, is described.

5.3. Experimental

5.3.1. Membrane fabrication

The membrane fabrication procedure was the same as that reported previously.[41] To summarize, the membrane support was made by crushing commercially obtained silica fibers (Technical Glass Products, nominal fiber length 4μm) in a stainless steel die at a load of 4 tons for 1 minute. This results in a silica fiber powder. According to the

previous method,[41] 1.7 g of powder was mixed with 10-12 drops of a 0.5 wt% PVA solution in water. This mixture was then pressed in a stainless steel die at a load of 4 tons for 1 minute. The resulting ~22 mm fiber compact was sintered at 1230ºC for 3 hours, with a heating ramp rate of 1.6ºC/min and a cooling ramp rate of 4ºC/min.

To make stronger supports that can withstand the high pressure and temperature conditions, the above procedure was slightly modified. First, 1.9 g of silica fiber powder was used per support, which gives a thicker support. Second, instead of using PVA solution, 0.5 ml of a silicon carbide precursor (StarPCS SM*P*-10, StarFire Systems) in hexane (precursor:hexane=1:4 by volume) was used. The precursor mixture was made in a glove box to prevent exposure of the silicon carbide precursor to the atmosphere. The rest of the procedure for support fabrication was the same as above, except that the compacts were sintered at 1100ºC for 4 hours (at a heating and cooling ramp rate of 4ºC/min) under a nitrogen flow of 50 sccm.

The supports were then characterized to estimate single gas permeance and mechanical strength. Single gas permeance was measured by sealing the support in a membrane cell with Viton *o*-rings and pressurizing one side of the cell with a gas (either He, N_2, CO_2 or H_2). At different gas pressures, the flow rate of permeate was measured through a bubble flow meter. Permeance was calculated as the gas flux divided by pressure difference across the membrane cell.

Strength measurements of various supports were carried out using the biaxial flexural test. In a typical ring-on-ring test, a support disk (diameter ~ 22 mm) was sandwiched between two *o*-rings (support- and loading-ring). The support-ring outer diameter (OD)

and inner diameter (ID) were 18mm and 14mm, respectively, while the loading-ring OD and ID were 10mm and 6mm, respectively. A normal force was applied on the loading-ring by a flat stainless-steel platen (MTS Bionix steel compression platen) attached to a mechanical strength-testing instrument (MTS Qtest Q10). The compression force that is required to break the support disk was measured by a load-cell, which was attached to the platen. The biaxial flexural strengths of the disks were calculated using[369]:

Biaxial flexural strength = $\frac{3P}{4\pi h^2}\left[2(1+\vartheta)\ln\left(\frac{a}{b}\right)+(1-\vartheta)\frac{(a^2-b^2)}{R^2}\right]$ ..... (1)

Where, P = load causing fracture a = radius of the support-ring b = radius of the loading-ring R = radius of the specimen h = thickness of the specimen ν = Poisson's ratio (0.17 for silica)

Following support fabrication, the supports were polished on both sides with a 600 Grit Carbimet abrasive paper (Buehler) and sonicated in DI water for 2 minutes. One side of the wet support was then smoothened by manual assembly of ~500 nm diameter Stöber silica spheres. The support was coated with the dry powder of Stöber silica and then rubbed with a gloved finger covered by Teflon tape, until the surface visually appeared smooth and uniform. The support was then sintered at 1100ºC for 3 hours with a heating ramp rate of 2ºC/min and a cooling ramp rate of 4ºC/min.

The manual assembly procedure was repeated until the silica fibers from the support were no longer visible by SEM (4-5 times). The 500 nm Stöber silica layer was then coated with 50 nm diameter Stöber silica spheres, which act as the silica source during gel-free secondary growth. A similar manual assembly process was used to coat the 50 nm silica

particles. The coated support was sintered at 400ºC for 6 hours with heating and cooling ramp rates of 1ºC/min.

The Stöber silica-coated support was coated with a seed layer of MFI nanosheets. A suspension of MFI nanosheets in octanol was prepared according to a previously described procedure.[44] The support was coated with 0.1 g of the suspension, diluted with 5 g of octanol using a vacuum-assisted coating process.[41,44] The coated support was dried at 150ºC and sintered at 400ºC for 6 hours with heating and cooling ramp rates of 1ºC/min. This coating process was repeated 3-4 times until the flow rate of octanol through the support reduced considerably (i.e. >24 h for 5 g octanol to permeate through the support).

The nanosheet-coated support was intergrown using a gel-free secondary growth process.[40,41] The support was soaked in an aqueous 0.025 M TPAOH solution for 5 minutes. The excess solution was removed by blotting on a lab-wipe. The soaked support was loaded into an autoclave with the nanosheet-coated side facing upwards. The autoclave was placed in a static oven maintained at 200ºC for 24 hours.

Following secondary growth, the support was calcined at 55º0C for 8 h with heating and cooling ramp rates of 0.5ºC/min and under air flow of 150 sccm.

For measurements on membranes made from “dC5 nanosheet” seeds, the membranes were obtained courtesy of Dr. Donghun Kim.

5.3.2. Membrane sealing

Membranes were sealed in a modified 1" VCR fitting (Swagelok Company) in which four holes were drilled, for the feed, retentate, permeate and sweep lines (see **Figure 5-2a**). Membranes were initially sealed in the cell using with Kalrez AS-568 *o*-rings (DuPont Performance Elastomers), pretreated at 250ºC for 4 hours in Helium atmosphere to prevent outgassing of carbonaceous materials during membrane testing. The cell was tightened using a torque wrench to a preset value of 60 N-m, in order to get a reproducible cell tightness every time.

G75H Perlast perfluoroelastomer (Precision Polymer Engineering Ltd.) was another type of *o*-ring that was used for sealing and is rated to 320ºC. These *o*-rings were used as obtained from the manufacturer with no pretreatment required. These *o*-rings were used in the module shown in **Figure 5-2a**.

Grafoil *o*-rings (Mercer Gasket and Shim) were also used for sealing in a modified cell designed by ExxonMobil (see **Figure 5-2b**). In this cell, the feed is split into four streams, for more uniform distribution to the membrane surface. The grafoil *o*-rings consist of flexible graphite sheets that are compacted together into an *o*-ring and are rated for high temperature >400ºC. The cell was tightened gradually turning six screws, which applied pressure on the grafoil *o*-rings and caused them to seal.

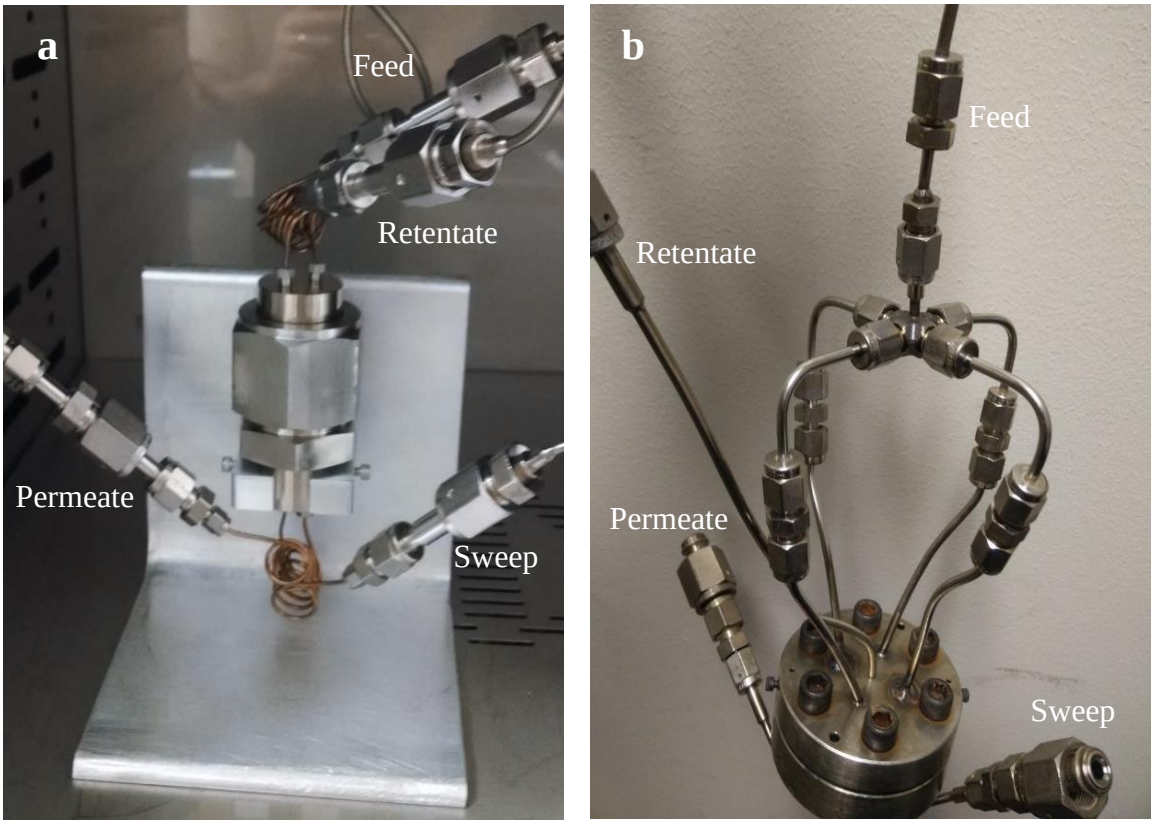

Figure 5-2. Different cell designs used for membrane sealing a. modified VCR fitting for sealing with polymer *o*-rings, b. flange-type module for sealing with grafoil *o*-rings.

5.3.3. Wicke-Kallenbach permeation measurements

The experimental setup at UMN for permeation testing consisted of sealing the membrane in a stainless-steel cell (**Figure 5-2**) and flowing the gases in Wicke-Kallenbach mode,[370] as seen in **Figure 5-3**. The total pressures of feed and permeate were maintained at atmospheric pressure. The xylene feed stream was generated by bubbling a 70 sccm flow of helium through a liquid xylene mixture in a glass bubbler which was heated using a water jacket. All lines following the bubbler were heated using

heating tapes to prevent xylene condensation. For n-butane/iso-butane permeation, equal flow rates of the gases were introduced as feed to the membrane. The membrane cell was placed in a convection oven to maintain a uniform temperature.

The feed was introduced near the surface of the membrane sealed in a membrane cell. The species that pass through the membrane were sent to a gas chromatograph with the assistance of a helium sweep stream (flow rate: 20 sccm). The composition of permeate (as well as feed) was determined using a gas chromatograph (GC, Agilent, 7890B) equipped with a flame ionization detector (FID) and a capillary column (DB-WAXetr, Chrometech). A small quantity of methane (10 sccm) was added to the permeate or feed stream sent to the GC in order to serve as an internal standard. Flow rates of all streams were measured using a bubble flow meter. The permeance is defined as the flux divided by partial pressure gradient. The separation factor is defined as the molar ratio of isomers in the permeate divided by the molar ratio of isomers in the feed.

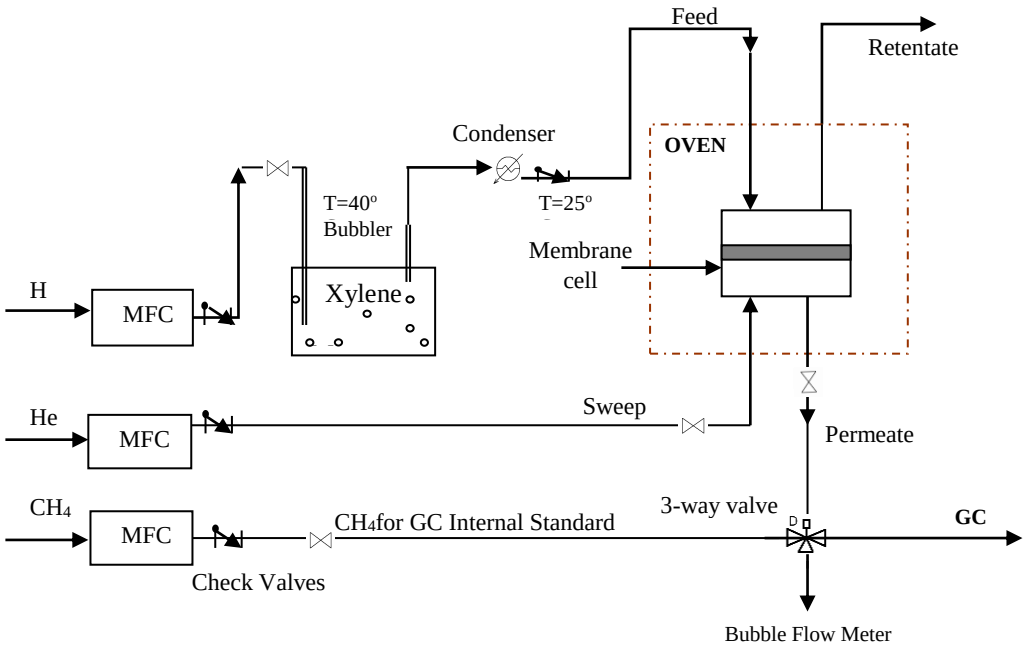

Figure 5-3. Schematic of permeation testing in Wicke-Kallenbach mode.

5.3.4. High pressure xylene permeation measurements

The experimental setup at ExxonMobil for high pressure xylene permeation measurements is shown in **Figure 5-4**. This setup can either run in Wicke-Kallenbach mode as described above or in full vapor mode. In the latter case, a syringe pump (ISCO, model number 500D) was used to send a constant flow rate (0.1 mL/min) of a liquid xylene mixture (47.5% *p*-xylene, 47.5% *o*-xylene and 5% trimethyl benzene) to the membrane cell. The feed pressure was varied through the syringe pump. The feed was passed through a preheater, which vaporized it, prior to being fed to the membrane. The permeate side was maintained under vacuum (~9-12 kPa permeate side pressure) to increase the driving force for diffusion. In addition, a helium sweep stream could also be used. The retentate and permeate compositions were determined through online GC sampling. The flux was determined by weighing the permeate, which was collected in a series of condensers, over a known period of time.

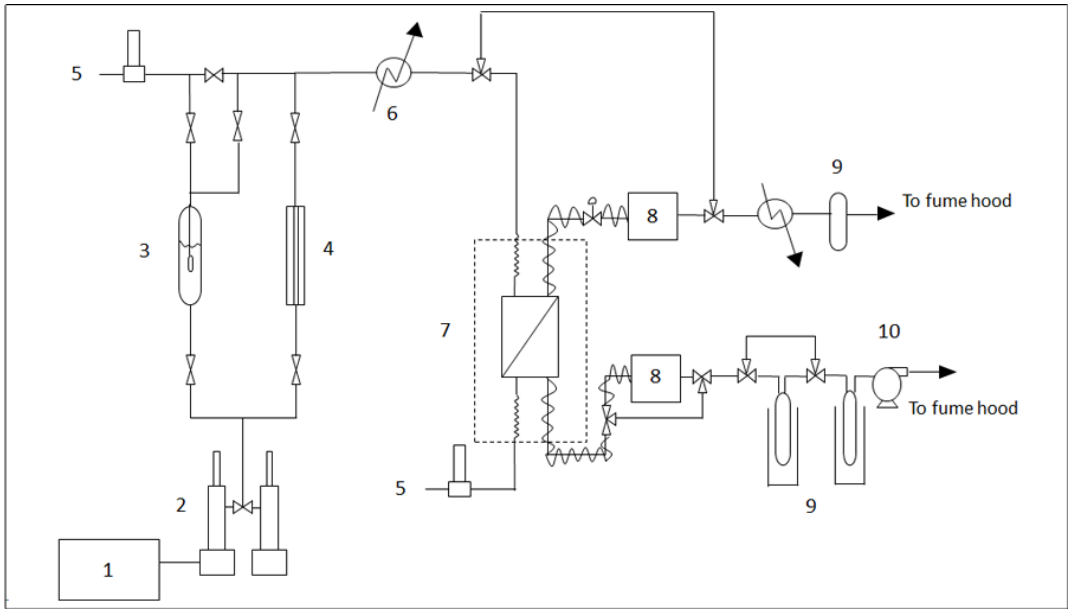

Figure 5-4. High temperature, high pressure xylene testing system at ExxonMobil. Picture of system (top) and schematic (bottom). Legend: 1 – Liquid xylene mixture, 2 – ISCO pumps for feed delivery, 3 – Sparger for dilute vapor delivery, 4 – Sight-glass, 5 – MFCs and gas handling for dilute vapor, 6 – Feed preheat for saturated/superheated vapor testing, 7 – Heated membrane oven, 8 – Automated

online GC analysis of feed, permeate and retentate, 9 – Liquid product collection (retentate and permeate), 10 – Vacuum pump

5.4. Results and Discussion

5.4.1. Support improvements

Alumina has traditionally been the support of choice for zeolite membranes.[24,361,362] Since it is a high strength ceramic support, it can withstand the high thermal and mechanical stresses, as seen in the xylene separation tests done in ref. [24]. However, the disadvantage with alumina is that when immersed in highly basic secondary growth solutions, the aluminum ions can leach out of the support.[371,372] This can cause reduction in membrane performance and decrease in support strength. Also, the gel-free secondary growth method is not possible with alumina support.[41]

As an alternative to alumina, the Yoon group showed the use of sintered Stöber silica spheres for support fabrication.[40] A mixture of 350 nm and 550 nm diameter Stöber silica spheres were mechanically pressed and sintered to form the support. Finally, it was coated with 50 nm diameter Stöber silica spheres which act as the silica source for secondary growth. Though the 200 nm-thick MFI membranes synthesized on such supports have relatively high permeance (~1.2×10^{-7} mol m^{-2} $s^{-1}$$Pa^{-1}$) and *p*-xylene/*o*-xylene S.F. > 1000, these supports have some disadvantages: 1) the use of Stöber silica spheres is very expensive for the purposes of scaling-up; 2) the mechanical strength offered by such supports is quite low and are easily broken by hand; 3) support

permeance is low and offers additional resistance to flow and 4) support quality is not easily reproducible.

We have recently shown that by using sintered silica fiber (SSF) supports, high performance MFI membranes can be made through gel-free secondary growth.[13,41] Commercially obtained silica fibers offer a low cost and high strength alternative to Stöber silica spheres. In order to smoothen the support surface, a thin layer of Stöber silica spheres can be coated either by manual assembly (rubbing) or sli*p*-casting (see **Figure 5-5**).

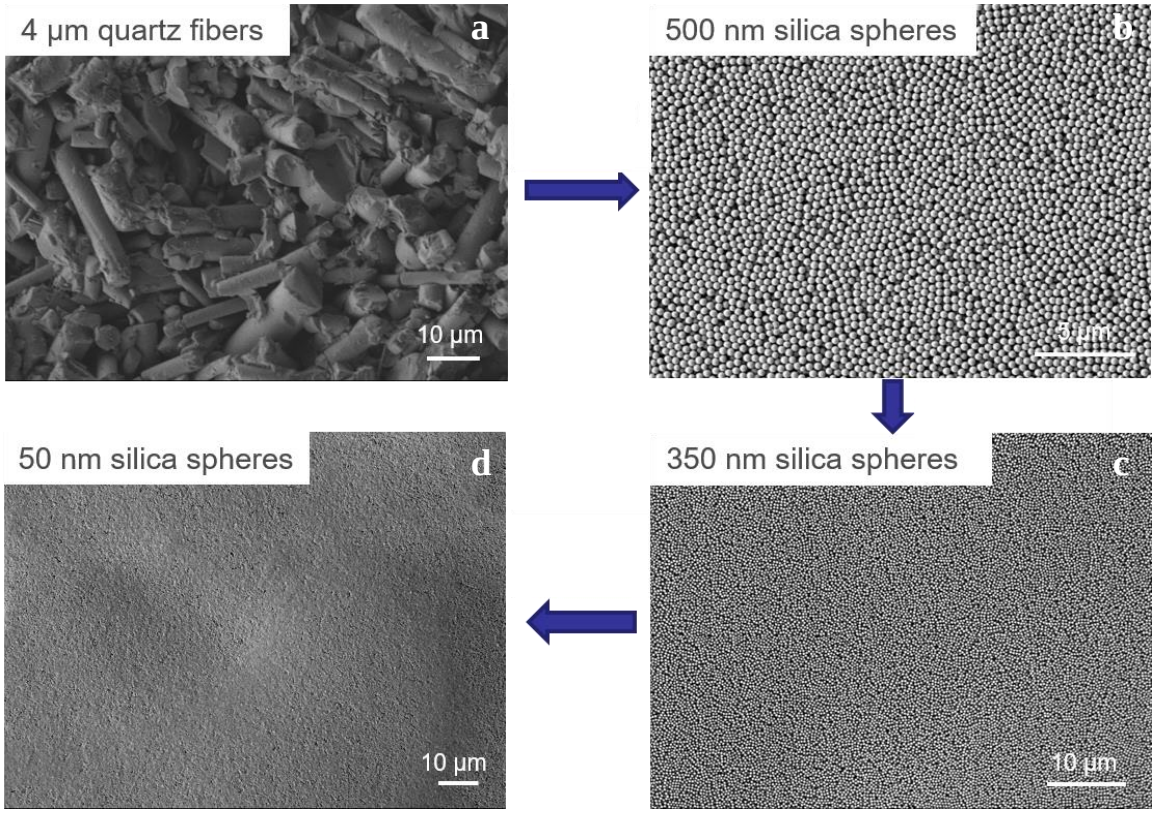

Figure 5-5. Scanning electron micrographs of SSF support fabrication process: a. Bare SSF support with quartz fibers visible, b. support surface after manual

assembly of 500 nm diameter Stober silica spheres, c. after manual assembly of 350 nm diameter Stober silica spheres, d. after manual assembly of 50 nm diameter Stober silica spheres.

As seen in **Table 5-2**, the single gas permeance of SSF supports for hydrogen, helium, nitrogen and carbon dioxide is an order of magnitude higher than that of Stöber silica supports.

Table 5-2. Single gas permeance for SSF support compared to Stöber silica support

	Single gas permeance (x 10^6 mol m^{-2} s^{-1} Pa^{-1})	
Gas	SSF support	Stöber silica support
H_2	55	5.6
He	35	3.7
N_2	21	1.7
CO_2	22	1.3

A comparison of flexural strength of these supports shows more than 3-fold improvement. SSF supports had a flexural strength of 18.2 MPa while Stöber silica supports had a flexural strength of 5.6 MPa. However, this is still far lower than the measured flexural strength of alumina supports (58 MPa). SSF supports made in this manner have been observed to usually break at high temperatures (250ºC and higher) and at pressures exceeding 2 bar.

To improve on the mechanical strength of SSF supports, we have employed two strategies. First, we have added a small amount of silicon carbide matrix precursor (StarPCS SM*P*-10, Starfire Systems) to the silica fibers prior to sintering. These SSF-SiC supports were then sintered under nitrogen flow. The second modification is that the support thickness is increased by adding a larger quantity of silica fibers per support (1.9 g compared to 1.7 g previously). The thickness of support increased from ~3.2 mm to ~3.90 mm.

These modifications led to the formation of a support that is mechanically much stronger than previous SSF supports. The breaking strength (load at which the support breaks) increased from ~430 N for SSF supports to as high as 680 N for SSF-SiC supports. Since flexural strength is breaking strength normalized by the square of the support thickness, there is a small increase (from 18.2 MPa to 20.8 MPa). However, the absolute strength of the support was high, which is indicated by the observation that the support was not broken even after applying a pressure of up to 4 bar, at a temperature of 300ºC.

SSF-SiC supports also have comparable permeance to SSF supports. The measured helium permeance is 37.6 x 10^{-6} mol m^{-2} s^{-1} Pa^{-1}, which is slightly higher than the permeance of SSF supports (see **Table 5-2**). Thus, the addition of silicon carbide matrix precursor and increase in support thickness led to greater support strength without compromising the support permeance.

For fabrication of membranes, the vacuum filtration process was used for MFI nanosheet seed deposition.[41,44] This gives good control over the thickness of the seed layer, which in turn provides control over the final membrane thickness. For a typical membrane, a

seed layer thickness of ~150-200 nm was used, which results in a final membrane thickness of 250-300 nm (see **Figure 5-6**). Thinner membranes (sub-100 nm) have also been achieved, which have higher permeance but lower separation factor.[41]

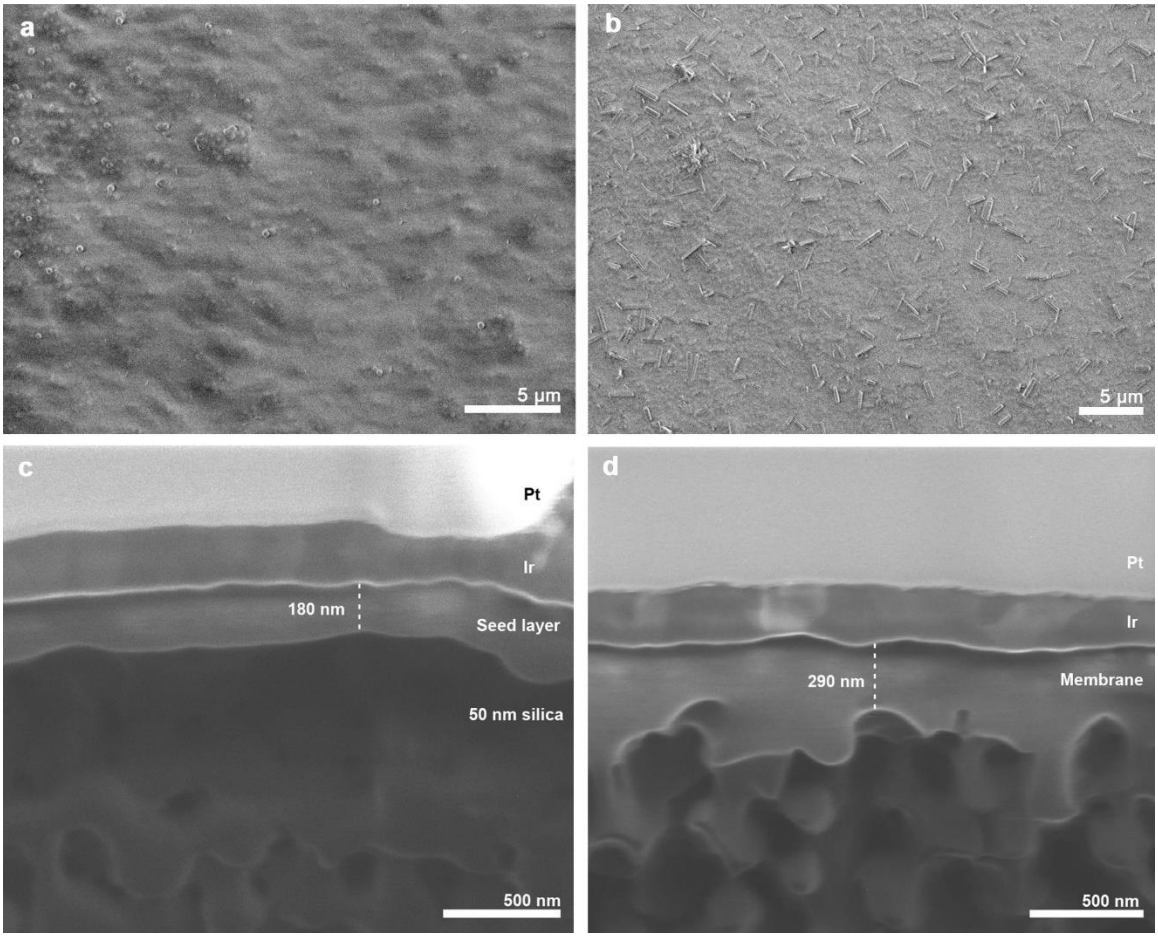

Figure 5-6. Top-view and cross-sectional SEM images of typical seed layer (a and c) and MFI membrane (b and d).

5.4.2. Membrane sealing

Kalrez *o*-rings were initially used for membrane sealing. Though these *o*-rings are rated to >300ºC, we found that during xylene permeation testing at 250ºC or higher, the

membranes were often found to be irreversibly deactivated. We assume that this was because the *o*-rings had poor chemical resistance to xylene at high temperature, leading to formation of some components that deactivated the membrane.

In order to overcome this issue, we replaced the Kalrez *o*-rings with G75H Perlast perfluoroelastomer *o*-rings. They were found to have much better thermal and chemical resistance to xylene. Irreversible membrane deactivation was not observed even at temperatures as high as 300ºC.

However, G75H Perlast *o*-rings are only rated to 320ºC. In order to extend the temperature range further, grafoil *o*-rings were utilized. These *o*-rings have been reported earlier to be successful for high temperature membrane sealing.[24] Grafoil *o*-rings consist of several graphite layers that are laminated together.[373] Hence, in order to form a good seal the membrane cell must be tightened to a great extent. However, when the cell was tightened too much, leaks were observed, possibly due to defects that develop in the flexible graphite sheets from slight differences in tightening strength at different points in the cell.

SSF membranes, which are mechanically weaker than alumina, usually broke when a high stress was applied due to tightening. SSF-SiC membranes did not break, however, a low permeance and S.F. for xylene permeation was observed (see **Table 5-3**). This could be due to small non-uniformities in cell tightening that resulted in defects. It also could be because the surface of the membranes was not smooth enough to form a good seal with grafoil.

Table 5-3. Binary *p*-xylene/*o*-xylene permeation results of membranes sealed with grafoil *o*-rings.

Membrane No.	Temperature (ºC)	*p*-x permeance (10^{-7} mol m^{-2} s^{-1} Pa^{-1})	*p*-x/*o*-x S.F.
27	150	0.46	1.3
28	150	1.5	4.3
30	180	0.91	5.9
37	150	0.23	1.3

5.4.3. Xylene permeation results

MFI membranes fabricated on SSF-SiC supports were first tested for xylene separation performance at dilute conditions. Sealing was done using G75H *o*-rings. Permeation results were obtained for two membranes in two different systems (at UMN and ExxonMobil) in order to ensure reproducibility.

As seen in **Table 5-4**, *p*-xylene permeance > 10^{-7} mol m^{-2} s^{-1} Pa^{-1} and high *p*-xylene/*o*-xylene S.F. was obtained. For membrane B14, the *o*-xylene peak area was below the detection limit in the UMN system, hence an approximate S.F. of ~1000 is reported. In the more sensitive ExxonMobil system, the peak area can be determined, resulting in an S.F. ~ 1000. For membrane B28, the *p*-xylene permeance and S.F. are slightly lower than B14 when measured in the UMN system. The permeance matches well with these values when measured in the ExxonMobil system but a higher S.F. of ~1500 is obtained. These differences could arise due to small differences in integration of the very small *o*-xylene

peak. The feed at ExxonMobil also contained a small amount (5% of hydrocarbon fraction) of trimethylbenzene (TMB), which was used to probe the presence of defects since it is too large to fit in the MFI pores. In the case of membrane B14, TMB was not detectable, while for membrane B28, a *p*-xylene/TMB S.F. >3000 was obtained, which indicates that the membrane is nearly defect-free.

From these results, it is clear that these membranes are of high quality, based on a comparison with our previous results.[41] The *p*-xylene permeance is within the range previously reported, while S.F. is much higher than the maximum S.F. of 185 obtained previously for membranes made on SSF supports.

Table 5-4. Wicke-Kallenbach permeation results for two membranes tested under dilute *p*-xylene/*o*-xylene feed (~0.5 kPa each) at 150ºC. 5% TMB is present only in the feed stream at ExxonMobil.

System	Membrane number	Permeance (10^{-7} mol m^{-2} s^{-1} Pa^{-1})			*p*-x/*o*-x S.F.	*p*-x/TMB S.F.
		p-x	*o*-x	TMB		
UMN	B14	1.12	~0.001	N/A	~1000	N/A
ExxonMobil	B14	1.51	0.0012	~0	1075	---
UMN	B28	0.97	0.0017	N/A	509	N/A
ExxonMobil	B28	1.04	0.0006	0.0003	1571	3655

Following the permeation tests under dilute conditions, high pressure xylene permeation was performed on the same membranes described above. In these experiments, the feed pressure was varied from 100 kPa full xylene vapor to 400 kPa full xylene vapor, with

temperature held constant at 300ºC. The feed composition was 47.5% *p*-xylene, 47.5% *o*-xylene and balance TMB. The results from these experiments are shown in **Figures 5-7 and 5-8**.

In **Figure 5-7**, permeance of the three feed components and *p*-xylene/*o*-xylene S.F. are plotted against feed side total pressure for membrane B14. The *p*-xylene permeance drops with increasing feed pressure while the *o*-xylene and TMB permeances remain relatively constant. This is consistent with the fact that increased feed pressure increases the *p*-xylene loading in the membrane, which reduces the *p*-xylene permeance. The *p*-xylene/*o*-xylene S.F. obtained at 100 kPa total feed pressure (47.5 kPa *p*-xylene partial pressure) is ~60. This is much higher than the previously reported *p*-xylene/*m*-xylene S.F. of 13, obtained at a *p*-xylene feed partial pressure of 25 kPa (see **Table 5-1**). Thus, at even higher loadings than previously reported, SSF-SiC supported MFI membranes have superior separation performance.

The *p*-xylene permeance under dilute conditions at 300ºC is also plotted on the same graph. The permeance under full vapor conditions at 100 kPa total feed pressure is slightly lower than the value under dilute conditions. This is primarily due to the fact that when calculating permeance at full vapor conditions, the flux is divided by a large pressure gradient compared to dilute conditions (100 kPa vs 0.5 kPa). Thus, a better measure for the actual molar flow rate of *p*-xylene through the membrane is the *p*-xylene flux itself.

In **Figure 5-8**, the *p*-xylene flux and stage cut are plotted against feed side total pressure. At 100 kPa feed side pressure, a flux approaching 10^{-3} $molm^{-2}s^{-1}$ and a stage cut of 0.72 is

obtained. This indicates ~50 times enhancement of flux over the value obtained under dilute conditions and is comparable to the values recently reported for reverse osmosis of xylene mixtures through carbon molecular sieve membranes.[374] The high stage cut implies that 72% of the feed gas permeates through the membrane. By comparison, a stage cut of <10% is typically obtained for *p*-xylene permeation under dilute conditions.

Similar results were obtained for membrane B28 at 100 kPa feed pressure and 275ºC temperature, confirming the reproducibility of these experiments. A *p*-xylene permeance of 1.1 x 10^{-8} $molm^{-2}s^{-1}Pa^{-1}$ (which implies a flux of ~4 x 10^{-4} $molm^{-2}s^{-1}$) and a *p*-xylene/*o*-xylene S.F. of 61 was obtained for membrane B28.

The results reported here indicate that ultra-thin MFI membranes fabricated by the process reported here have significant potential for industrial applications. In future, more experiments are required to explore the parameter space for optimum operating conditions, including use of lower concentration of *p*-xylene in the feed, effect of a sweep stream and effect of temperature.

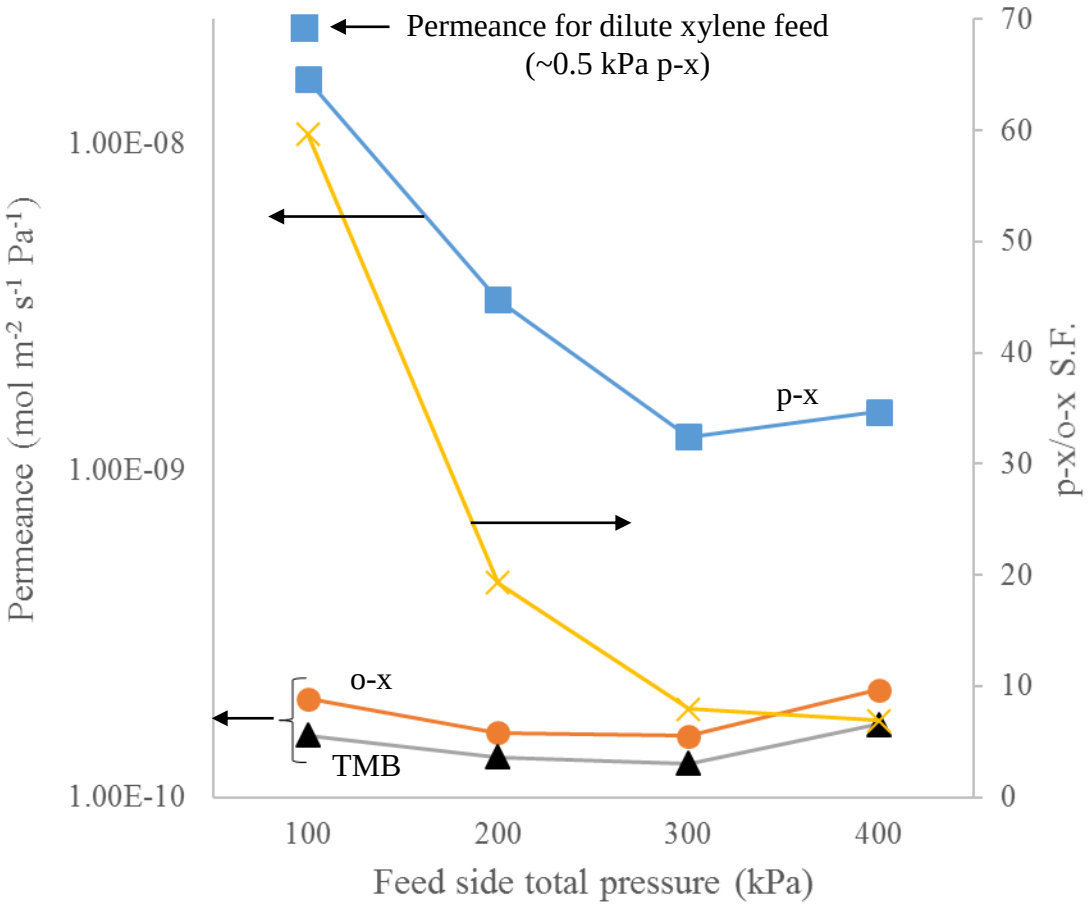

Figure 5-7. High pressure xylene permeation results for membrane B14. Permeance and S.F. plotted against feed side total pressure at 300ºC. The feed composition is 47.5% *p*-xylene, 47.5% *o*-xylene and 5% trimethylbenzene. Permeance for dilute *p*-xylene permeation at 300ºC is also shown.

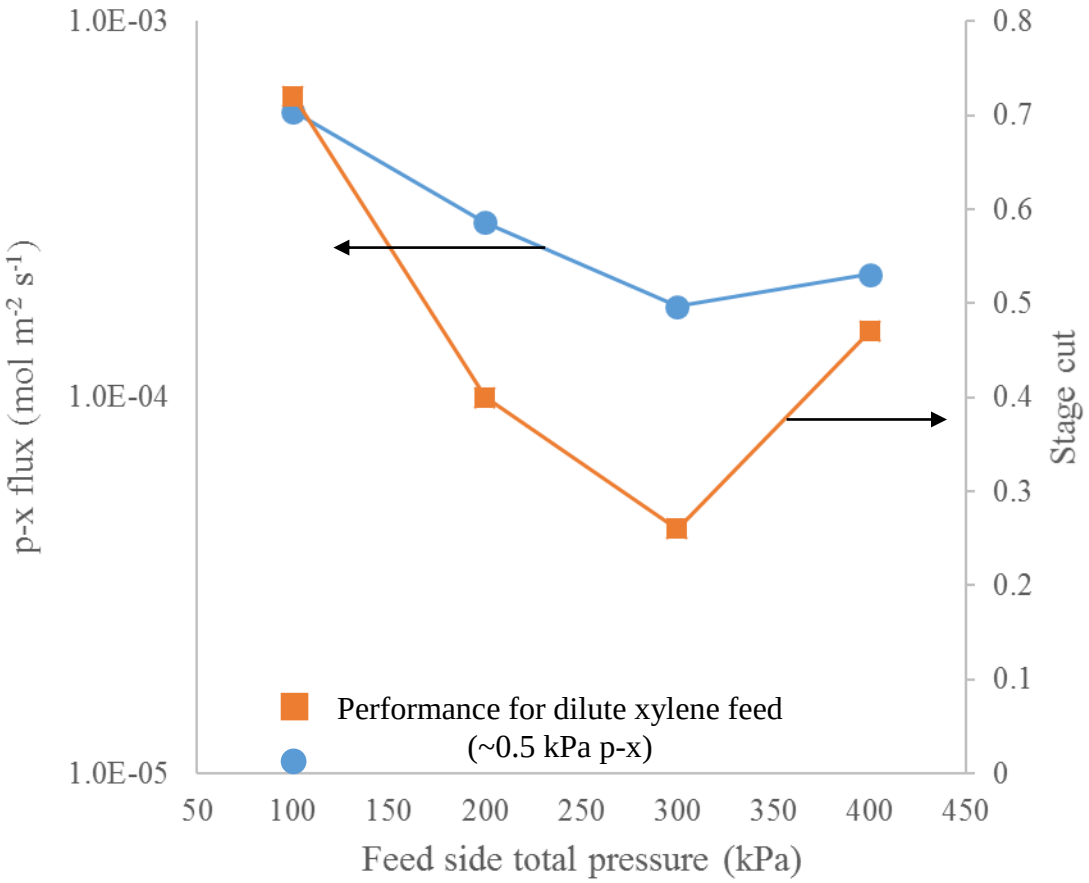

Figure 5-8. *p*-xylene flux and stage-cut vs feed side total pressure at 300°C for membrane B14. The feed composition is 47.5% *p*-xylene, 47.5% *o*-xylene and 5% trimethylbenzene. Performance for dilute xylene feed at 300°C is also shown.

5.4.4. Butane permeation

There are several reports of MFI membranes for separation of n-butane from iso-butane.[375–395] Here, we compare these results with separation performance of MFI membranes made from nanosheet seeds on SSF supports.

Table 5-5 shows binary n-butane/iso-butane permeation results for two SSF membranes (SSF-9 and SSF-10) measured at different temperatures from 25°C to 200°C. Very high n-

butane permeance and S.F. is obtained for these membranes, with permeance as high as $1.3x10^{-6}$ $molm^{-2}s^{-1}Pa^{-1}$ at 150ºC for SSF-9.

When room temperature data is compared with separation performance from refs. [375–395], we can see that S.F. is among the highest reported, while permeance is 2-3 fold higher than the best membranes previously reported. The large increase in permeance is mainly due to the decrease in membrane thickness. The selective layer of the membranes reported here is 200-300 nm in thickness while previously reported membranes from the literature exceed 1 µm in thickness of selective layer.

Table 5-5. Wicke-Kallenbach binary n-butane/iso-butane permeation results for membranes made on SSF supports. Feed consists of ~50 kPa each of n-butane and iso-butane. Reproduced from ref. [41]

Membrane No.	Temperature (ºC)	n-butane permeance (10^{-7} $molm^{-2}s^{-1}Pa^{-1}$)	S.F.
SSF - 9	25	4.3	62
	100	11.9	20
	150	12.7	15
	200	7.25	14
SSF - 10	25	2.34	47
	100	3.72	21
	150	5.14	19
	200	5.55	19

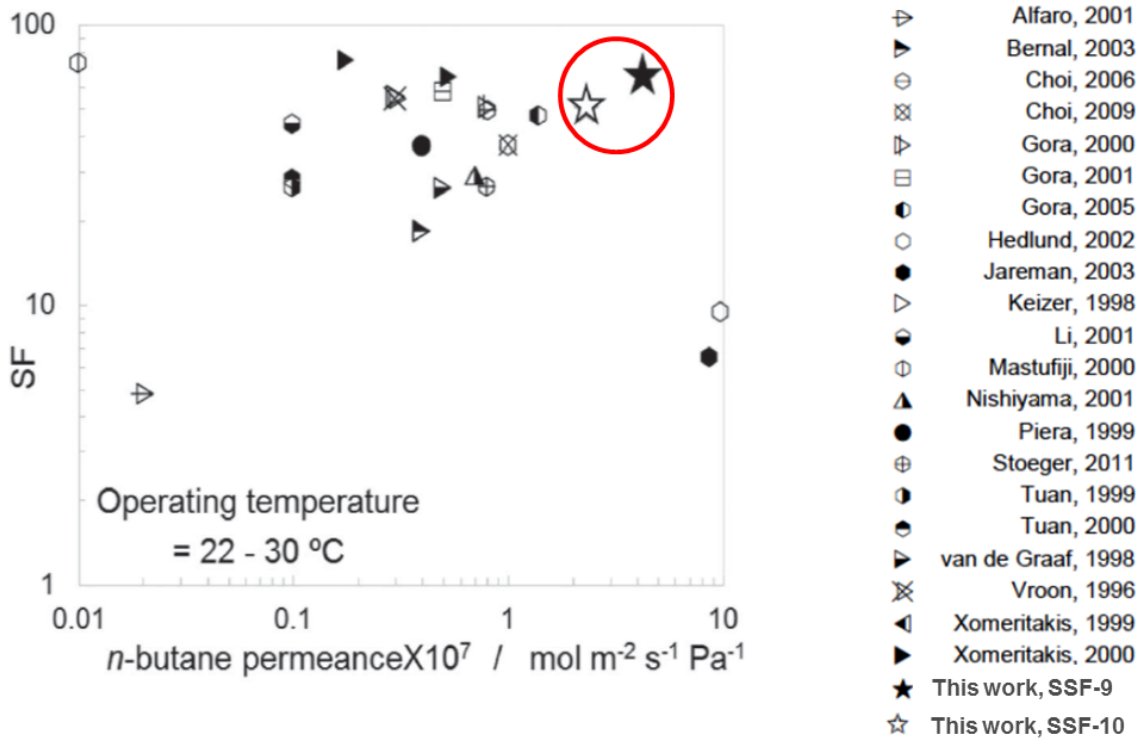

Figure 5-9. Plot of n-butane/iso-butane separation performance at room temperature for MFI nanosheet membranes and various reports of MFI membranes from the literature. Reproduced from ref. [41]

5.4.5. Membranes made using seed layers of directly synthesized nanosheets (dC5 nanosheets)

For industrial application of zeolite membranes, the cost of fabricating the membranes should be kept low. A large fraction of the cost is the ceramic support, which should eventually be replaced by a more inexpensive polymer support. Another important cost component is the seed crystals themselves. Synthesis of MFI nanosheets is time-consuming, expensive and results in a low yield. This is because they are fabricated by a

to*p*-down method, where the parent multi-lamellar MFI material is exfoliated to produce single-layer nanosheets.[43] There is a large loss of material in this process due to incomplete exfoliation. Also, large amounts of organic solvents are required to separate the single-layer nanosheets from unexfoliated particles.[44] The exfoliation process also leads to breakage of nanosheets, resulting in nanosheets with sub-micrometer lateral dimensions.

It has been previously reported that replacement of the SDA tetrapropylammonium ions (TPA^+) with a dimer or trimer of TPA^+ can modify the morphology of the MFI crystal obtained.[33,45] Specifically by using the SDA $(C_3H_7)_3N^+(CH_2)_5N^+(C_3H_7)_3$, also known as dimer-C5 (or "dC5"), MFI crystals can be obtained which are thin along the b-axis. This method, known as "bottom up" synthesis, does not involve exfoliation and can lead to high-aspect-ratio nanosheets. The cost would be lower and yield would be higher than the previous exfoliation or "top down" synthesis.

dC5 nanosheets were synthesized by hydrothermal growth of ~30 nm MFI seeds in the presence of dC5 SDA. It led to the formation of 5-nm (2.5 unit cells) thick MFI nanosheets with high-aspect-ratio. Membranes were made on SSF supports by the same method described previously for MFI nanosheet membranes. Membranes were obtained as-made from Dr. Donghun Kim. Details on synthesis and characterization can be found in ref. 55.

First, binary *p*-xylene/*o*-xylene separation performance was evaluated. As seen in **Figure 5-10**, a record high S.F. of ~2500 at and *p*-xylene permeance approaching $4x10^{-7}$ $molm^{-2}s^{-1}Pa^{-1}$ at 125ºC was achieved. This is much higher than the values reported for

membranes made from exfoliated MFI nanosheets (see **Section 5.4.3**). Equally significant is the fact that reasonably high S.F. of 30 and 300 is obtained at 50ºC and 75ºC, respectively. At 50ºC, loading of *p*-xylene in MFI approaches ~8 molecules/unit cell while at 150ºC, the loading is ~1 molecule/unit cell. This explains the ~2 orders of magnitude drop in permeance, however, it is remarkable that S.F. of even 30 can be achieved at low temperatures.

In order to evaluate the stability of membrane performance, single component *p*-xylene permeation was conducted over a period of 3 weeks (see **Figure 5-11**). The measurements were first done under decreasing membrane temperature (blue curve) and then under increasing temperature (orange curve). The two curves trace each other well, within experimental error, indicating stability of membrane performance.

Lastly, multicomponent separation performance of these membranes was evaluated. A feed vapor composition of 15.6% *p*-xylene, 18% *o*-xylene, 58.6% *m*-xylene, 7% ethylbenzene, 0.8% trimethylbenzene was used. Very high *p*-xylene permeance (approaching 8×10^{-7} $molm^{-2}s^{-1}Pa^{-1}$ at 150ºC) and separation factors were achieved. Even at a lower temperature of 75ºC, a *p*-xylene/*o*-xylene S.F. of ~300 could be obtained.

Thus, large-aspect-ratio dC5 nanosheets made from a bottom-up synthesis method, offer a viable high-yield alternative to exfoliated MFI nanosheets for fabrication of high performance membranes.

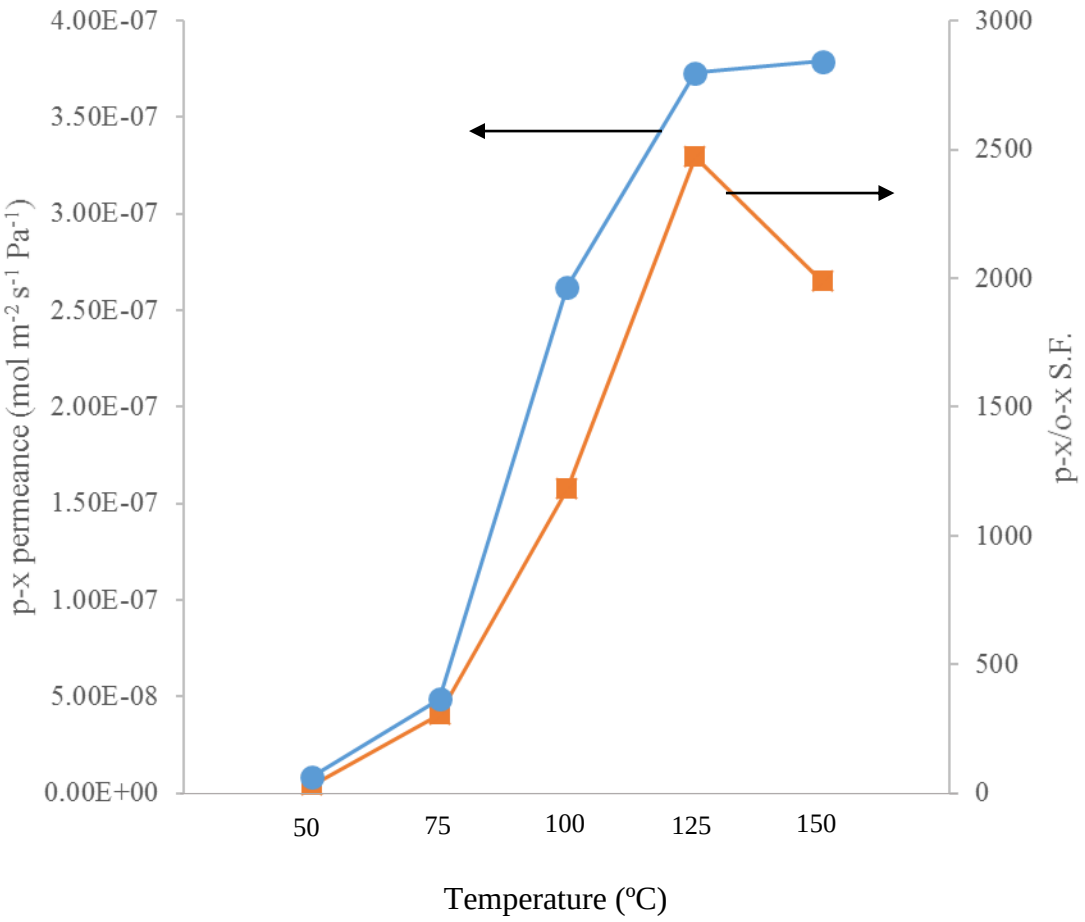

Figure 5-10. Binary *p*-xylene/*o*-xylene permeation results at different temperatures for a membrane made from dC5 nanosheet seeds. Measurements were done in Wicke-Kallenbach mode with equimolar dilute *p*-xylene/*o*-xylene feed (~0.4 kPa each) at a total feed pressure of 100 kPa.

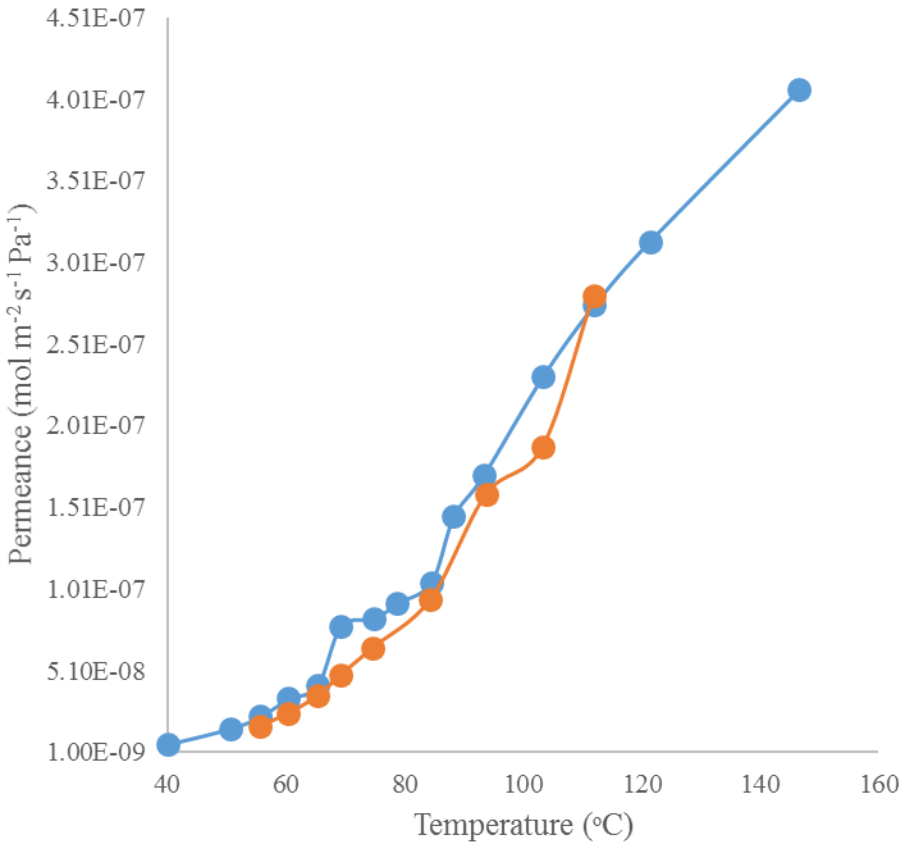

Figure 5-11. Single component *p*-x permeation results for a membrane synthesized from dC5 nanosheet seeds. Blue curve represents the behavior during decrease in permeation temperature while the red curve represents the behavior during increase in permeation temperature. The measurements were performed over a period of 3 weeks. The red curve traces the blue curve within experimental error, demonstrating the stability of membrane performance.

Table 5-6. Multi-component xylene isomer permeation results for a membrane synthesized from dC5 nanosheet seeds.

T (°C)	*p*-xylene permeance	S.F.			
	(x 10^7 mol m^{-2} s^{-1} Pa^{-1})	p-x/o-x	*p*-x/*m*-x	*p*-x/EB	*p*-x/TMB
150	7.84	1252	1719	4.0	840.4
120	1.87	2389	1379	4.6	290.6
75	0.048	290.9	155.1	3.8	7.3

5.5. Conclusions

There are currently very few examples of industrial processes that employ zeolite membranes and not a single industrial process for gas separation using a zeolite membrane. The main limitations are the low flux of traditional zeolite membranes and the lack of experimental data at industrially relevant conditions. In this chapter, the recent progress on ultra-thin, high flux MFI membranes for xylene separations has been described. Using zeolite nanosheets, the thickness of selective layer has been reduced to under 300 nm, with the possibility of reducing the thickness even further. To test at high xylene partial pressure, and consequently at high temperature, modifications were made to the support fabrication process, the sealing method and the permeation measurement system. The result of these measurements is the achievement of *p*-xylene/*o*-xylene S.F. ~ 60 and *p*-xylene flux over 20 times higher than the typical low partial pressure xylene

measurement reported in the zeolite membrane literature. A stage cut as high as 72% could be achieved, which is promising for potential industrial applications. The high separation performance of SSF membranes for butane isomers has also been demonstrated. Flux of n-butane was found to be 2-3-fold higher and S.F. among the best membranes reported previously. Finally, the xylene separation performance of membranes made from bottom-up dC5 nanosheet seeds was shown. In addition to the high p-xylene permeance, record high S.F. was obtained for binary p-xylene/o-xylene separation at 125-150ºC, while a decent S.F. could be obtained even at 50-75ºC.

The results presented here are an important step towards eventual industrial application of zeolite membranes, especially for xylene separations.

Chapter 6

Concluding Remarks

This dissertation describes the fabrication of ultra-thin zeolite films and their applications. Using nanosheets, the thickness of zeolite films has been reduced by an order of magnitude compared to typically reported zeolite films in the literature. Earlier, we have reported coatings of nanosheets on porous supports by vacuum filtration. However, the thickness could not be reduced to below 50 nm while still ensuring good surface coverage.[41] By using the Langmuir-Schaefer (LS) deposition method presented in this dissertation, monolayer transfer of nanosheets to silicon wafers with high surface coverage is now possible.[49] This has enabled the fabrication of continuous sub-12 nm thick MFI films, the thinnest ever. In future, these films should be investigated for low-dielectric constant applications. The ultra-low thickness would be favorable for incorporating them in computer chips, where the transistor size is rapidly approaching the sub-10 nm range.[17] However, the challenges that remain include scalability of the LS method, scalability of the nanosheet synthesis process (which currently has low yield of single-layer nanosheets) and application of the usually corrosive secondary growth process to temperature and chemical-sensitive computer chips.

To investigate the latter issue, thicker MFI films (~550 nm) were synthesized on silicon wafers under mild secondary growth conditions.[53] Under these conditions, we have shown that even a delicate sputtered gold coating on a silicon wafer was not etched or corroded. We also demonstrate that the traditional high temperature calcination process for zeolite activation can be successfully replaced by a near-room temperature UV-ozone treatment process. Finally, we show that MFI films synthesized by this procedure have a dielectric constant and elastic modulus close to the theoretically-predicted values for single-crystal MFI. These are promising results for eventual industrial application as low-dielectric constant materials in computer chips. Such a fabrication procedure could be applied in future for synthesis of zeolite films on various substrates, including those with limitations on temperature and chemical stability.

Finally, the recent results on zeolite membranes have been presented. High xylene isomer separation performance of zeolite membranes made from nanosheet seeds at industrially relevant conditions has been observed for the first time. At 300ºC and *p*-xylene partial pressures of 0.5 bar or higher, which is over 100 times higher than typical literature reports, the *p*-xylene flux (~7 x 10^{-4} mol/m^2/s) is 50 times higher than that obtained under low xylene feed partial pressure while maintaining a high separation factor of 60. This is a very promising result for potential industrial application of these membranes. The challenges that need to be addressed are the high cost of ceramic supports and lack of scalability of the nanosheet synthesis process. Future efforts should focus on polymer-supported zeolite membranes, especially on temperature-stable polymers like polybenzimidazole, to enable a significant reduction in cost per unit area. The second

focus should be on nanosheets synthesized in a high yield, to further enable scale-up of the membrane fabrication process. Recent results on membranes made from bottom-up dC5 nanosheet seeds are a significant step in this direction.[55]

Bibliography

[1] M. E. Davis, *Nature* **2002**, *417*, 813.

[2] C. Martínez, A. Corma, *Coord. Chem. Rev.* **2011**, *255*, 1558.

[3] International Zeolite Association **2007**, www.iza-online.org.

[4] J. Li, A. Corma, J. Yu, *Chem. Soc. Rev.* **2015**, *44*, 7112.

[5] A. Corma, V. Fornes, S. B. Pergher, T. L. M. Maesan, J. G. Buglass, *Nature* **1998**, *396*, 353.

[6] M. Choi, K. Na, J. Kim, Y. Sakamoto, O. Terasaki, R. Ryoo, *Nature* **2009**, *461*, 246.

[7] P. Bai, M. Y. Jeon, L. Ren, C. Knight, M. W. Deem, M. Tsapatsis, J. I. Siepmann, *Nat. Commun.* **2015**, *6*, No. 5912.

[8] S. Van Donk, A. H. Janssen, J. H. Bitter, K. P. de Jong, S. Van Donk, *Catal. Rev.* **2003**, *45*, 297.

[9] S. Brandenberger, O. Kröcher, A. Tissler, R. Althoff, *Catal. Rev.* **2008**, *50*, 492.

[10] S. Wang, Y. Peng, *Chem. Eng. J.* **2010**, *156*, 11.

[11] E. Erdem, N. Karapinar, R. Donat, *J. Colloid Interface Sci.* **2004**, *280*, 309.

[12] Y. Peng, H. Lu, Z. Wang, Y. Yan, *J. Mater. Chem. A* **2014**, *2*, 16093.

[13] B. Elyassi, M. Y. Jeon, K. Narasimharao, S. N. Basahel, S. Al-Thabaiti, M. Tsapatsis, *AIChE J.* **2016**, *62*, 556.

[14] D. Korelskiy, T. Leppäjärvi, H. Zhou, M. Grahn, J. Tanskanen, J. Hedlund, *J. Membr. Sci.* **2013**, *427*, 381.

[15] Z. Lai, G. Bonilla, I. Diaz, J. G. Nery, K. Sujaoti, M. a Amat, E. Kokkoli, O. Terasaki, R. W. Thompson, M. Tsapatsis, D. G. Vlachos, *Science* **2003**, *300*, 456.

[16] C. M. Lew, R. Cai, Y. Yan, *Acc. Chem. Res.* **2010**, *43*, 210.

[17] K. Maex, M. R. Baklanov, D. Shamiryan, F. Iacopi, S. H. Brongersma, Z. S. Yanovitskaya, *J. Appl. Phys.* **2016**, *93*, 8793.

[18] D. H. Olson, G. T. Kokotailo, S. L. Lawton, W. M. Meier, *J. Phys. Chem.* **1981**, *85*, 2238.

[19] T. Bein, *Chem. Mater.* **1996**, *8*, 1636.

[20] Z. Lai, M. Tsapatsis, J. P. Nicolich, *Adv. Funct. Mater.* **2004**, *14*, 716.

[21] R. P. Lively, D. S. Sholl, *Nature* **2016**, *532*, 435.

[22] C. D. Thomas, A. Cameron, R. E. Green, M. Bakkenes, L. J. Beaumont, Y. C. Collingham, B. F. N. Erasmus, M. F. de Siqueira, A. Grainger, L. Hannah, L. Hughes, B. Huntley, A. S. van Jaarsveld, G. F. Midgley, L. Miles, M. A. Ortega-Huerta, A. T. Peterson, O. L. Phillips, S. E. Williams, *Nature* **2004**, *427*, 145.

[23] C. Parmesan, G. Yohe, *Nature* **2003**, *421*, 37.

[24] J. Hedlund, J. Sterte, M. Anthonis, A. Bons, B. Carstensen, N. Corcoran, D. Cox, H. Deckman, W. De Gijnst, P. De Moor, F. Lai, J. Mchenry, W. Mortier, J. Reinoso, J. Peters, *Microporous Mesoporous Mater.* **2002**, *52*, 179.

[25] Global Paraxylene Market: Rising Use of PET Packaging in APAC to Drive Demand, observes TMR. *Transpar. Mark. Res.*

[26] D. B. Broughton, R. W. Neuzil, J. M. Pharis, C. S. Brearley, *Chem. Eng. Prog.* **1970**, *66*, 70.

[27] M. H. Paulson, Separation of Xylene Isomers by Fractional Crystallization **1956**.

[28] *World LPG Association Annual Report 2015*.

[29] S.-Y. Cho, Composition of refrigerant mixtures for low back pressure condition **2003**.

[30] K. S. Whiteley, In *Ullmann's Encyclopedia of Industrial Chemistry*; Wiley-VCH, 2012; p. 27.

[31] G. V. Research, *Butane Market Analysis By Application (LPG, Petrochemicals, Refinery) And Segment Forecasts To 2020*.

[32] N. Mittal, P. Bai, A. Kelloway, J. I. Siepmann, P. Daoutidis, M. Tsapatsis, *J. Membr. Sci.* **2016**, *520*, 434.

[33] M. A. Snyder, M. Tsapatsis, *Angew. Chem. Int. Ed. Engl.* **2007**, *46*, 7560.

[34] J. Caro, M. Noack, *Microporous Mesoporous Mater.* **2008**, *115*, 215.

[35] M. Tsapatsis, *Science* **2011**, *334*, 767.

[36] P. Peng, B. Shi, Y. Lan, *Sep. Sci. Technol.* **2011**, *46*, 234.

[37] M. Severance, B. Wang, K. Ramasubramanian, L. Zhao, W. S. W. Ho, P. K. Dutta, *Langmuir* **2014**.

[38] B. Wang, C. Sun, Y. Li, L. Zhao, W. S. W. Ho, P. K. Dutta, *Microporous Mesoporous Mater.* **2015**, *208*, 72.

[39] H. Zhang, Q. Xiao, X. Guo, N. Li, P. Kumar, N. Rangnekar, M. Y. Jeon, S. Al-thabaiti, K. Narasimharao, S. N. Basahel, B. Topuz, F. J. Onorato, C. W. Macosko, K. A. Mkhoyan, M. Tsapatsis, *Angew. Chemie Int. Ed.* **2016**, *55*, 7184.

[40] T. C. T. Pham, T. H. Nguyen, K. B. Yoon, *Angew. Chem. Int. Ed. Engl.* **2013**, *52*, 8693.

[41] K. V. Agrawal, B. Topuz, T. C. T. Pham, T. H. Nguyen, N. Sauer, N. Rangnekar, H. Zhang, K. Narasimharao, S. Basahel, L. F. Francis, C. W. Macosko, S. Al-Thabaiti, M. Tsapatsis, K. B. Yoon, *Adv. Mater.* **2015**, *27*, 3243.

[42] S. Mintova, J.-P. Gilson, V. Valtchev, *Nanoscale* **2013**, *5*, 6693.

[43] K. V. Agrawal, X. Zhang, B. Elyassi, D. D. Brewer, M. Gettel, S. Kumar, J. A. Lee, S. Maheshwari, A. Mittal, C.-Y. Sung, M. Cococcioni, L. F. Francis, A. V McCormick, K. A. Mkhoyan, M. Tsapatsis, *Science* **2011**, *334*, 72.

[44] K. V. Agrawal, B. Topuz, Z. Jiang, K. Nguenkam, B. Elyassi, M. Navarro, L. F. Francis, M. Tsapatsis, *AIChE J.* **2013**, *59*, 3458.

[45] G. Bonilla, I. Diaz, M. Tsapatsis, H. Jeong, Y. Lee, D. G. Vlachos, *Chem. Mater.* **2004**, *382*, 5697.

[46] T. C. T. Pham, H. S. Kim, K. B. Yoon, *Science* **2011**, *334*, 1533.

[47] M. Shete, M. Kumar, D. Kim, N. Rangnekar, D. Xu, B. Topuz, K. V. Agrawal, E.

Karapetrova, B. Stottrup, S. Al-Thabaiti, S. Basahel, K. Narasimharao, J. D. Rimer, M. Tsapatsis, *Angew. Chem. Int. Ed.* **2016**, *55*, 1.

[48] W. Chaikittisilp, M. E. Davis, T. Okubo, *Chem. Mater.* **2007**, *19*, 4120.

[49] N. Rangnekar, M. Shete, K. V. Agrawal, B. Topuz, P. Kumar, Q. Guo, I. Ismail, A. Alyoubi, S. Basahel, K. Narasimharao, C. W. Macosko, K. A. Mkhoyan, S. Al-Thabaiti, B. Stottrup, M. Tsapatsis, *Angew. Chemie Int. Ed.* **2015**, *54*, 6571.

[50] J. Li, X. Liu, X. Lv, B. Zhang, *Mater. Lett.* **2014**, *124*, 299.

[51] H. Kaur, S. Yadav, A. K. Srivastava, N. Singh, J. J. Schneider, *Sci. Rep.* **2016**, *6*, 1.

[52] X. Li, J. F. Gilchrist, *Langmuir* **2016**, *32*, 1220.

[53] R. Tiriolo, N. Rangnekar, H. Zhang, M. Shete, P. Bai, J. Nelson, E. Karapetrova, J. I. Siepmann, E. Lamanna, A. L. And, M. Tsapatsis, *Adv. Func. Mater.* Accepted.

[54] Z. Li, M. C. Johnson, M. Sun, E. T. Ryan, D. J. Earl, W. Maichen, J. I. Martin, S. Li, C. M. Lew, J. Wang, M. W. Deem, M. E. Davis, Y. Yan, *Angew. Chemie Int. Ed.* **2006**, *118*, 6477.

[55] M. Y. Jeon, D. Kim, P. Kumar, P. S. Lee, N. Rangnekar, P. Bai, M. Shete, B. Elyassi, H. S. Lee, K. Narasimharao, S. N. Basahel, S. Al-thabaiti, W. Xu, H. J. Cho, E. O. Fetisov, R. Thyagarajan, R. F. Dejaco, W. Fan, K. A. Mkhoyan, J. I. Siepmann, M. Tsapatsis, *Nature*, **2017**, 543, 690.

[56] R. Hoffmann, *Angew. Chem. Int. Ed. Engl.* **2013**, *52*, 93.

[57] M. Choi, K. Na, J. Kim, Y. Sakamoto, O. Terasaki, R. Ryoo, *Nature* **2009**, *461*, 246.

[58] B. Marler, H. Gies, *Eur. J. Mineral.* **2012**, *24*, 405.

[59] W. Kim, S. Nair, *Chem. Eng. Sci.* **2013**, *104*, 908.

[60] H.-K. Jeong, S. Nair, T. Vogt, L. C. Dickinson, M. Tsapatsis, *Nat. Mater.* **2003**, *2*, 53.

[61] P. Chlubná, W. J. Roth, H. F. Greer, W. Zhou, O. Shvets, A. Zukal, Č. Jiří, R. E. Morris, *Chem. Mater.* **2013**, *25*, 542.

[62] K. Möller, T. Bein, *Science* **2011**, *333*, 297.

[63] D. Xu, G. R. Swindlehurst, H. Wu, D. H. Olson, X. Zhang, M. Tsapatsis, *Adv. Funct. Mater.* **2014**, *24*, 201.

[64] H. K. Hunt, C. M. Lew, M. Sun, Y. Yan, M. E. Davis, *Microporous Mesoporous Mater.* **2010**, *128*, 12.

[65] K. B. Blodgett, *J. Am. Chem. Soc.* **1934**, *56*, 495.

[66] I. Langmuir, V. J. Schaefer, *J. Am. Chem. Soc.* **1938**, *60*, 1351.

[67] M. C. Petty, *Langmuir-Blodgett Films An Introduction*; Cambridge University Press, 1996.

[68] K. Morawetz, J. Reiche, H. Kamusewitz, H. Kosmella, R. Ries, *Colloids Surfaces A Physicochem. Eng. Asp.* **2002**, *200*, 409.

[69] L. Tosheva, V. P. Valtchev, B. Mihailova, A. M. Doyle, *J. Phys. Chem. C* **2007**,

111, 12052.

[70] Z. Wang, L. H. Wee, B. Mihailova, K. J. Edler, A. M. Doyle, *Chem. Mater.* **2007**, *19*, 5806.

[71] L. H. Wee, Z. Wang, L. Tosheva, L. Itani, V. Valtchev, A. M. Doyle, *Microporous Mesoporous Mater.* **2008**, *116*, 22.

[72] R. Makiura, S. Motoyama, Y. Umemura, H. Yamanaka, O. Sakata, H. Kitagawa, *Nat. Mater.* **2010**, *9*, 565.

[73] L. Imperiali, K. Liao, C. Clasen, J. Fransaer, C. W. Macosko, J. Vermant, *Langmuir* **2012**, *28*, 7990.

[74] A. Corma, U. Díaz, T. García, G. Sastre, A. Velty, *J. Am. Chem. Soc.* **2010**, *132*, 15011.

[75] Y. Liu, Y. Li, W. Yang, *J. Am. Chem. Soc.* **2010**, *132*, 1768.

[76] T. C. T. Pham, H. S. Kim, K. B. Yoon, *Science* **2011**, *334*, 1533.

[77] L. A. Nagahara, K. Hashimoto, A. Fujishima, D. Snowdenlfft, P. B. Price, *J. Vac. Sci. Technol. B Microelectron. Nanom. Struct.* **1994**, *12*, 1694.

[78] P. Kumar, K. V. Agrawal, K. A. Mkhoyan, M. Tsapatsis, .

[79] E. . Geus, H. Van Bekkum, *Zeolites* **1995**, *15*, 333.

[80] T. M. Davis, T. O. Drews, H. Ramanan, C. He, J. Dong, H. Schnablegger, M. a Katsoulakis, E. Kokkoli, A. V McCormick, R. L. Penn, M. Tsapatsis, *Nat. Mater.* **2006**, *5*, 400.

[81] W. Volksen, R. D. Miller, G. Dubois, *Chem. Rev.* **2010**, *110*, 56.

[82] M. R. Baklanov, K. Maex, *Philos. Trans. R. Soc. A* **2006**, *364*, 201.

[83] R. Poloni, J. Kim, *J. Mater. Chem. C* **2014**, *2*, 2298.

[84] Z. Wang, H. Wang, A. Mitra, L. Huang, Y. Yan, *Adv. Mater.* **2001**, *13*, 746.

[85] Y. Chen, G. Zhu, Y. Peng, H. Bi, J. Feng, S. Qiu, *Microporous Mesoporous Mater.* **2009**, *123*, 45.

[86] Y. Liu, C. M. Lew, M. Sun, R. Cai, J. Wang, G. Kloster, B. Boyanov, Y. Yan, *Angew. Chemie (International Ed.* **2009**, *48*, 4777.

[87] H. K. Hunt, C. M. Lew, M. Sun, Y. Yan, M. E. Davis, *Microporous Mesoporous Mater.* **2010**, *130*, 49.

[88] Z. B. Wang, A. Mitra, H. T. Wang, L. M. Huang, Y. Yan, *Adv. Mater.* **2001**, *13*, 1463.

[89] Z. J. Li, S. Li, H. M. Luo, Y. S. Yan, *Adv. Funct. Mater.* **2004**, *14*, 1019.

[90] S. Li, Z. Li, D. Medina, C. Lew, Yan, *Chem. Mater.* **2005**, *17*, 1851.

[91] Z. Li, C. M. Lew, S. Li, D. I. Medina, Y. Yan, *J. Phys. Chem. B.* **2005**, *109*, 8652.

[92] B. S. Eslava, M. R. Baklanov, A. V Neimark, F. Iacopi, C. E. A. Kirschhock, K. Maex, J. A. Martens, *Adv. Mater.* **2008**, *20*, 3110.

[93] S. Eslava, J. Urrutia, A. N. Busawon, M. R. Baklanov, F. Iacopi, S. Aldea, K. Maex, J. A. Martens, C. E. A. Kirschhock, *J. Am. Chem. Soc.* **2008**, *130*, 17528.

[94] Y. Liu, M. Sun, C. M. Lew, J. Wang, Y. Yan, *Adv. Funct. Mater.* **2008**, *18*, 1732.

[95] C. M. Lew, Y. Liu, B. Day, G. M. Kloster, H. Tiznado, M. Sun, F. Zaera, J. Wang, Y. Yan, *Langmuir* **2009**, *25*, 5039.

[96] Z. Huang, J. Zhao, *RSC Adv.* **2016**, *6*, 34825.

[97] M. Bhushan, M. B. Ketchen, *CMOS Test and Evaluation: A Physical Perspective*; Springer, 2015.

[98] A. M. Abdul-Lettif, N. N. Rammo, M. N. Makadsi, *Surf. Interface Anal.* **2001**, 117.

[99] Y. Huang, H. Qiu, F. Wang, L. Pan, Y. Tian, P. Wu, *Vacuum* **2003**, *71*, 523.

[100] M. Morgen, E. T. Ryan, J.-H. Zhao, C. Hu, T. Cho, P. S. Ho, *Annu. Rev. Mater. Sci.* **2000**, *30*, 645.

[101] K. Maex, M. R. Baklanov, D. Shamiryan, F. lacopi, S. H. Brongersma, Z. S. Yanovitskaya, *J. Appl. Phys.* **2003**, *93*, 8793.

[102] W. Volksen, K. Lionti, T. Magbitang, G. Dubois, *Scr. Mater.* **2014**, *74*, 19.

[103] J. S. Lee, J. H. Kim, Y. J. Lee, N. C. Jeong, K. B. Yoon, *Angew. Chemie Int. Ed.* **2007**, *46*, 3087.

[104] J. S. Lee, J. H. Kim, Y. J. Lee, N. C. Jeong, K. B. Yoon, *Angew. Chem. Int. Ed. Engl.* **2007**, *46*, 3087.

[105] M. Johnson, Z. Li, J. Wang, Y. Yan, *Thin Solid Films* **2007**, *515*, 3164.

[106] S. Baroni, R. Resta, *Phys. Rev. B* **1986**, *33*, 7017.

[107] M. Gajdoš, K. Hummer, G. Kresse, J. Furthmüller, F. Bechstedt, *Phys. Rev. B* **2006**, *73*, 45112.

[108] G. Kresse, *Phys. Rev. B* **1999**, *59*, 1758.

[109] J. P. Perdew, K. Burke, M. Ernzerhof, *Phys. Rev. Lett.* **1997**, *78*, 1396.

[110] V. Švorčík, O. Kvítek, O. Lyutakov, J. Siegel, Z. Kolská, *Appl. Phys. A Mater. Sci. Process.* **2011**, *102*, 747.

[111] M. Lassinantti Gualtieri, A. F. Gualtieri, J. Hedlund, *Microporous Mesoporous Mater.* **2006**, *89*, 1.

[112] H.-K. Jeong, Z. Lai, M. Tsapatsis, J. C. Hanson, *Microporous Mesoporous Mater.* **2005**, *84*, 332.

[113] A. N. Parikh, A. Navrotsky, Q. Li, C. K. Yee, M. L. Amweg, A. Corma, *Microporous Mesoporous Mater.* **2004**, *76*, 17.

[114] J. Coates, In *Encyclopedia of Analytical Chemistry*; John Wiley & Sons Ltd, 2006; pp. 1–23.

[115] H.-K. Jeong, Z. Lai, M. Tsapatsis, J. C. Hanson, *Microporous Mesoporous Mater.* **2005**, *84*, 332.

[116] C. M. Lew, Z. Li, S. Li, S.-J. Hwang, Y. Liu, D. I. Medina, M. Sun, J. Wang, M. E. Davis, Y. Yan, *Adv. Funct. Mater.* **2008**, *18*, 3454.

[117] D. Korelskiy, T. Leppäjärvi, H. Zhou, M. Grahn, J. Tanskanen, J. Hedlund, *J.*

Membr. Sci **2013**, *427*, 381.

[118] G. N. Karanikolos, J. W. Wydra, J. A. Stoeger, H. Garcia, A. Corma, M. Tsapatsis, *Chem. Mater* **2007**, *19*, 792.

[119] H. Awala, J.-P. Gilson, R. Retoux, P. Boullay, J.-M. Goupil, V. Valtchev, S. Mintova, *Nat. Mater.* **2015**, 1.

[120] W. Fan, M. a Snyder, S. Kumar, P.-S. Lee, W. C. Yoo, A. V McCormick, R. Lee Penn, A. Stein, M. Tsapatsis, *Nat. Mater.* **2008**, *7*, 984.

[121] P. Lee, X. Zhang, J. A. Stoeger, A. Malek, W. Fan, S. Kumar, W. C. Yoo, S. Al Hashimi, R. L. Penn, A. Stein, M. Tsapatsis, *J. Am. Chem. Soc.* **2011**, *133*, 493.

[122] H. Chen, J. Wydra, X. Zhang, P. S. Lee, Z. Wang, W. Fan, M. Tsapatsis, *J. Am. Chem. Soc.* **2011**, *133*, 12390.

[123] W. J. Roth, P. Nachtigall, R. E. Morris, J. Čejka, *Chem. Rev.* **2014**, *114*, 4807.

[124] U. Díaz, A. Corma, *Dalt. Trans.* **2014**, *43*, 10292.

[125] M. Tsapatsis, *AIChE J.* **2014**, *60*, 2374.

[126] K. B. Yoon, *Acc. Chem. Res.* **2007**, *40*, 29.

[127] Y. S. Chun, K. Ha, Y.-J. Lee, J. S. Lee, H. S. Kim, Y. S. Park, K. B. Yoon, *Chem. Commun. (Camb).* **2002**, *5*, 1846.

[128] A. Huang, J. Caro, *J. Mater. Chem.* **2011**, *21*, 11424.

[129] A. Huang, F. Liang, F. Steinbach, J. Caro, *J. Membr. Sci.* **2010**, *350*, 5.

[130] A. Huang, J. Caro, *Chem. Mater.* **2010**, *22*, 4353.

[131] Y. Peng, Z. Zhan, L. Shan, X. Li, Z. Wang, Y. Yan, *J. Membr. Sci.* **2013**, *444*, 60.

[132] B. Zhu, D. T. Myat, J.-W. Shin, Y.-H. Na, I.-S. Moon, G. Connor, S. Maeda, G. Morris, S. Gray, M. Duke, *J. Membr. Sci.* **2015**, *475*, 167.

[133] W. C. Yoo, J. a Stoeger, P.-S. Lee, M. Tsapatsis, A. Stein, *Angew. Chem. Int. Ed. Engl.* **2010**, *49*, 8699.

[134] E. Hu, Y. L. W. Huang, Q. Yan, D. Liu, Z. Lai, *Microporous Mesoporous Mater.* **2009**, *126*, 81.

[135] C. Wang, X. Liu, J. Li, B. Zhang, *CrystEngComm* **2013**, *15*, 6301.

[136] M. Zhou, D. Korelskiy, P. Ye, M. Grahn, J. Hedlund, *Angew. Chem. Int. Ed. Engl.* **2014**, *53*, 3492.

[137] X. Shu, X. Wang, Q. Kong, X. Gu, N. Xu, *Ind. Eng. Chem. Res.* **2012**, *51*, 12073.

[138] M. Zhou, M. Grahn, H. Zhou, A. Holmgren, J. Hedlund, *Chem. Commun.* **2014**, *50*, 14261.

[139] J. S. Lee, K. Ha, Y. J. Lee, K. B. Yoon, *Adv. Mater.* **2005**, *17*, 837.

[140] K. Ariga, Y. Yamauchi, T. Mori, J. P. Hill, *Adv. Mater.* **2013**, *25*, 6477.

[141] Z. Wang, T. Yu, P. Nian, Q. Zhang, J. Yao, S. Li, Z. Gao, X. Yue, *Langmuir* **2014**.

[142] R. Makiura, O. Konovalov, *Nature* **2013**, *3*, 1.

[143] S. Motoyama, R. Makiura, O. Sakata, H. Kitagawa, *J. Am. Chem. Soc.* **2011**, *133*, 5640.

[144] W. Wang, X. Dong, J. Nan, W. Jin, Z. Hu, Y. Chen, J. Jiang, *Chem. Commun.* **2012**, *48*, 7022.

[145] D.-J. Lee, Q. Li, H. Kim, K. Lee, *Microporous Mesoporous Mater.* **2012**, *163*, 169.

[146] B. Liu, O. Shekhah, H. K. Arslan, J. Liu, C. Woll, R. A. Fischer, *Angew. Chem. Int. Ed. Engl.* **2012**, *51*, 807.

[147] A. Bétard, H. Bux, S. Henke, D. Zacher, J. Caro, R. A. Fischer, *Microporous Mesoporous Mater.* **2012**, *150*, 76.

[148] J. Benito, M. Fenero, S. Sorribas, B. Zornoza, K. J. Msayib, N. B. McKeown, C. Téllez, J. Coronas, I. Gascón, *Colloids Surfaces A Physicochem. Eng. Asp.* **2015**, *470*, 161.

[149] X. Chen, J. Wang, D. Yin, J. Yang, J. Lu, Y. Zhang, Z. Chen, *Sep. Mater. Devices Process.* **2013**, *59*, 936.

[150] H. Li, J. Wang, J. Xu, X. Meng, B. Xu, J. Yang, S. Li, J. Lu, Y. Zhang, X. He, D. Yin, *J. Membr. Sci.* **2013**, *444*, 513.

[151] H. Li, Z. Song, X. Zhang, Y. Huang, S. Li, Y. Mao, H. J. Ploehn, Y. Bao, M. Yu, *Science* **2013**, *342*, 95.

[152] Y. Peng, Y. Li, Y. Ban, H. Jin, W. Jiao, X. Liu, W. Yang, *Science* **2014**, *346*, 1356.

[153] X. Li, Y. Peng, Z. Wang, Y. Yan, *CrystEngComm* **2011**, *13*, 3657.

[154] X. Li, Y. Yan, Z. Wang, *Ind. Eng. Chem. Res.* **2010**, *49*, 5933.

[155] Y. Liu, Y. Li, R. Cai, W. Yang, *Chem. Commun.* **2012**, *48*, 6782.

[156] A. I. Lupulescu, J. D. Rimer, *Science* **2014**.

[157] H. F. Greer, *Mater. Sci. Technol.* **2014**, *30*, 611.

[158] M. L. Gualtieri, *Microporous Mesoporous Mater.* **2009**, *117*, 508.

[159] Y. Peng, X. Lu, Z. Wang, Y. Yan, *Angew. Chemie Int. Ed.* **2015**, *54*, 1.

[160] M. E. Davis, *Chem. Mater.* **2014**, *26*, 239.

[161] K. Iyoki, K. Itabashi, T. Okubo, *Microporous Mesoporous Mater.* **2014**, *189*, 22.

[162] K. Itabashi, Y. Kamimura, K. Iyoki, A. Shimojima, T. Okubo, *J. Am. Chem. Soc.* **2012**, *134*, 11542.

[163] M. D. Oleksiak, J. D. Rimer, *Rev. Chem. Eng.* **2014**, *30*, 1.

[164] B. Xie, J. Song, L. Ren, Y. Ji, J. Li, F.-S. Xiao, *Chem. Mater.* **2008**, *20*, 4533.

[165] B. Xie, H. Zhang, C. Yang, S. Liu, L. Ren, L. Zhang, X. Meng, B. Yilmaz, U. Müller, F.-S. Xiao, *Chem. Commun.* **2011**, *47*, 3945.

[166] Y. Kamimura, S. Tanahashi, K. Itabashi, A. Sugawara, T. Wakihara, A. Shimojima, T. Okubo, *J. Phys. Chem. C* **2011**, *115*, 744.

[167] K. Honda, A. Yashiki, M. Itakura, Y. Ide, M. Sadakane, T. Sano, *Microporous Mesoporous Mater.* **2011**, *142*, 161.

[168] K. Iyoki, K. Itabashi, T. Okubo, *Chem. Asian J.* **2013**, *8*, 1419.

[169] G. Wu, W. Wu, X. Wang, W. Zan, W. Wang, C. Li, *Microporous Mesoporous Mater.* **2013**, *180*, 187.

[170] Q. Wu, X. Wang, G. Qi, Q. Guo, S. Pan, X. Meng, J. Xu, F. Deng, F. Fan, Z. Feng, C. Li, S. Maurer, U. Mu, F. Xiao, *J. Am. Chem. Soc.* **2014**, *136*, 4019.

[171] G. Majano, A. Darwiche, S. Mintova, V. Valtchev, *Ind. Eng. Chem. Res.* **2009**, *48*, 7084.

[172] H. Zhang, C. Yang, L. Zhu, X. Meng, B. Yilmaz, U. Müller, M. Feyen, F.-S. Xiao, *Microporous Mesoporous Mater.* **2012**, *155*, 1.

[173] A. Yashiki, K. Honda, A. Fujimoto, S. Shibata, Y. Ide, M. Sadakane, T. Sano, *J. Cryst. Growth* **2011**, *325*, 96.

[174] E. Ng, J. Goupil, C. Fernandez, R. Retoux, V. Valtchev, S. Mintova, *Chem. Mater.* **2012**, *24*, 4758.

[175] Z. Tang, S. J. Kim, X. Gu, J. Dong, *Microporous Mesoporous Mater.* **2009**, *118*, 224.

[176] H. Wang, Y. S. Lin, *J. Membr. Sci.* **2012**, *396*, 128.

[177] M.-H. Zhu, Z.-H. Lu, I. Kumakiri, K. Tanaka, X.-S. Chen, H. Kita, *J. Membr. Sci.* **2012**, *415–416*, 57.

[178] Y. Tang, X. Liu, S. Nai, B. Zhang, *Chem. Commun.* **2014**, *50*, 8834.

[179] E. Sjöberg, L. Sandström, O. G. W. Öhrman, J. Hedlund, *J. Membr. Sci.* **2013**, *443*, 131.

[180] H. Zhou, D. Korelskiy, E. Sjöberg, J. Hedlund, *Microporous Mesoporous Mater.* **2014**, *192*, 76.

[181] N. Peng, N. Widjojo, P. Sukitpaneenit, M. M. Teoh, G. G. Lipscomb, T. S. Chung, J. Y. Lai, *Prog. Polym. Sci.* **2012**, *37*, 1401.

[182] D. Q. Vu, W. J. Koros, S. J. Miller, *J. Membr. Sci.* **2003**, *211*, 311.

[183] R. Mahajan, W. J. Koros, *Ind. Eng. Chem. Res.* **2000**, *39*, 2692.

[184] C. M. Zimmerman, A. Singh, W. J. Koros, *J. Membr. Sci.* **1997**, *137*, 145.

[185] M. G. Süer, N. Baç, L. Yilmaz, *J. Membr. Sci.* **1994**, *91*, 77.

[186] P. Sukitpaneenit, T. S. Chung, L. Y. Jiang, *J. Membr. Sci.* **2010**, *362*, 393.

[187] T. S. Chung, L. Y. Jiang, Y. Li, S. Kulprathipanja, *Prog. Polym. Sci.* **2007**, *32*, 483.

[188] T. T. Moore, W. J. Koros, *J. Mol. Struct.* **2005**, *739*, 87.

[189] R. Patel, J. T. Park, H. P. Hong, J. H. Kim, B. R. Min, *Polym. Adv. Technol.* **2011**, *22*, 768.

[190] I. Kiesow, D. Marczewski, L. Reinhardt, M. Mu, M. Possiwan, W. A. Goedel, *J. Am. Chem. Soc.* **2013**.

[191] C. J. Duan, X. M. Jie, D. D. Liu, Y. M. Cao, Q. Yuan, *J. Membr. Sci.* **2014**, *466*, 92.

[192] T. Rodenas, I. Luz, G. Prieto, B. Seoane, H. Miro, A. Corma, F. Kapteijn, F. L. i

Xamena, J. Gascon, *Nat. Mater.* **2015**, *14*, 48.

[193] S. Sorribas, A. Kudasheva, E. Almendro, B. Zornoza, Ó. de la Iglesia, C. Téllez, J. Coronas, *Chem. Eng. Sci.* **2015**, *124*, 37.

[194] E. L. Cussler, *J. Membr. Sci.* **1990**, *52*, 275.

[195] J. Li, J. Shao, Q. Ge, G. Wang, Z. Wang, Y. Yan, *Microporous Mesoporous Mater.* **2012**, *160*, 10.

[196] Z. Zhan, J. Shao, Y. Peng, Z. Wang, Y. Yan, *J. Membr. Sci.* **2014**, *471*, 299.

[197] Y. Yushan, M. E. Davis, G. R. Gavalas, *J. Membr. Sci.* **1997**, *123*, 95.

[198] A. Navajas, R. Mallada, C. Téllez, J. Coronas, M. Menéndez, J. Santamaría, *J. Membr. Sci.* **2006**, *270*, 32.

[199] M. B. Berry, B. E. Libby, K. Rose, K. H. Haas, R. W. Thompson, *Microporous Mesoporous Mater.* **2000**, *39*, 205.

[200] G. Li, X. H. Su, R. Sen Lin, *Mater. Lett.* **2007**, *61*, 4576.

[201] M. Nomura, T. Yamaguchi, S. Nakao, *Ind. Eng. Chem. Res.* **1997**, *36*, 4217.

[202] M. Nomura, T. Yamaguchi, S. I. Nakao, *J. Membr. Sci.* **2001**, *187*, 203.

[203] A. I. Labropoulos, C. P. Athanasekou, N. K. Kakizis, A. A. Sapalidis, G. I. Pilatos, G. E. Romanos, N. K. Kanellopoulos, *Chem. Eng. J.* **2014**, *255*, 377.

[204] X. Zhu, H. Wang, Y. S. Lin, *Ind. Eng. Chem. Res.* **2010**, *49*, 10026.

[205] M. Kanezashi, Y. S. Lin, *J. Phys. Chem. C* **2009**, *113*, 3767.

[206] M. Kanezashi, J. O'Brien-Abraham, Y. S. Lin, *AIChE J.* **2008**, *54*, 1478.

[207] Z. Tang, J. Dong, T. M. Nenoff, *Langmuir* **2009**, *25*, 4848.

[208] M. Tsapatsis, G. Gavalas, *J. Membr. Sci.* **1994**, *87*, 281.

[209] W. V. Chiu, I.-S. Park, K. Shqau, J. C. White, M. C. Schillo, W. S. W. Ho, P. K. Dutta, H. Verweij, *J. Membr. Sci.* **2011**, *377*, 182.

[210] Y. Kuwahara, T. Kamegawa, K. Mori, Y. Matsumura, H. Yamashita, *Top. Catal.* **2009**, *52*, 643.

[211] Y. Kuwahara, K. Maki, Y. Matsumura, T. Kamegawa, K. Mori, H. Yamashita, *J. Phys. Chem. C* **2009**, *113*, 1552.

[212] Z. Hong, C. Zhang, X. Gu, W. Jin, N. Xu, *J. Membr. Sci.* **2011**, *366*, 427.

[213] N. Kosinov, V. G. P. Sripathi, E. J. M. Hensen, *Microporous Mesoporous Mater.* **2014**, *194*, 24.

[214] R. Krishna, L. J. P. van den Broeke, *Chem. Eng. J. Biochem. Eng. J.* **1995**, *57*, 155.

[215] R. Krishna, J. A. Wesselingh, *Chem. Eng. Sci.* **1997**, *52*, 861.

[216] F. Kapteijn, J. A. Moulijn, R. Krishna, *Chem. Eng. Sci.* **2000**, *55*, 2923.

[217] R. Krishna, R. Baur, *Sep. Purif. Technol.* **2003**, *33*, 213.

[218] R. Krishna, *J. Phys. Chem. C* **2009**, *113*, 19756.

[219] R. Krishna, *Microporous Mesoporous Mater.* **2014**, *185*, 30.

[220] A. I. Skoulidas, D. S. Sholl, *AIChE J.* **2005**, *51*, 867.
[221] T. J. H. Vlugt, R. Krishna, B. Smit, *J. Phys. Chem. B* **1999**, *103*, 1102.
[222] P. F. Lito, A. S. Santiago, S. P. Cardoso, B. R. Figueiredo, C. M. Silva, *J. Membr. Sci.* **2011**, *367*, 21.
[223] K. Y. Foo, B. H. Hameed, *Chem. Eng. J.* **2010**, *156*, 2.
[224] R. Krishna, J. M. van Baten, *Langmuir* **2010**, *26*, 10854.
[225] R. Krishna, D. Paschek, *Ind. Eng. Chem. Res.* **2000**, *39*, 2618.
[226] A. L. Myers, J. M. Prausnitz, *AIChE J.* **1965**, *11*, 121.
[227] R. Krishna, D. Paschek, *Sep. Purif. Technol.* **2000**, *21*, 111.
[228] D. P. Valenzuela, A. L. Myers, O. Talu, I. Zwiebel, *AIChE J.* **1988**, *34*, 397.
[229] L. Lu, Y. Zhu, X. Wu, S. Wang, W. Cao, X. Lu, *Sep. Sci. Technol.* **2014**, *49*, 1215.
[230] P. Bai, M. Bai, J. I. Tsapatsis, Siepmann, *Langmuir* **2012**, *28*, 15566.
[231] E. Costa, J. L. Sotelo, G. Calleja, C. Marron, *AIChE J.* **1981**, *27*, 5.
[232] E. Costa, G. Calleja, C. Marron, A. Jimenez, J. Pau, *J. Chem. Eng. Data* **1989**, *34*, 156.
[233] S. Sochard, N. Fernandes, J. Reneaume, *AIChE J.* **2010**, *56*, 3109.
[234] A. Erto, A. Lancia, D. Musmarra, *Microporous Mesoporous Mater.* **2012**, *154*, 45.
[235] M. Mofarahi, F. Gholipour, *Microporous Mesoporous Mater.* **2014**, *200*, 1.
[236] A. I. Skoulidas, D. S. Sholl, R. Krishna, *Langmuir* **2003**, *19*, 7977.
[237] R. Krishna, J. M. Van Baten, E. Garcia-Perez, S. Calero, *Ind. Eng. Chem. Res.* **2007**, *46*, 2974.
[238] R. Krishna, J. M. Van Baten, *Microporous Mesoporous Mater.* **2008**, *109*, 91.
[239] R. Krishna, J. M. Van Baten, *Chem. Phys. Lett.* **2006**, *420*, 545.
[240] C. Chmelik, L. Heinke, J. Kärger, W. Schmidt, D. B. Shah, J. M. Van Baten, R. Krishna, *Chem. Phys. Lett.* **2008**, *459*, 141.
[241] R. Krishna, J. M. van Baten, *Phys. Chem. Chem. Phys.* **2013**, *15*, 7994.
[242] D. Paschek, R. Krishna, *Langmuir* **2001**, *17*, 247.
[243] F. van Kapteijn, J. A. Moulijn, J. M. de Graaf, J. ChE, *AIChE J.* **1999**, *45*, 497.
[244] R. Krishna, J. M. van Baten, *J. Membr. Sci.* **2011**, *383*, 289.
[245] R. Krishna, J. M. Van Baten, *Chem. Eng. Sci.* **2009**, *64*, 3159.
[246] L. J. P. Van den Broeke, R. Krishna, *Chem. Eng. Sci.* **1995**, *50*, 2507.
[247] R. Krishna, *Chem. Phys. Lett.* **2000**, *326*, 477.
[248] R. Krishna, D. Paschek, *Chem. Eng. J.* **2002**, *87*, 1.
[249] D. M. Ruthven, M. Eic, E. Richard, *Zeolites* **1991**, *11*, 647.
[250] S. Brandani, M. Jama, D. Ruthven, *Microporous Mesoporous Mater.* **2000**, *35–36*, 283.
[251] D. M. Ruthven, *Adsorption* **2007**, *13*, 225.
[252] G. Xomeritakis, S. Nair, M. Tsapatsis, *Microporous Mesoporous Mater.* **2000**, *38*,

61.

[253] J. B. Lee, H. H. Funke, R. D. Noble, J. L. Falconer, *J. Membr. Sci.* **2009**, *341*, 238.

[254] R. Krishna, J. Baten, *J. Eng. Chem.* **2008**, *140*, 614.

[255] W. Zhu, P. Hrabanek, L. Gora, F. Kapteijn, J. C. Jansen, J. A. Moulijn, B. Part, *Stud. Surf. Sci. Catal.* **2004**, *154*, 1935.

[256] R. Krishna, J. M. van Baten, *Langmuir 26*, 8450.

[257] R. Krishna, J. M. van Baten, *J. Membr. Sci.* **2010**, *360*, 476.

[258] T. C. Bowen, J. C. Wyss, R. D. Noble, J. L. Falconer, *Ind. Eng. Chem. Res.* **2004**, *43*, 2598.

[259] R. Krishna, J. M. van Baten, *J. Phys. Chem. C* **2010**, *114*, 13154.

[260] K. Zhang, R. P. Lively, M. E. Dose, L. Li, W. J. Koros, D. M. Ruthven, B. A. McCool, R. R. Chance, *Microporous Mesoporous Mater.* **2013**, *170*, 259.

[261] K. Zhang, R. Zhang, C. Lively, W. Zhang, R. Koros, Chance, *J. Phys. Chem.* **2013**, *117*, 7214.

[262] K. Zhang, R. P. Lively, M. E. Dose, A. J. Brown, C. Zhang, J. Chung, S. Nair, W. J. Koros, R. R. Chance, *Chem. Commun.* **2013**, *49*, 3245.

[263] F. Kapteijn, W. J. W. Bakker, J. Van De Graaf, G. Zheng, J. Poppe, J. A. Moulijn, *Catal. Today* **1995**, *25*, 213.

[264] T. Wu, M. C. Diaz, Y. Zheng, R. Zhou, H. H. Funke, J. L. Falconer, R. D. Noble, *J. Membr. Sci.* **2015**, *473*, 201.

[265] T. Q. Gardner, J. L. Falconer, R. D. Noble, *AIChE, J* **2004**, *50*, 2816.

[266] J. Shao, Z. Zhan, J. Li, Z. Wang, K. Li, Y. Yan, *J. Membr. Sci.* **2014**, *451*, 10.

[267] H. Zhou, D. Korelskiy, T. Leppäjärvi, M. Grahn, J. Tanskanen, J. Hedlund, *J. Membr. Sci.* **2012**, *399–400*, 106.

[268] M. Grahn, J. Hedlund, *J. Membr. Sci.* **2014**, *471*, 328.

[269] S. Farooq, I. Karimi, *J. Membr. Sci.* **2001**, *186*, 109.

[270] J. G. Martinek, T. Q. Gardner, R. D. Noble, J. L. Falconer, *Ind. Eng. Chem. Res.* **2006**, *45*, 6032.

[271] L. H, S. U, J. Hoffmann, P. Niehoff, K. Haas-Santo, R. Dittmeyer, *Chem. Eng. Sci.* **2014**, *108*, 94.

[272] J. M. van de Graaf, E. van der Bijl, A. Stol, F. Kapteijn, J. A. Moulijn, *Ind. Eng. Chem. Res.* **1998**, *37*, 4071.

[273] J. M. van de Graaf, F. Kapteijn, J. A. Moulijn, *J. Membr. Sci.* **1998**, *144*, 87.

[274] T. C. Bowen, R. D. Noble, J. L. Falconer, *J. Membr. Sci.* **2004**, *245*, 1.

[275] S. Bhattacharya, S. Hwang, *J. Membr. Sci.* **1997**, *132*, 73.

[276] A. M. Avila, H. H. Funke, Y. Zhang, J. L. Falconer, R. D. Noble, *J. Membr. Sci.* **2009**, *335*, 32.

[277] G. He, Y. Mi, P. L. Yue, G. Chen, *J. Membr. Sci.* **1999**, *153*, 243.

[278] B. Raghunath, S. Hwang, J, *J. Membr. Sci.* **1992**, *65*, 147.

[279] G. Ji, G. Wang, K. Hooman, S. Bhatia, J. C. D. da Costa, *Chem. Eng. J.* **2013**, *218*, 394.

[280] G. Ji, G. Wang, K. Hooman, S. Bhatia, J. C. D. da Costa, *Chem. Eng. Sci.* **2014**, *111*, 142.

[281] E. Kim, J. Choi, M. Tsapatsis, *Microporous Mesoporous Mater.* **2013**, *170*, 1.

[282] J. Hedlund, D. Korelskiy, L. Sandström, J. Lindmark, *J. Membr. Sci.* **2009**, *345*, 276.

[283] M. Yu, R. D. Noble, J. L. Falconer, *Acc. Chem. Res.* **2011**, *44*, 1196.

[284] E. E. Mallon, M. Y. Jeon, M. Navarro, A. Bhan, M. Tsapatsis, *Langmuir 29*, 6546.

[285] M. E. Dose, K. Zhang, J. A. Thompson, J. Leisen, R. R. Chance, W. J. Koros, *Chem. Mater.* **2014**, *26*, 4368.

[286] P. H. Nelson, M. Tsapatsis, S. M. Auerbach, J, *J. Membr. Sci* **2001**, *184*, 245.

[287] J. Kangas, L. Sandström, I. Malinen, J. Hedlund, J. Tanskanen, *J. Membr. Sci.* **2013**, *435*, 186.

[288] W. Ding, H. Li, P. Pfeifer, R. Dittmeyer, *Chem. Eng. J.* **2014**, *254*, 545.

[289] Y. J. Colón, R. Q. Snurr, *Chem. Soc. Rev.* **2014**, *43*, 5735.

[290] E. Haldoupis, S. Nair, D. S. Sholl, *Phys. Chem. Chem. Phys.* **2011**, *13*, 5053.

[291] E. L. First, C. E. Gounaris, J. Wei, C. a Floudas, *Phys. Chem. Chem. Phys.* **2011**, *13*, 17339.

[292] E. L. First, C. E. Gounaris, C. A. Floudas, *Langmuir* **2013**.

[293] E. L. First, C. A. Floudas, *Microporous Mesoporous Mater.* **2013**, *165*, 32.

[294] R. L. Martin, T. F. Willems, L.-C. Lin, J. Kim, J. a Swisher, B. Smit, M. Haranczyk, *ChemPhysChem* **2012**, *13*, 3595.

[295] J. Kim, L.-C. Lin, R. L. Martin, J. A. Swisher, M. Haranczyk, B. Smit, *Langmuir* **2012**.

[296] J. Kim, M. Abouelnasr, L.-C. Lin, B. Smit, *J. Am. Chem. Soc.* **2013**.

[297] E. L. First, M. M. F. Hasan, C. A. Floudas, *AIChE J.* **2014**, *60*, 1767.

[298] J. Gascon, F. Kapteijn, B. Zornoza, V. Sebastián, C. Casado, J. Coronas, *Chem. Mater.* **2012**, *24*, 2829.

[299] H. Voss, A. Diefenbacher, G. Schuch, H. Richter, I. Voigt, M. Noack, J. Caro, *J. Membr. Sci.* **2009**, *329*, 11.

[300] S. Li, J. L. Falconer, R. D. Noble, *Adv. Mater.* **2006**, *18*, 2601.

[301] S. Li, M. A. Carreon, Y. Zhang, H. H. Funke, R. D. Noble, J. L. Falconer, *J. Membr. Sci.* **2010**, *352*, 7.

[302] J. van den Bergh, W. Zhu, J. Gascon, J. A. Moulijn, F. Kapteijn, *J. Membr. Sci.* **2008**, *316*, 35.

[303] M. Simo, In *Separation and purification technologies in biorefineries, S. Ramaswamy, H.-J. Huang, B.V. Ramarao (eds.),*; John Wiley & Sons, UK, 2013.

[304] J. S. Jeong, H. Jeon, K. M. Ko, B. Chung, G. W. Choi, *Renew. Energy* **2012**, *42*,

41.

[305] L. Y. Jiang, Y. Wang, T. S. Chung, X. Y. Qiao, J. Y. Lai, *Progr. Polym. Sci.* **2009**, *34*, 1135.

[306] N. Le, T. S. Chung, *J. Membr. Sci.* **2014**, *454*, 62.

[307] K. Vanherck, G. Koecklberghs, I. F. J. Vankelecom, *Progr. Polym. Sci.* **2013**, *38*, 874.

[308] Y. Xu, C. Chen, J. Li, *Chem. Eng. Sci.* **2007**, *62*, 2466.

[309] Y. Morigami, M. Kondo, J. Abe, H. Kita, K. Okamoto, *Sep. Purif. Technol.* **2001**, *25*, 251.

[310] K. Sato, K. Aoki, K. Sugimoto, K. Izumi, S. Inoue, J. Saito, S. Ikeda, T. Nakane, *Microporous Mesoporous Mater.* **2008**, *115*, 184.

[311] K. Sato, T. Nakane, *J. Membr. Sci.* **2007**, *301*, 151.

[312] H. Richter, I. Voigt, J.-T. Kuehnert, *Desalination* **2006**, *199*, 92.

[313] T. Gallego-Lizón, E. Edwards, G. Lobiundo, L. F. Santos, *J. Membr. Sci.* **2002**, *197*, 309.

[314] A. Urtiaga, E. D. Gorri, C. Casado, I. Ortiz, *Sep. Purif. Technol.* **2003**, *32*, 207.

[315] Y. S. Li, W. S. Yang, *Chinese J. Catal.* **2015**, *36*, 692.

[316] X. Wang, Y. Chen, C. Zhang, X. Gu, N. Xu, *J. Membr.Sci.* **2014**, *455*, 294.

[317] X. Wang, Z. Yang, C. Yu, L. Yin, C. Zhang, X. Gu, *Microporous Mesoporous Mater.* **2014**, *197*, 17.

[318] Y. Liu, Z. Yang, C. Yu, X. Gu, N. Xu, *Microporous Mesoporous Mater.* **2011**, *143*, 348.

[319] X. Gu, *Nanjing University of Technology and Jiangsu Nine Heaven High-Tech Co. Ltd., Personal Information.*

[320] Y. S. Li, W. S. Yang, *Dalian Institute of Chemical Physics, Chinese Academy of Sciences, Personal Information*.

[321] Y. S. Li, H. L. Chen, J. Liu, W. S. Yang, *J. Membr. Sci.* **2006**, *277*, 230.

[322] H. Zhou, Y. S. Li, G. Q. Zhu, J. Liu, W. S. Yang, *Sep. Purif. Technol.* **2009**, *65*, 164.

[323] Y. S. Li, J. Liu, W. S. Yang, *J. Membr. Sci.*, **2006**, *281*, 646.

[324] Y. S. Li, W. S. Yang, *J. Membr. Sci.* **2008**, *316*, 3.

[325] G. Q. Zhu, Y. S. Li, H. L. Chen, W. S. Yang, *J. Mater. Sci.* **2008**, *43*, 3279.

[326] Y. S. Li, H. L. Chen, W. S. Yang, *Chin. J. Catal.* **2006**, *27*, 544.

[327] C. Téllez, M. Menéndez, In *Membranes for Membrane Reactors: Preparation, Optimization and Selection, (eds. A. Basile and F. Gallucci)*; John Wiley & Sons, UK, 2011.

[328] M. O. Daramola, E. F. Aransiola, T. V. Ojumu, *Materials (Basel).* **2012**, *5*, 2101.

[329] *Chemical Engineering and Processing: Process Intensification, Volume 88, In Press.*; 2015.

[330] E. Drioli, E. Fontanova, In *Ullmann's Encyclopaedia of Industrial Chemistry*; Wiley-VCH, Weinheim, 2010.

[331] E. Fontanova, E. Drioli, *Chemie Ing. Tech.* **2014**, *86*, 2039.

[332] R. Dittmeyer, J. Caro, In *Handbook of Heterogeneous Catalysis, G. Ertl, H. Knözinger, F. Schüth, J. Weitkamp (eds.),*; Wiley-VCH; pp. 2198–2247.

[333] J. Caro, In *Comprehensive Membrane Science and Technology, E. Drioli, L. Giorno (eds.)*; Elsevier, 2010; pp. 1–24.

[334] S. Khajavi, S. Sartipi, J. Gascon, J. C. Jansen, F. Kapteijn, *Microporous Mesoporous Mater.* **2010**, *132*, 510.

[335] S. Khajavi, F. Kapteijn, J. C. Jansen, *J. Membr. Sci.* **2007**, *299*, 63.

[336] S.-R. Lee, Y.-H. Son, A. Julbe, J.-H. Choy, *Thin Solid Films* **2006**, *495*, 92.

[337] A. Julbe, J. Motuzas, F. Cazeville, G. Volle, C. Guizard, *Separ. Purif. Technol.* **2003**, *32*, 139.

[338] N. Wang, Y. Liu, A. Huang, J. Caro, *Microporous Mesoporous Mater.* **2015**, *207*, 33.

[339] C. Günther, H. Richter, I. Voigt, *Chem. Eng. Trans.* **2013**, *32*, 1963.

[340] S.-J. Kim, S. Yang, G. K. Reddy, P. Smirniotis, J. Dong, *Energy Fuels,* **2013**, *27*, 4471.

[341] Y. Zhang, Z. Wu, Z. Hong, X. Gu, N. Xu, *Chem. Engin. J.* **2012**, *197*, 314.

[342] S. M. Maier, A. Jentys, J. A. Lercher, *J. Phys. Chem. C,* **2011**, *115*, 8005.

[343] H. K. Beyer, *Molecular Sieves: Science and Technology, Post-Synthesis Modification I*; Springer Berlin Heidelberg, 2002.

[344] G. Kennedy, S. Lawton, A. Fung, M. Rubin, S. Steuernagel, *Catal. Today* **1999**, *49*, 385.

[345] G. Kennedy, S. Lawton, M. Rubin, *J. Am. Chem. Soc.,* **1994**, *116*, 11000.

[346] D. Ma, F. Deng, R. Fu, X. Dan, X. Bao, *J. Phys. Chem. B,* **2001**, *105*, 1770.

[347] R. Kreiter, M. Rietkerk, H. Castricum, H. van Veen, J. ten Elshof, J. Vente, *J. SolGel. Sci. Technol.* **2011**, *57*, 245.

[348] B. Elyassi, X. Zhang, M. Tsapatsis, *Microporous Mesoporous Mater.* **2014**, *193*, 134.

[349] K. Sato, K. Sugimoto, Y. Sekine, M. Takada, M. Matsukata, T. Nakane, *Microporous Mesoporous Mater.* **2007**, *101*, 312.

[350] K.-I.Sawamura, T. Shirai, M. Takada, Y. Sekine, E. Kikuchi, M. Matsukata, *Catal. Today* **2008**, *132*, 182.

[351] S. A. S. Rezai, J. Lindmark, C. Andersson, F. Jareman, K. Moller, J. Hedlund, *Microporous Mesoporous Mater.* **2008**, *108*, 136.

[352] T. Masuda, N. Fukumoto, M. Kitamura, *Microporous Mesoporous Mater.* **2001**, *48*, 239.

[353] S. J. Kim, Z. Xu, G. K. Reddy, P. Smirniotis, J. H. Dong, *Ind. Eng. Chem. Res.*

2012, *51*, 1364.

[354] M. P. Bernal, E. Piera, J. Coronas, M. Menéndez, J. Santamaría, *Catal. Today* **2000**, *56*, 221.

[355] H. Wang, Y. S. Lin, *AIChE J.* **2012**, *58*, 153.

[356] J. Canivet, A. Fateeva, Y. Guo, B. Coasne, D. Farusseng, *Chem. Soc. Rev.* **2014**, *43*, 5594.

[357] N. C. Burtch, H. Jasuja, K. S. Walton, *Chem. Rev.* **2014**, *114*, 10575.

[358] J. J. Low, A. I. Benin, P. Jakubczak, J. F. Abrahamian, S. A. Faheem, R. R. Willis, *J. Am. Chem. Soc.* **2009**, *131*, 15834.

[359] A. Huang, W. Dou, J. Caro, *J. Am. Chem. Soc.* **2010**, *132*, 15562.

[360] A. Huang, Y. Chen, Q. Liu, N. Wang, J. Jiang, J. Caro, *J. Membr. Sci.* **2014**, *454*, 126.

[361] Y. Yan, M. E. Davis, G. R. Gavalas, *Ind. Eng. Chem. Res.* **1995**, *34*, 1652.

[362] Y. Yan, M. Tsapatsis, G. R. Gavalas, M. E. Davis, *J. Chem. Soc., Chem. Commun.* **1995**, 227.

[363] R. Lai, G. R. Gavalas, *Ind. Eng. Chem. Res.* **1998**, *37*, 4275.

[364] K. Keizer, A. J. Burggraaf, Z. A. E. P. Vroon, H. Verweij, *J. Membr. Sci.* **1998**, *147*, 159.

[365] Z. Lai, M. Tsapatsis, *Ind. Eng. Chem. Res.* **2004**, *43*, 3000.

[366] G. Xomeritakis, Z. Lai, M. Tsapatsis, *Ind. Eng. Chem. Res.* **2001**, *40*, 544.

[367] G. Xomeritakis, M. Tsapatsis, *Chem. Mater.* **1999**, *11*, 875.

[368] A. M. Niziolek, O. Onel, C. A. Floudas, *AIChE J.* **2016**, *62*, 1531.

[369] J. Kim, G. Zi, C. Yi, *Mag. Concr. Res.* **2012**, *64*, 1057.

[370] J. Choi, S. Ghosh, L. King, M. Tsapatsis, *Adsorption* **2006**, *12*, 339.

[371] N. Nishiyama, K. Ueyama, M. Matsukata, *Microporous Mesoporous Mater.* **1996**, *7*, 299.

[372] E. R. Geus, M. J. Den Exter, H. Van Bekkum, *J. Chem. Soc. Faraday Trans.* **1992**, *88*, 3101.

[373] J. H. Shane, R. J. Russell, R. A. Bochman, US Patent 3,404,061 Flexible Graphite Material of Expanded Particles Compressed Together **1968**.

[374] D.-Y. Koh, B. A. McCool, H. W. Deckman, R. P. Lively, *Science* **2016**, *353*, 804.

[375] V. A. Tuan, J. L. Falconer, R. D. Noble, *Ind. Eng. Chem. Res.* **1999**, *38*, 3635.

[376] G. Xomeritakis, S. Nair, M. Tsapatsis, *Microporous Mesoporous Mater.* **2000**, *38*, 61.

[377] G. Xomeritakis, A. Gouzinis, S. Nair, T. Okubo, M. Y. He, R. M. Overney, M. Tsapatsis, *Chem. Eng. Sci.* **1999**, *54*, 3521.

[378] Z. A. E. P. Vroon, K. Keizer, M. J. Gilde, H. Verweij, A. J. Burggraaf, *J. Membr. Sci.* **1996**, *113*, 293.

[379] J. Piera, E. Bernai, M. P. Salomon, M. A. Coronas, J. Menendez, M. Santamaria,

Stud. Surf. Sci. Catal. **1999**, *125*, 189.

[380] V. A. Tuan, J. L. Falconer, R. D. Noble, *Microporous Mesoporous Mater.* **2000**, *41*, 269.

[381] J. A. Stoeger, J. Choi, M. Tsapatsis, *Energy Environ. Sci.* **2011**, *4*, 3479.

[382] N. Nishiyama, L. Gora, V. Teplyakov, F. Kapteijn, J. A. Moulijn, *Sep. Purif. Technol.* **2001**, *22–23*, 295.

[383] T. Matsufuji, N. Nishiyama, *J. Membr. Sci.* **2000**, *178*, 25.

[384] Y. Li, X. Zhang, J. Wang, *Sep. Purif. Technol.* **2001**, *25*, 459.

[385] K. Keizer, A. J. Burggraaf, Z. A. E. P. Vroon, H. Verweij, *J. Membr. Sci.* **1998**, *147*, 159.

[386] F. Jareman, J. Hedlund, J. Sterte, *Sep. Purif. Technol.* **2003**, *32*, 159.

[387] J. Hedlund, J. Sterte, M. Anthonis, A. J. Bons, B. Carstensen, N. Corcoran, D. Cox, H. Deckman, W. De Gijnst, P. P. de Moor, F. Lai, J. McHenry, W. Mortier, J. Reinoso, *Microporous Mesoporous Mater.* **2002**, *52*, 179.

[388] S. Alfaro, M. Arruebo, *Microporous Mesoporous Mater.* **2001**, *50*, 195.

[389] M. P. Bernal, J. Coronas, M. Menéndez, J. Santamarı, *Microporous Mesoporous Mater.* **2003**, *60*, 99.

[390] J. Choi, S. Ghosh, L. King, M. Tsapatsis, *Adsorption* **2006**, *12*, 339.

[391] J. Choi, H.-K. Jeong, M. A. Snyder, J. A. Stoeger, R. I. Masel, M. Tsapatsis, *Science* **2009**, *325*, 590.

[392] L. Gora, J. Jansen, T. Maschmeyer, *Chemistry (Easton).* **2000**, *6*, 2537.

[393] L. Gora, N. Nishiyama, J. C. Jansen, F. Kapteijn, V. Teplyakov, *Sep. Purif. Technol.* **2001**, *22–23*, 223.

[394] J. M. Van De Graaf, E. Van Der Bijl, A. Stol, F. Kapteijn, J. A. Moulijn, *Ind. Eng. Chem. Res.* **1998**, *37*, 4071.

[395] L. Gora, J. C. Jansen, *J. Catal.* **2005**, *230*, 269.